UNIVERSITY OF SÃO PAULO

SÃO CARLOS SCHOOL OF ENGINEERING

NAIARA ARANTES LIMA

# Synthesis and characterization of Cu, Ni and Zn tungstates for mulfunctional applications: catalysis, photocatalysis and pigment

# Síntese e caracterização de tungstatos de Cu, Ni e Zn para aplicações mulfuncionais: catálise, fotocatálise e pigmento

São Carlos

2021

NAIARA ARANTES LIMA

# Synthesis and characterization of Cu, Ni and Zn tungstates for mulfunctional applications: catalysis, photocatalysis and pigment

# Síntese e caracterização de tungstatos de Cu, Ni e Zn para aplicações mulfuncionais: catálise, fotocatálise e pigmento

**Revised Version**

Thesis presented to the Graduate Program in Materials Science and Engineering at University of São Paulo to obtain the degree of Doctor of Science.

Concentration area: Development, Characterization and Application of Materials

Supervisor: Dra. Maria Inês Basso Bernardi

São Carlos

2021

AUTHORIZE THE REPRODUCTION OF TOTAL OR PARTIAL COPIES OF THIS THESIS, BY CONVENTIONAL OR ELECTRONIC MEDIA FOR STUDY OR RESEARCH PURPOSE, SINCE IT IS REFERENCED.

AUTORIZO A REPRODUÇÃO TOTAL OU PARCIAL DESTE TRABALHO, POR QUALQUER MEIO CONVENCIONAL OU ELETRÔNICO, PARA FINS DE ESTUDO E PESQUISA, DESDE QUE CITADA A FONTE.

Ficha catalográfica elaborada pela Biblioteca Prof. Dr. Sérgio Rodrigues Fontes da EESC/USP com os dados inseridos pelo(a) autor(a).

Arantes Lima, Naiara
As Synthesis and characterization of Cu, Ni and Zn tungstates for mulfunctional applications: catalysis, photocatalysis and pigment / Naiara Arantes Lima; orientadora Maria Inês Basso Bernardi. São Carlos, 2020.

Tese (Doutorado) - Programa de Pós-Graduação em Ciência e Engenharia de Materiais e Área de Concentração em Desenvolvimento, Caracterização e Aplicação de Materiais -- Escola de Engenharia de São Carlos da Universidade de São Paulo, 2020.

1. tungstates. 2. catalysis. 3. photocatalysis. 4. pigments. 5. mulfunctional applications. I. Título.

Eduardo Graziosi Silva - CRB - 8/8907

# FOLHA DE JULGAMENTO

Candidata: Licenciada **NAIARA ARANTES LIMA.**

Título da tese: " Síntese e caracterização de tungstatosde Cu, Ni e Zn para aplicações multifuncionais: catálise, fotocatálise e pigmento".

Data da defesa: 18/02/2021.

**Comissão Julgadora** **Resultado**

Dra. **Maria Ines Basso Bernardi** APROVADA
**(Orientadora)**
(Instituto de Física de São Carlos/IFSC-USP)

Prof. Associado **Rafael Salomão** APROVADA
(Escola de Engenharia de São Carlos/EESC-USP)

Dra. **Elaine Cristina Paris** APROVADA
(Empresa Brasileira de Pesquisa Agropecuária/EMBRAPA)

Prof. Dr. **Alexandre Mesquita** APROVADA
(Universidade Estadual Paulista "Júlio de Mesquita Filho"/UNESP-Rio Claro)

Dr. **Gelson Tiago dos Santos Tavares da Silva** APROVADA
(Empresa Brasileira de Pesquisa Agropecuária /EMBRAPA)

Coordenador do Programa de Pós-Graduação em Engenharia de Materiais:
Prof. Associado **Marcelo Falcão de Oliveira**

Presidente da Comissão de Pós-Graduação:
Prof. Titular **Murilo Araujo Romero**

I dedicate this thesis to my parents Patrícia and Claudio, and to my grandparents Glória and João (in memorian).

**ACKNOWLEDGMENTS**

First of all, I wish to thank the University of São Paulo and the post graduation program (PGrCEM) for the financing and infrastructure,

I thank the Institute of Physics for the infrastructure provided,

The Biophysics Laboratory (IFSC/USP) for the space provided and for the equipment and materials made available,

my advisor, Dr. Maria Inês Basso Bernardi, for her teachings and friendship throughout the development of my doctoral research.

I would also like to thank

Prof. Dr. Luis Fernando da Silva (UFSCar) and Prof. Dr. Renato Vitalino Gonçalves (IFSC/USP) for the teachings on photocatalysis,

Prof. Dra. Elaine Cristina Paris (Embrapa) for the teachings and for providing laboratories and equipment for the photocatalytic studies,

Prof. Dr. Alexandre Mesquita (UNESP/ Rio Claro) for the X-ray absorption measurements, scientific discussions and help throughout this dissertation,

Prof. Dr. Maximo Siu Li (IFSC/USP) for the help with photoluminescence measurements,

Prof. Dr. Humberto Vieira Fajardo (UFOP) for the catalysis measurements and discussion of the results,

This study was financed in part by the Coordenação de Aperfeiçoamento Pessoal de Nível Superior -Brasil (CAPES) - Finance Code 159866/2018-9

CEPID 2013 / 07296-2 and 2018 / 07517-2 São Paulo Research Foundation (FAPESP);

This study was financed in part by the FAPESP - 2013/07909-4;

This study was financed in part by the Conselho Nacional de Desenvolvimento Científico e Tecnológico (CNPq) - Finance Code 405033/2018-4 and 300954/2018-2;

Finally, I thank the countless friends who were essential and brought me a lot of happiness during these 4 years.

*“Há duas formas para viver sua vida.Uma é acreditar que não existe milagre. A outra é acreditar que todas as coisas são um milagre.”*

(Albert Einstein)

## ABSTRACT

LIMA, Naiara Arantes. **Synthesis and characterization of Cu, Ni and Zn tungstates for mulfunctional applications: catalysis, photocatalysis and pigment**. Thesis (Doctor in Science) - Escola de Engenharia de São Carlos, Universidade de São Paulo, São Carlos, 2020.

In this research, copper ($CuWO_4$), nickel ($NiWO_4$) and zinc ($ZnWO_4$) tugstates were applied in three different themes: catalysis, photocatalysis and pigments. In the catalysis application, Cu, Ni and Zn tungstates were synthesized by the polymeric precursor method (PPM, and their catalytic activity was evaluated as a function of the conversion of thioanisole to methyl phenyl sulfoxide and methyl phenyl sulfone, according to the catalyst nature, reaction time, temperature and $H_2O_2$ concentration. $CuWO_4$ was the most effective catalyst mainly due to the greater number of vacancies / oxygen mobility proportional to the increased catalytic activity. In the photocatalysis application, copper tunsgtate was synthesized by the coprecipitation (CM), microwave-assisted hydrothermal (HM) and polymeric precursor (PPM) methods, and its photocatalytic activity was evaluated for the degradation of the Rhodamine B dye. The study was carried out in order to understand the influence of the synthesis method on the material properties, and consequently on the photocatalytic response. The influence of the oxidizing agent $H_2O_2$ and the sodium oxalate and silver nitrate scavengers were evaluated in the reaction. With the addition of $Ag^+$ ions, the recombination rate was minimized and the reaction occurred more efficiently for $CuWO_4$ (PPM) (20 min = 100% of degradation). The most relevant properties that may have influenced catalytic efficiency were surface charge (-38.5 for PPM < -29.7 for CM < -16.2 for HM) and the number of oxygen vacancies (PPM > HM > CM). In the pigment application, $NiWO_4$ was synthesized by the polymeric precursor method for the manufacture of a yellow pigment. The material was evaluated for its stability, color pattern, luminescence and reproducibility. The results showed that $NiWO_4$, whose yellow color was due to the electronic transitions of $Ni^{2+}$, proved to be stable for calcination temperatures above 700 °C. Additionally, when illuminated this material presented light emission in the blue-green region, indicating luminescent properties.



Keywords: Tungstates. Catalysis. Photocatalysis. Pigments. Mulfunctional applications.

# RESUMO

LIMA, Naiara Arantes. **Síntese e caracterização de tungstatos de Cu, Ni e Zn para aplicações mulfuncionais: catálise, fotocatálise e pigmento**. Tese (Doutorado em Ciências) - Escola de Engenharia de São Carlos, Universidade de São Paulo, São Carlos, 2020.

Nesta tese os tugstatos de cobre ($CuWO_4$), níquel ($NiWO_4$) e zinco ($ZnWO_4$) foram aplicados em três temas distintos: catálise, fotocatálise e pigmentos. Na aplicação em Catálise, os tungstatos de Cu, Ni e Zn foram sintetizados pelo método dos precursores poliméricos (PPM) e sua atividade catalítica foi avaliada em função da conversão de tioanisol em metil fenil sulfóxiodo e metil fenil sulfona. A atividade catalítica foi avaliada em função da natureza do catalisador, tempo de reação, temperatura e concentração de $H_2O_2$. O $CuWO_4$ foi o catalisador mais eficaz devido principalmente ao maior número de vacâncias/mobilidade de oxigênio que são proporcionais à maior atividade catalítica. Na aplicação em Fotocatálise, o tunsgtato de cobre foi sintetizado pelos métodos de Coprecipitação (CM), Hidrotermal assistido por micro-ondas (HM) e Precursores poliméricos PPM e sua atividade fotocatalítica foi avaliada para a degradação do corante rodamina B. O estudo foi feito em busca de compreender a influência do método de síntese nas propriedades do material e consequentemente na resposta fotocatalítica. A influência do agente oxidante $H_2O_2$ e os sequestradores oxalato de sódio e nitrato de prata foram avaliados na reação. Com a adição de íons $Ag^+$ a taxa de recombinação foi minimizada e a reação ocorreu mais eficientemente para $CuWO_4$ (PPM) (20 min = 100% degradação). As propriedades mais relevantes e que podem ter influenciado na eficiência catalítica foi a carga superficial (-38.5 for PPM < -29.7 for CM < -16.2 for HM) e a quantidade de vacâncias de oxigênio (PPM > HM > CM). Na aplicação em Pigmento, o $NiWO_4$ foi sintetizado pelo método dos precursores poliméricos para a fabricação de um pigmento de coloração amarela. O material foi avaliado quanto a sua estabilidade, padrão de cor e

luminescência e reprodutibilidade. O $NiWO_4$ apresentou-se estável para temperaturas de calcinação acima de 700 °C, a coloração amarela se deve às transições eletrônicas do $Ni^{2+}$. Houve emissão de luz na região azul-verde quando iluminado, indicando propriedades luminescentes.

Palavras-chave: Tungstatos. Catálise. Fotocatálise. Pigmento. Aplicações multifuncionais.

## LIST OF FIGURES

## LIST OF TABLES

**CONTENTS**

# 1. INTRODUCTION

Multifunctional materials are of broad economic and technological interest as they have as their main characteristic the physical properties that allow more than one application. [1; 2] This type of material can be used in various sectors with the advantage of saving time and money since it uses already known and well-established properties of a certain material, also saving investments in new primary research. [3]

Among the materials with multiple applications, we can highlight oxides with semiconducting properties, which have been widely studied due to their good optical properties and the possibility of having their morphology manipulated. Materials such as $Ag_2WO_4$, $CuWO_4$, $NiWO_4$, $ZnWO_4$, ZnO and $TiO_2$ are typical examples of multifunctional oxides. In addition to presenting excellent bactericidal properties, [4] $Ag_2WO_4$ has potential for photocatalytic applications and can be activated with visible light. [5; 6; 7] $CuWO_4$ is often used to oxidize water [8; 9] and has the potential for degradation of organic molecules, such as dyes, pesticides and drugs. [10] $NiWO_4$ is used for hydrodesulfurization [11] and also as electrode for high-performance electrochemical capacitors. [12; 13] $ZnWO_4$ is applied in photocatalysis [14] and scintillators. [15] ZnO is used in dielectric ceramics [16] and also for photocatalytic applications. [17; 18] Finally, $TiO_2$ has exceptional photocatalytic activity in ultraviolet light [19] and is also applied for the production of hydrogen. [20]

In this research, $CuWO_4$, [21] $NiWO_4$, [21] and $ZnWO_4$ [21] were chosen because of their potential for multiple applications, simplicity of synthesis, low cost of production when compared to other semiconductors and high reproducibility. Such characteristics make these oxides economically viable for future applications on an industrial scale.

## 1.1. CATALYSIS

Catalysis consists of a process capable of accelerating a given reaction by alternative means. The increase in the reaction speed occurs as a result of the lower activation energy of the reaction caused by the presence of a catalyst material.

Catalysis is present in several sectors, for example, in the chemical industry for the obtention of nitric acid ($HNO_3$) and sulfuric acid ($H_2SO_4$), in the petrochemical industry for the production of polymers, and in the automotive industry for the production of exhausts capable of converting harmful molecules to the environment from fuels used during burning into ecologically clean by-products. [22]

There are several catalytic reactions. The most common are those caused by metals (dehydrogenation, hydrogenation and hydrogenolysis), [23] basic acids (oligomerization, cyclization, cracking and isomerization) [24] and oxides (selective oxidation). [24]

In general, catalytic reactions are divided into two types: homogeneous and heterogeneous.

### 1.1.1 Homogeneous catalysis

Homogeneous catalysis is basically described as a reaction in which the catalyst is in the same phase as the reaction medium. As an example we can cite the production of sulfur trioxide ($SO_3$) from the oxidation of $SO_2$. This reaction is accelerated by the nitrogen oxide (NO) catalyst, as shown in Equations 1 and 2. [22]

$$O_{2\,(g)} + 2NO_{\,(g)} \rightarrow 2NO_{2\,(g)} \qquad (1)$$

In turn, $NO_2$ reacts with sulfur dioxide ($SO_2$), generating sulfur trioxide ($SO_3$):

$$NO_{2\,(g)} + SO_{2\,(g)} \rightarrow NO_{\,(g)} + SO_{3\,(g)} \qquad (2)$$

The generation of sulfur trioxide by alternative means such as catalysis is useful, because when in contact with water molecules they easily form sulfuric acid, which is used in the petrochemical industry for oil refining, fertilizer and paper production, and water treatment.

On the other hand, homogeneous catalysis may be less advantageous than heterogeneous catalysis as the catalyst consumed in the reaction cannot be reused. [22]

### 1.1.2 Heterogeneous Catalysis

Heterogeneous catalysis is described by a system in which the catalyst is in a different phase from the reaction medium and is not consumed during the reaction.

In this case, the reaction is accelerated when the reagent is adsorbed on the catalyst surface, interacting with its active sites, consequently allowing the chemical reactions capable of accelerating the conversion of initial molecules into other by-products. [22] This process basically consists of 5 steps:

(1) the reagent is diffused through the catalyst surface and pores;
(2) the reagent is adsorbed on the catalyst active sites;
(3) the chemical reaction occurs;
(4) the desorption of formed products occurs;
(5) finally, the formed products are disseminated.

In general, in heterogeneous catalysis there is chemical adsorption (chemisorption) at the active sites present on the catalyst surface. Active sites are related to defects on the surface. [22]

### 1.1.2.1 Catalyst

An important concept regarding the catalyst surface refers to the active sites available for the occurrence of the catalytic reaction, and particle size is known to be a property directly related to the reaction. The restructuring of the catalyst surface is favored by the presence of small particles since the smaller the network of atoms in the material, the more easily the atoms can move in the network, making catalysts advantageous on the nanoscale. In addition to the size, the shape and distribution of the catalyst particles also influence the reaction speed. [24]

It is also known that the mobility of surface oxygen and oxygen vacancies favor the oxidative process. [25]

### 1.1.2.2. Conversion from sulfide to sulfoxide and sulfone

There are studies reporting the oxidation of sulfides to sulfoxides and sulfones through thioanisole via heterogeneous catalysis. As an alternative catalyst, oxide materials based on transition metals have been gaining prominence in this type of reaction. [26]

Thioanisole (methylsulfanylbenzene) is an organic compound that has sulfur in its molecular structure ($C_7H_8S$) and a molar mass of 124.2 g $mol^{-1}$. It is a colorless liquid material soluble in organic solvents. Its melting and boiling points are -15 ° C and +188 ° C, respectively, and it can be the base compound for the study regarding conversion of sulfides to sulfoxides and sulfones. The conversion of the thioanisole molecule can form methyl phenyl sulfoxide ($C_7H_8OS$) and methyl phenyl sulfone ($C_7H_8O_2S$), according to Figure 1.

Figure 1- Thioanisole molecule generating sulfoxide and sulfone

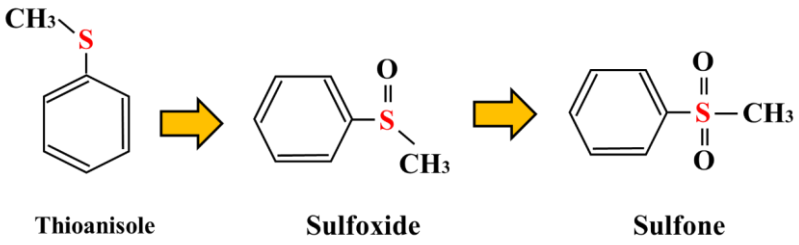


Source: Author

### 1.1.2.3. Hydrogen peroxide ($H_2O_2$)

Hydrogen peroxide ($H_2O_2$) is a non-toxic liquid that can be diluted in water. It is a well-known and widely used oxidizing agent since it has water and oxygen molecules–which are ecologically-clean molecules–as by-products of the reaction. More specifically, when heated to temperatures above 80 ° C it decomposes into water and oxygen. [27] [25]

In 1912, it was discovered that in addition to water and oxygen, more reactive intermediate products can be formed from the decomposition of $H_2O_2$: hydroxyl (OH•) and peroxyl ($HO_2$•) radicals. [28] The $H_2O_2$ decomposition reactions are described in Equations (3 - 5).

$$H_2O_2 \rightarrow 2OH\bullet \quad (3)$$

$$OH\bullet + H_2O_2 \rightarrow HO_2\bullet + H_2O \quad (4)$$

$$OH\bullet + HO_2\bullet \rightarrow H_2O + O_2 \quad (5)$$

The oxidation reactions of organic compounds involve two essential phenomena: mass and surface oxygen mobilities. The greater mobility of oxygen tends to cause the migration of active oxygen species through the catalyst structure, leading to greater oxidation activity. [29] Moreover, the $H_2O_2$ adsorption intensity can be increased by oxygen vacancies on the catalyst surface, which in turn facilitate the generation of active oxygen species, leading to an increased catalytic activity. [29]

## 1.2. PHOTOCATALYSIS

Photocatalysis is an advanced oxidative process (AOP) described as a degradation reaction accelerated by the action of a catalyst material that can be photoactivated with electromagnetic radiation. [30]

The reaction occurs when electromagnetic radiation, usually ultraviolet light or visible light, reaches the catalyst, generating ($h^+$) and ($e^-$) charge carriers and / or radicals with high oxidation / reduction power. The radicals generated, the hole ($h^+$) of the valence band (VB) and the electron ($e^-$) of the conduction band (CB) are highly reactive, little selective and with a high potential for degradation of organic compounds. [30]

Specifically, the hydroxyl radical (OH•) has a relatively high oxidation potential when compared to other known species. For this reason, it is one of the main responsible for the degradation of organic molecules. [31] The values of standard reduction potential of some reactive species are shown in Table 1.

Table 1- Standard reduction potentials of some reactive species [31]

| **Species** | **E° (Volts)** |
|---|---|
| Hydroxyl radical (HO•) | + 2.80 |
| Ozone ($O_3$) | + 2.07 |
| Hydrogen peroxide ($H_2O_2$) | + 1.77 |
| Hypochlorite ($ClO^-$) | + 1.43 |
| Perhydroxyl radical ($HO_2$•) | + 1.42 |
| Chlorine ($Cl_2$) | + 1.36 |
| Oxygen ($O_2$) | + 1.23 |

Source: Author

Photocatalysis can be divided into two types: homogeneous and heterogeneous photocatalysis.

### 1.2.1. Homogeneous photocatalysis

The homogeneous photocatalysis occurs when the catalyst is in the same phase as the reaction medium. The reactions with hydrogen peroxide ($H_2O_2$ / UV or Vis), ozone ($O_3$ / UV or Vis) and photo-Fenton are examples of homogeneous photocatalysis based on the generation of hydroxyl radicals (OH•). [32]

The photocatalysis with $H_2O_2$ happens through direct oxidation of the hydrogen peroxide molecule when the system is irradiated with UV or visible light, forming two hydroxyl radicals, which in turn are capable of oxidizing organic molecules (OM) and generating mostly water ($H_2O$) and carbon dioxide ($CO_2$), as shown in Equations 6 and 7. [32]

$$H_2O_2 + h\nu \rightarrow 2OH\bullet \quad (6)$$

$$OH\bullet + OM \rightarrow H_2O + CO_2 \quad (7)$$

When in contact with organic molecules (OM), the photocatalytic reactions using ozone and in the presence of radiation ($O_3$/UV or Vis) occur as follows (Equations 8 to 12), [31; 32] mainly resulting in water and carbon dioxide.

$$O_3 + H_2O + h\nu \rightarrow O_2 + H_2O_2 \quad (8)$$

$$H_2O_2 + h\nu \rightarrow 2HO\bullet \quad (9)$$

$$O_3 + OH^- \rightarrow O_2^- + HO_2\bullet \quad (10)$$

$$O_3 + HO_2\bullet \rightarrow 2O_2 + OH\bullet \quad (11)$$

$$OH\bullet + OM \rightarrow H_2O + CO_2 \quad (12)$$

The homogeneous photo-Fenton photocatalytic reactions ($H_2O_2$ / $Fe^{2+}$ / UV or Vis) occur as shown by Equations 13 and 14. [31]

$$Fe^{3+} + H_2O_2 + h\nu \rightarrow Fe^{2+} + H^+ + OH\bullet \quad (13)$$

$$OH\bullet + OM \rightarrow H_2O + CO_2 \quad (14)$$

### 1.2.2. Heterogeneous photocatalysis

The heterogeneous photocatalysis is based on the activation of a solid-state catalyst dispersed in an aqueous solution (distinct phases). The catalyst is used to accelerate the kinetics of a reaction to convert complex organic molecules into other by-products less harmful to the environment. In this case, different from the homogeneous photocatalysis the catalyst is not consumed during the reaction, being possible its reuse. [33] Thus, in heterogeneous photocatalysis, the degradation can be triggered by the presence of three essential agents: a solid catalyst, electromagnetic radiation and water molecules. [34]

#### 1.2.2.1. Catalyst

The catalyst must have semiconducting properties since this type of material has the necessary electronic configuration to excite electrons of the valence band (VB) and promote them to the conduction band (CB) when they receive energy $E = h\nu$ equal to or greater than its band gap energy value (BG). [35]

It is known that the BG of the semiconductor materials has an intermediate energy value, being more easily excited than insulator materials and less easily excited than conductor materials, according to Figure 2. Thus, the semiconductors fall in the BG range corresponding to the ultraviolet and / or visible radiation energy. The advantage of working with materials that can be excited by these types of radiation is that they are more accessible and relatively inexpensive energy sources as they compose most of the solar radiation. [34]

Figure 2- Structure of band gap energies for insulator, semiconductor and conductor materials [36]

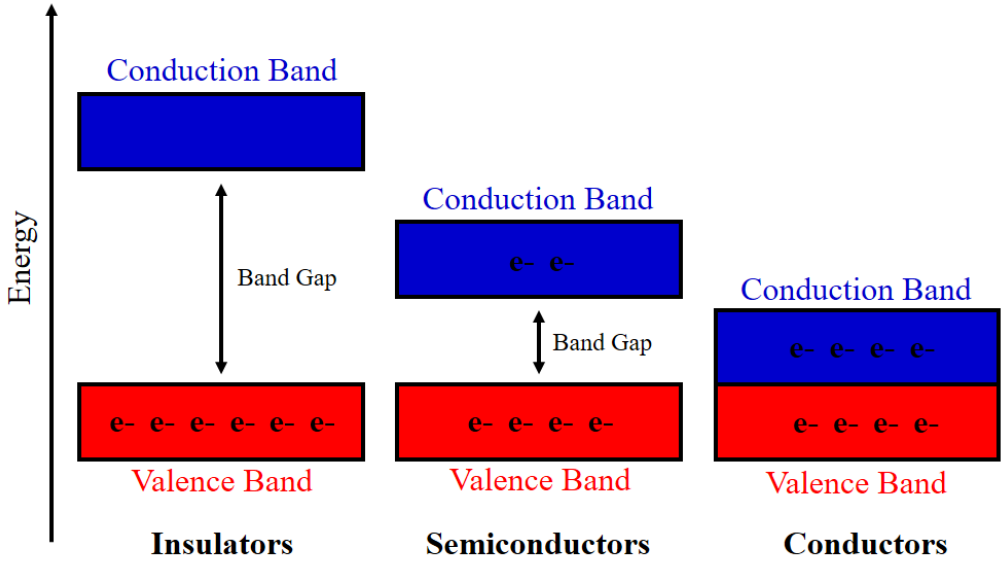


Source: Author

When the catalyst receives energy (E = hν) greater than or equal to its band gap (BG) value, the electrons from the VB are promoted to the CB, leading to the formation of the so-called electron-hole ($h^+ + e^-$) pair, which is the primary phase for the occurrence of the photocatalytic process, as shown in Equation 15. The hole ($h^+$) formed in the VB is able to oxidize water molecules adsorbed on the catalyst surface, generating OH• radicals, while the electron ($e^-$) present in the CB is able to reduce oxygen molecules ($O_2$) adsorbed on the semiconductor surface, forming superoxide radicals ($O_2^{\bullet -}$), according to Equations 16 and 17. [37] Both radicals have the potential to degrade a wide range of organic molecules. [33] The basic mechanism of heterogeneous photocatalysis is displayed in Figure 3.

$$h\nu \geq E_{BG} \rightarrow h^+ + e^- \quad (15)$$

$$h^+ + H_2O_{ads} \rightarrow HO\bullet + H^+ \quad (16)$$

$$e^- + O_{2\ ads} \rightarrow O_2^{\bullet -} \quad (17)$$

Figure 3 - Basic mechanism of heterogeneous photocatalysis. In the semiconductor, electrons are promoted from the VB to the CB through energy radiation, hν. The hole ($h^+$) and electron ($e^-$) interact with water and $O_2$ molecules adsorbed on the catalyst surface, forming the HO• and $O_2$•$^-$ radicals

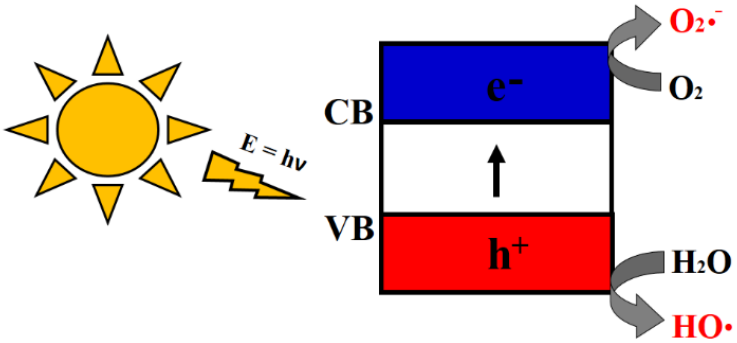


Source: Author

Although not fully understood yet, there is evidence that the holes ($h^+$) of the VB can degrade organic molecules (OM) through: (1) direct degradation (Equation 18); [38; 39]

$$h^+ + OM \rightarrow CO_2 + H_2O \quad (18)$$

or (2) generation of hydroxyl radicals (OH•), which are highly oxidizing. Hydroxyl radicals are generated when the hole ($h^+$) interacts with water molecules ($H_2O$) adsorbed on the catalyst surface, forming OH• and $H^+$, [39] as seen in Equation 19. In turn, the OH• radical is capable of degrading OM (Equation 20). The product of both processes is degradation, which mostly results in water ($H_2O$) and carbon dioxide ($CO_2$). [38; 39]

$$h^+ + H_2O_{ads} \rightarrow OH\bullet + H^+ \quad (19)$$

$$OH\bullet + OM \rightarrow H_2O + CO_2 \quad (20)$$

The possible mechanisms of degradation of organic molecules (OM) via holes ($h^+$) of the valence band are displayed in Figure 4.

Figure 4- Degradation mechanism via holes ($h^+$) of the VB through direct and indirect oxidations

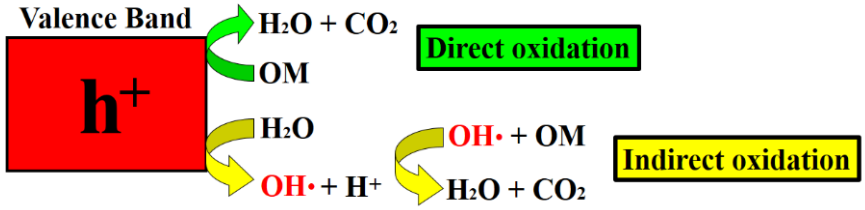


Source: Author

In addition to the OH• radical, the $HO_2$• and $O_2$•$^-$ radicals also have the potential to degrade organic molecules. It is important to mention that these radicals can be generated from the free electrons available in the conduction band.

Electrons ($e^-$) from the CB are able to reduce oxygen molecules ($O_2$) to superoxide radical ($O_2$•$^-$), as observed in Equation 21. [39]

$$e^- + O_2 \rightarrow O_2\bullet^- \quad (21)$$

There are three ways of degrading organic molecules via electrons in the conduction band: (1) when the superoxide radical ($O_2$•$^-$) interacts directly with the organic pollutant (Equation 22); (2) when the superoxide radical bonds to the $H^+$ obtained in the oxidation process in the VB, forming the $HO_2$• radical (Equation 23) [39] and (3) when two $HO_2$• radicals bond to form $H_2O_2$ (Equation 24), which in turn breaks to form the oxidizing radical (OH•) (Equation 25).

$$O_2\bullet^- + OM \rightarrow CO_2 + H_2O \quad (22)$$

$$O_2\bullet^- + H^+ \rightarrow HO_2\bullet \quad (23)$$

$$HO_2\bullet + HO_2\bullet \rightarrow H_2O_2 + O_2 \quad (24)$$

$$H_2O_2 \rightarrow 2\ OH\bullet \quad (25)$$

From $H_2O_2$ (Equation 26 – 28):

$$H_2O_2 + h\nu \rightarrow 2HO\bullet \quad (26)$$

$$H_2O_2 + O_2\bullet^- \rightarrow HO\bullet + OH^- + O_2 \quad (27)$$

$$H_2O_2 + e^- \rightarrow HO\bullet + OH^- \quad (28)$$

The three possible mechanisms involved in the conduction band are displayed in detail in Figure 5.

Figure 5- Degradation mechanisms via electrons ($e^-$) of the CB

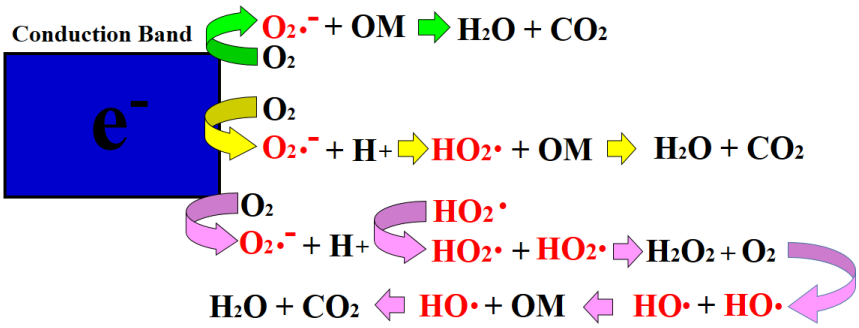


Source: Author

*1.2.2.2.Scavengers*

For the photocatalysis mechanism to be efficient, the VB holes and CB electrons must remain available in order to make the reaction happen. It is known that the promotion of electrons from the VB to the CB triggers a natural process of electron recombination that occurs in the semiconductors. In other words, the CB electrons rapidly decrease to their lowest energy state, which is in the VB, eliminating oxidizing and reducing sites (Figure 6a). Therefore, for the degradation to occur effectively, the recombination must be minimized as much as possible.

The use of so-called scavengers can appear as an alternative to this process. Scavengers are materials capable of either capturing electrons from the CB or bonding to the holes in the VB, preventing their recombination and return to the VB, thus making oxidizing or reducing

sites available for the reaction to occur. Figure 6b exemplifies a system in which silver ions are used to capture CB electrons, making the VB holes available so as to allow the oxidation reactions necessary for the degradation of organic molecules.

Figure 6- (a) Electron-hole pair recombination process and (b) use of $Ag^{+}$ as electron scavenger

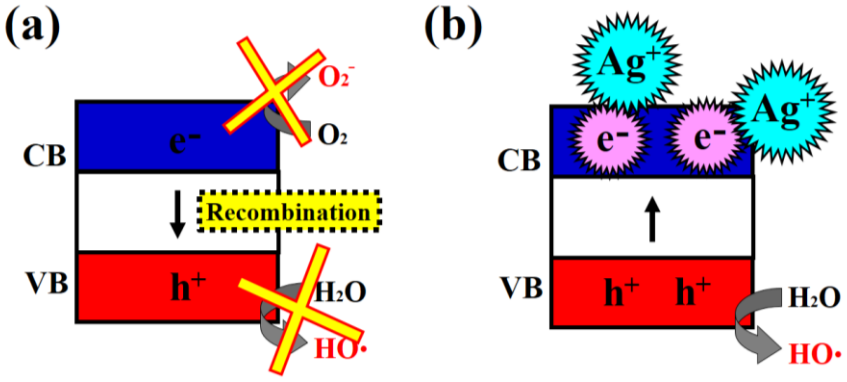


Source: Author

In the literature, it is possible to find some studies reporting the degradation of organic molecules by heterogeneous photocatalysis using photoactive catalysts in the ultraviolet region, such as P25, a commercial $TiO_2$-based material. [40; 41; 42] However, only a minor percentage of solar radiation is composed of UV, causing the system to be energetically and economically disadvantageous and less ecological when compared to systems that use only visible radiation. [43] Therefore, it is feasible to use semiconductor catalysts with low band gap values, allowing the system to work effectively by means of visible radiation.

Due to its low band gap (approximately 2.3 eV), [44] $CuWO_4$ is a semiconductor material that shows potential for photocatalytic applications using only visible radiation since its band gap value is within the range of the visible radiation spectrum, as observed in Figure 7. Therefore, a photoactive catalyst in the visible region of the electromagnetic spectrum may be able to effectively and relatively cheaply degrade unwanted molecules. [45]

Figure 7- Visible radiation spectrum wavelength and energy and $CuWO_4$ band gap

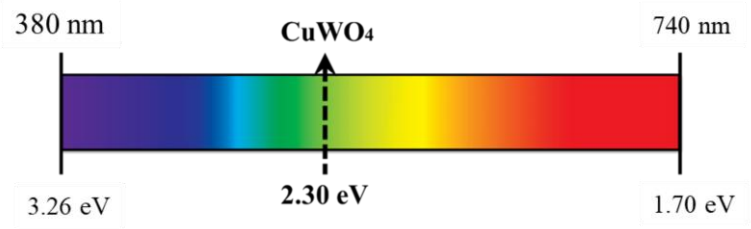


Source: Author.

To make photocatalysis viable for future applications on an industrial scale, it is necessary that the photocatalytic system be efficient and low-cost. In order to meet these two requirements, it is reasonable to use a catalyst with a band gap value between 1.59 and 3.26 eV as it is the energy range corresponding to the visible light spectrum.

The use of a material that is photoactive under visible radiation is of great technological interest since the sun mainly emits this type of radiation, causing the degradation of organic pollutants to occur anywhere that receives the sunlight incidence, thus discarding the use of expensive and complex systems that are necessary to radiate ultraviolet light.

## 1.3. PIGMENTS

Pigments are solid materials that are insoluble in the medium into which they will be incorporated. They are able to absorb part of the visible light wavelength emitted over it and reflect another wavelength that corresponds to a specific color [46] and can be seen with the naked eyes (Figure 8).

Figure 8- The visible radiation emitted by the sun reaches the pigment. The pigment absorbs blue and yellow radiations and reflects red radiation. The eyes capture the red color

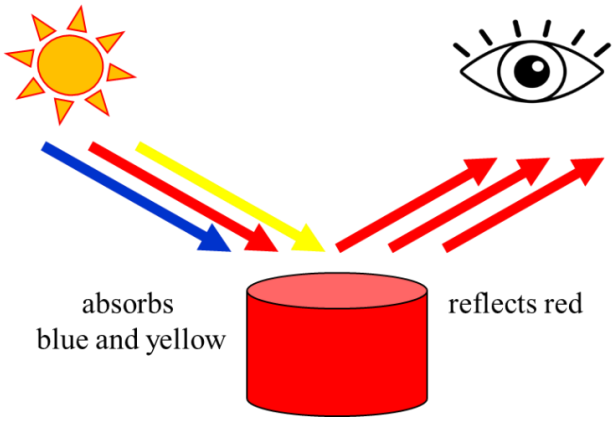


Source: Author

The colored aspect observed in the materials is described mainly by the way the color reacts to the absorption and scattering of the light they receive. The observed color intensity is governed by the absorption coefficient K, which is inversely proportional to the scattering coefficient S, as described by Equation 29. The values are related to the reflectance data (r). [47]

$$\frac{K}{S} = \frac{(1-r)^2}{2r} \tag{29}$$

Materials with high ability to reflect light (little absorption) are generally white and light-colored materials with a very small K value. Conversely, very dark-colored and even black materials reflect little light (high absorption) and have a very small S value.

Pigments can be classified as natural or synthetic. Natural pigments generally come from plants and minerals and are not much used on an industrial scale mainly due to their color variation and low durability. [46] On the other hand, synthetic pigments are characterized by their ability to standardize color and increase their own resistance, which can be beneficial for industrial applications.

In crystalline pigments, color can be perceived because of the electronic transitions involving unsaturated molecules or when there are carbon molecules bonded to oxygen or sulfur atoms. [48] The presence of any transition metal in their crystalline structure can cause a color change. Thus, the color that the eyes can capture is a result of electronic transitions that occur within the atom. There are two possible situations that can arise. One of them is when the "d" orbital is partially filled. [49] In such a case, the radiation corresponding to the visible light has enough energy to promote the excitation of electrons from a lower to a higher energy level. When the electrons undergo relaxation, they emit photons with energy corresponding to a specific color. The other situation is when the "d" orbital is completely filled ($d^{10}$). In this configuration, so that the electrons can be promoted from a lower to a higher energy level it is necessary to provide them with greater energy (radiation with a shorter wavelength), that is, these electrons will not be excited with light visible. For this reason, some materials having transition metals in their structure are seen as white, [50] as is the case of $TiO_2$.

In general, the industry consumes inorganic pigments. They are mainly used to color paints, cosmetics, ceramics, plastics, enamels and varnishes. [51] For these purposes, the properties of the pigments must be controlled since they can influence gloss, covering power and durability. [49]

In the industry, a pigment is considered of quality if it has thermal and chemical stability. In other words, its color and gloss must be durable and resist exposure to sunlight and heat. In addition, it must be chemically inert and resist contact with air and moisture. [49]

Currently, in a search of better properties for pigments, particle size has been a property of great relevance since studies have shown that materials on the nanoscale are gaining prominence due to their capability to generate a product of superior quality in comparison with those previously found on the market. [52]

### 1.3.1. Particle size

Given the direct influence of particle size on the characteristics of a pigment, in recent years the manufacture of synthetic pigments with controlled properties has been extensively studied. [52]

The size of a particle is directly related to its optical properties, such as opacity, gloss and resistance to bad weather. [53]

Using Weber's formula (Equation 30), it is possible to predict the ideal particle size capable of causing maximum light scattering for each system (maximum opacity). In the formula, "D" corresponds to the ideal particle size for a pigment with high refractive index, "λ" is the wavelength of the light incidence on it, and "n1" and "n2" are relative to the refractive index of the pigment and the environment with which it is associated. [53]

$$D = \frac{2\lambda}{\pi(n1-n2)} \tag{30}$$

As an example, considering a pigment that has been extensively explored, such as $TiO_2$ in rutile phase, it is possible to estimate its ideal particle size. As it can be seen in Table 2, the "n1" value corresponding to the refractive index of $TiO_2$ (rutile) is 2.70. The refractive index of the medium in which it is dispersed, "n2", when considering water as the dispersion medium has a value of 1.33.

Table 2- Refractive index of pigments

| **Material** | **Refractive index (n)** |
|---|---|
| $SnO_2$ | 2.04 [53] |
| $ZrO_2$ | 2.40 [53] |
| $ZrSiO_4$ | 1.85 [53] |
| $TiO_2$ (anatase) | 2.50 [53] |
| $TiO_2$ (rutile) | 2.70 [53] |
| Water | 1.33 [54] |

Source: Author

By applying Weber's equation and taking into account the entire wavelength corresponding to visible light (from 380 nm to 740 nm), an ideal particle size range between 169 and 329 nm can be obtained, as shown in Figure 9.

Figure 9- Ideal size for the rutile $TiO_2$ pigment particle dispersed in water according to Weber's equation

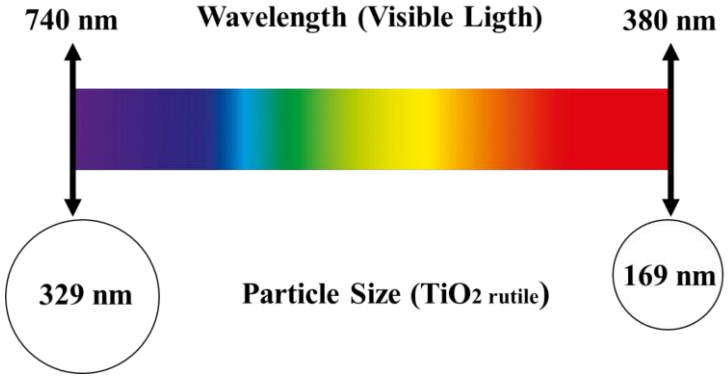


Source: Author

Opacity is an important parameter for pigments and can be described as the covering power of a given surface. The opacity is said to be bad when the pigment cannot cover the entire substrate on which it was applied. In contrast, it is considered good when the pigment film covers the entire substrate.

It is worth mentioning that opacity is influenced by the particle size of the powder that will be used to give color. Figure 10 shows the ideal particle size range to increase its ability to completely hide the substrate on which the pigment is being applied. So that the degree of opacity is high and light cannot reach the substrate, the refractive index of the pigment must be considerably higher than that of the medium in which it was dispersed. [55]

When the particles are approximately half the size of the radiation wavelength that they will receive, they can spread light more efficiently, and consequently maximize the pigment opacity. Therefore, very small (below 169 nm) or very large particles (greater than 329 nm) will absorb more and more and spread less and less radiation, resulting in less opacity, as shown in Figure 10.

Figure 10- Relationship between particle size, scattering, opacity and absorption in relation to visible radiation

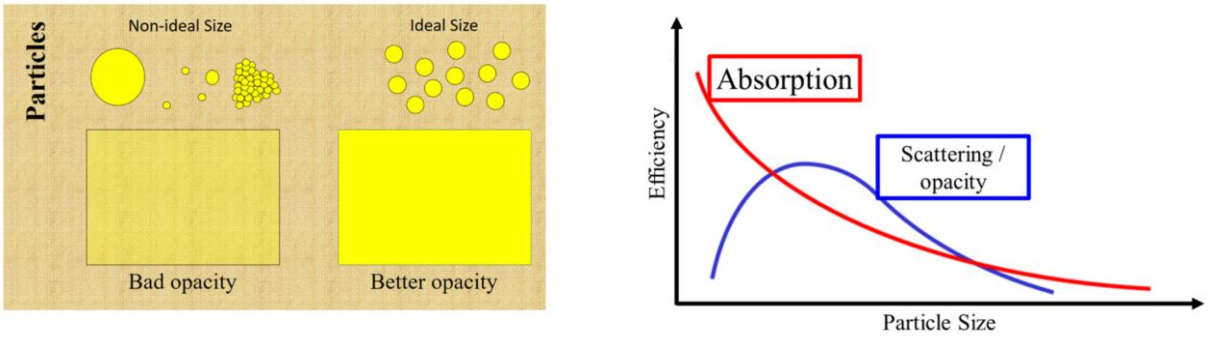


Source: Adapted [53]

Therefore, it is economically viable to optimize the particle size for pigment production. In this way, the pigment concentration used to cover a substrate will be much lower than when using particles with random sizes since too large or too small particles, or clusters of particles, need a higher concentration of pigment to achieve the same covering. [53] This scheme is illustrated in Figure 11.

Figure 11- Curve showing the relationship between particle size and opacity, gloss and durability

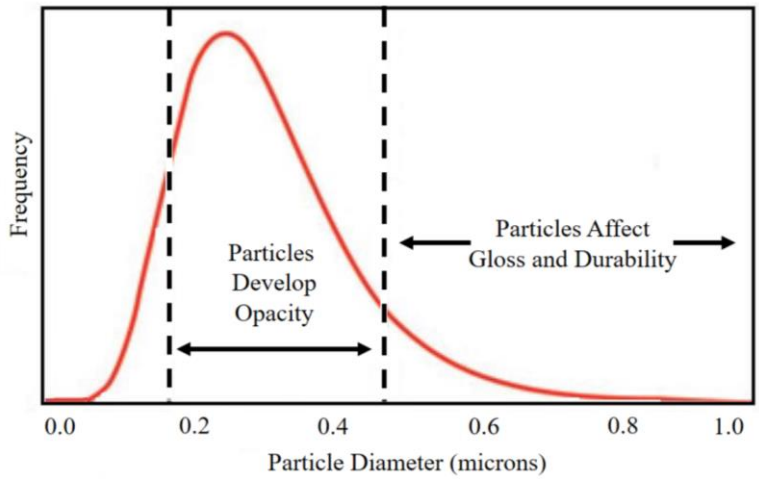


Source: Adapted from [53]

Gloss and durability properties are also associated with particle size and how these particles are dispersed in the film. Films containing a narrow particle size gradient have a more uniform finish, which in turn makes them more resistant. Moreover, when the particles are small, they are able to spread more light, resulting in a glossy aspect. [53]

The use of large and/or non-uniform particles and / or clusters of small particles can decrease the covering power, making the film less resistant. These characteristics can displace pieces of the covering more easily, thus making the surface also less glossy. [56]

The agglomeration of particles occurs as a result of the adhesion force (related to the high surface area) that predominates among the too small-sized particles. As a consequence, there is less opacity, gloss and durability. [56] Figure 12 shows the relationship between the force that induces particle adhesion and the particle size.

Figure 12- Relationship between particle size and particle adhesion force

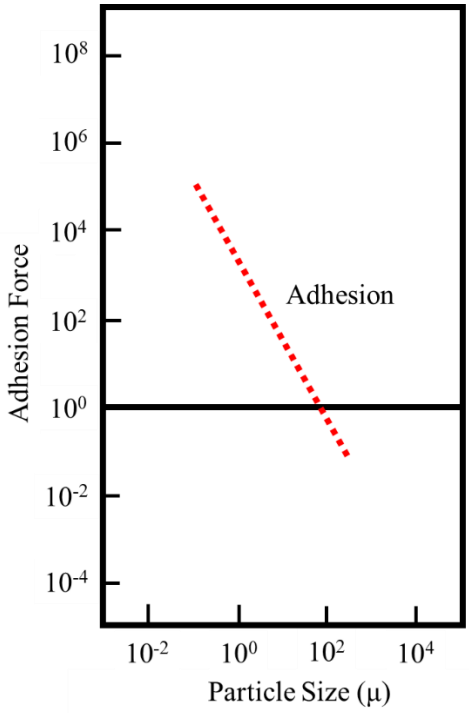


Source: Adapted from [53]

It can be concluded that there are several variables involved in the manufacturing process of a pigment that directly influences its characteristics. Therefore, for industrial applications it is necessary to standardize such variables so that they can later be replicated. To this end, there is a specific system that accurately measures the color of the pigments.

### 1.3.2. Color standardization

Color perception can be influenced by a number of factors. Depending on the sensitivity of the retina, the perception may be altered by the presence of different colors around the observed object. Thus, it is difficult to describe a color accurately with the naked eye and replicate it.

In this way, to meet the demand for pigments in the industrial sector it is necessary to use a measurable technique to establish a well-defined color standard, such as those using spectra acquisition. The spectrophotometer, for example, is based on the emission of white monochromatic light on the object of study, which in turn reflects the light that was not absorbed, reaching the galvanometer, a photosensitive sensor capable of measuring the reflected light.

To measure the color portion of each object, the *Commission Internationale d'Eclairage* (International Commission on Illumination) established a technique using three color coordinates based on *L*, *a* and *b*. [57] The parameter *L* ranges from 0 to 100 and represents the gradient from black (L = 0) to white (L = 100). The parameter *a* goes from green (- a) to red (+ a). Finally, the coordinate *b* ranges from blue (- b) to yellow (+ b), [57] as shown in the diagram of Figure 13.

Figure 13- Color system described by the standard from Hunter Associates Laboratory, Inc

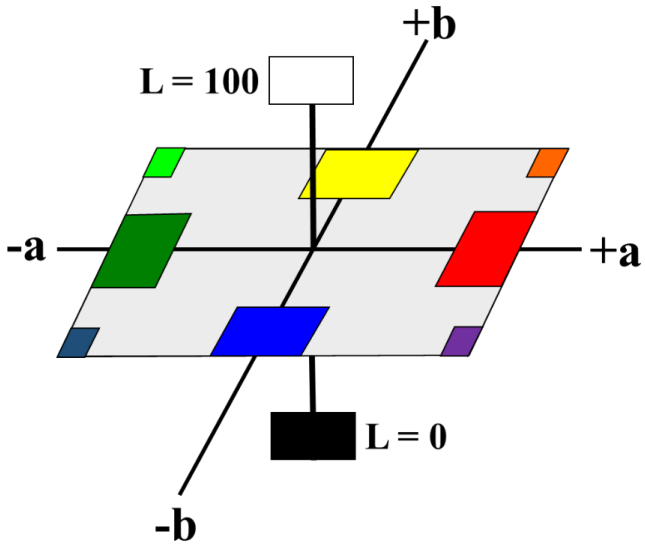


Source: Author

Using the calculation standard DIN6170, ASTM D2244, the color value (ΔE) can be determined by Equation 31. Δ*L*, Δ*a* and Δ*b* represent the variation of the parameters *L*, *a* and *b*, respectively, in relation to a pre-established standard.

$$\Delta E = \sqrt{\Delta L^2 + \Delta a^2 + \Delta b^2} \quad (31)$$

### 1.3.3. Yellow pigments

Among the dyes most used in the ceramic industry, we can highlight the yellow dyes. The most common yellow pigments are cadmium sulfide (CdS), which is mainly used in jewelry and to color plastics and ceramics, [58] and lead chromate ($PbCrO_4$), which is used in traffic lanes and is considered one of the responsible dyes for the environmental pollution by heavy metals. [59] These pigments have toxic metals in their composition, in addition to being unstable and possibly losing color due to external stimuli. Such pigments have been used on a large scale, however, in view of the constant concern regarding health and environment those considered toxic and possibly carcinogenic have been losing space in the market. [57] Thus, there is a need to seek alternative pigments that are efficient, economically viable and ecologically appropriate to replace the yellow ones.

In this way, nickel tungstate appears as an alternative to yellow pigments harmful to health and environment. Besides being yellow, it withstands high temperatures, [60] is relatively simple to manufacture, has low production costs [61] and is less toxic than pigments composed of heavy metals. Additionally, it may have one more advantage: luminescent properties. [62]

### 1.3.4. Luminescent pigments

Pigments with luminescent properties are used mainly in traffic signs [63] and artistic paintings [51] as well as to mark paper such as money so as to prevent counterfeiting. [64] Luminescent materials are capable of emitting light without the need of heating.

# 2. OBJECTIVES

## 2.1.GENERAL OBJETIVES

Synthesis and characterization of Cu, Ni and Zn tungstates for mulfunctional applications: catalysis, photocatalysis and pigment.

## 2.2.SPECIFIC OBJECTIVES

The propose of the study reported in paper 1 was to investigate the “heterogeneous catalysis for thioanisole oxidation using hydrogen peroxide and copper, nickel and zinc tungstates obtained by the polymeric precursor method”. The system composed of three types of semiconductors ($CuWO_4$, $NiWO_4$ and $ZnWO_4$) was studied due to their catalytic responses for the conversion of sulfides, of less economic and environmental interest, into sulfoxides and sulfones, which are by-products used in the agricultural and pharmaceutical industry.

The propose of the study reported in paper 2 was the "Influence of the synthesis method on $CuWO_4$ nanoparticles for photocatalytic application". The properties obtained due to the different methods of synthesis of $CuWO_4$ were studied in function of its photocatalytic response for degradation of the organic molecule of rhodamine-B dye. Due to its band gap of approximately 2.4 eV, photoexcitation can occur with radiation in the visible range of the electromagnetic spectrum, which makes the system energetically favorable.

The propose of the study in paper 3 was the “$NiWO_4$ powders prepared via polymeric precursor method for application as ceramic luminescente pigments”. The system was also studied for applications in the area of luminescent pigments due to its promising photoluminescent properties.

# 3. PAPER 1: HETEROGENEOUS CATALYSIS FOR THIOANISOLE OXIDATION USING HYDROGEN PEROXIDE AND COPPER, NICKEL AND ZINC TUNGSTATES OBTAINED BY THE POLYMERIC PRECURSOR METHOD

Naiara Arantes Lima [1], Lorena Dariane da Silva Alencar [2], Gabryella Cerri Mendonça [1], Alexandre Mesquita [3], Augusto Vieira Pontes Silva [4], Marcelo Gonçalves Rosmaninho [4], Jason Guy Taylor [4], Humberto Vieira Fajardo [4], Leonardo César Moraes [5] and Maria Inês Basso Bernardi [1]

[1] Institute of Physics of São Carlos, University of São Paulo – USP, 13560-970, São Carlos, SP, Brazil

[2] Federal Institute of Mato Grosso do Sul, 79200-000, Aquidauana, MS, Brazil

[3] Institute of Geosciences and Exact Sciences, São Paulo State University – Unesp, 13506-900, Rio Claro, SP, Brazil

[4] Department of Chemistry, Federal University of Ouro Preto – UFOP, 35400-000, Ouro Preto, MG, Brazil

[5] Department of Botany, Institute of Biological Sciences, Federal University of Minas Gerais – UFMG, 31970-901, Belo Horizonte, MG, Brazil

Preprint Research Square – DOI: 10.21203 / rs.3.rs-24759 / v1

Submitted in Bulletin of Materials Science: 19 November, 2020

Figure 14- Graphical abstract of paper 1

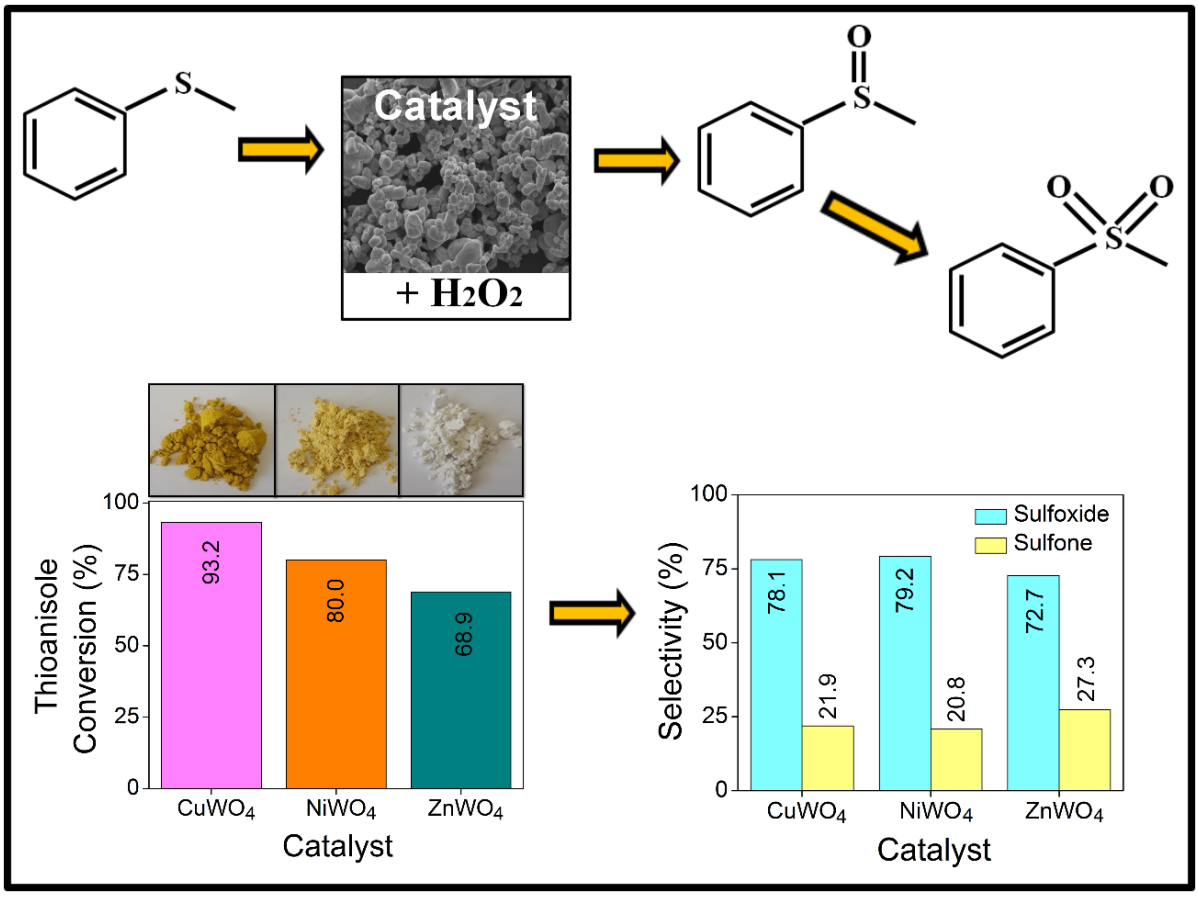


Source: Author


## ABSTRACT

The catalytic potential of copper, nickel and zinc tungstate powders was investigated in the thioanisole oxidation with $H_2O_2$ toward its sulfoxide and sulfone. Copper tungstate was the most efficient in the process, since it showed higher oxygen vacancy, ability to increase surface oxygen mobility and enhancement of $H_2O_2$ intensity adsorption on the surface, which in turn increased the conversion and selectivity of the process. The addition of 0.1 mL of hydrogen peroxide enhanced the conversion and increased the amount of sulfone produced. The ideal reaction time was found to be 12 hours, and the optimum temperature was 75 °C.


Keywords: Sulfide. Sulfone. sulfoxides, $H_2O_2$, $H_2$-TPR.

## 3.1. INTRODUCTION

The oxidation of sulfides to sulfoxides and sulfones is considered to be an important reaction that has been used to synthesize several valuable sulfur-containing chemical intermediates and products. These compounds are used in industry to produce pharmaceuticals, agrochemicals and polymeric materials, among others. [65] The catalytic oxidative desulfurization process (sulfoxidation reaction) is typically carried out to remove sulfur-based impurities from crude oil. [66] The selective detoxification of organosulfide-containing chemical nerve agents to less toxic sulfoxide compounds also has important applications. [67] Efforts have been made towards the development of catalytic methods using homogeneous catalysts to enable the oxidation of sulfides to sulfoxides and/or sulfones. [68; 69; 70; 71; 72; 73; 74] The more environmentally-friendly protocols based on heterogeneous catalysts in conjunction with hydrogen peroxide as oxidant have been considered attractive alternatives. The oxidation of thioanisole using $H_2O_2$ and heterogeneous catalysts has been described in the scientific literature. Examples include: titanium-containing mesoporous silica nanoparticles, [75] isotetramolybdate-supported metal carbonyl material, [76] $[Cu(terpy)]^{2+}$ complexes encapsulated into Na-Y zeolite, [77] copper nanoparticles immobilized on nanocellulose, [78] polyoxomolybdates, [79] Mo(VI) Schiff base complex anchored on $Fe_3O_4$ nanoparticles, [74] polyoxometalate-based frameworks, [80] vanadium incorporated into disordered mesoporous nanocrystalline titania, [70] and $VOx/SiO_2$ and $VOx/Al_2O_3$ catalysts. [73; 74; 81; 82] Rare but noteworthy studies report examples describing the use of molecular oxygen such as sole oxidant with $BaRuO_3$, [83] immobilized metalloporphyrins [84] or molybdenum-doped $\alpha$-$MnO_2$ [85] as heterogeneous catalysts. Some of tungsten-based catalytic systems have proved to effectively promote sulfide oxidation in a homogeneous medium. [86; 87] However, the heterogeneous catalytic protocols are more desirable given their potential to be recovered and reused in further cycles.

Metal tungstates–whose general formula is $MWO_4$, where M symbolizes a bivalent cation–have been applied to catalysis due to their peculiar physical and chemical properties. [88] In this work, we report the synthesis of $CuWO_4$, $NiWO_4$ and $ZnWO_4$ powders by the polymeric precursor method, considered a low-cost processing procedure with high reproducibility compared to other chemical methods, which has been successfully used in the synthesis of nanoparticles of different oxides. This method consists of the chelation of cations by a hydrocarboxylic acid (typically citric acid), followed by a polyesterification reaction using a

glycol (typically ethylene glycol), [89] resulting in precursor resins containing cations randomly distributed all over the polymer. [90] Additionally, we present herein some promising results on the application of $MWO_4$ (M = Cu, Ni and Zn, respectively) to catalyze thioanisole oxidation with aqueous $H_2O_2$.

## 3.2. METHODS

### 3.2.1. Synthesis of tungstates

In a typical procedure, $H_2WO_4$ was dissolved in distilled water with pH of 8-11 at a temperature of 70 ºC. Then, an aqueous solution of citric acid was added, resulting in a solution containing tungsten citrate. The addition of $Cu(NO_3)_2.3H_2O$ or $Ni(NO_3)_2.6H_2O$ or $Zn(NO_3)_2.6H_2O$ precursor to the solution under constant stirring enabled the synthesis of the polymeric resin at a temperature of 100 ºC. The polyesterification reaction was promoted after the addition of ethylene glycol, resulting in a citric acid:metal molar ratio of 3:1 and citric acid:ethylene glycol ratio of 3:2 (mass ratio). In the final step, the as-prepared polymeric precursor solution underwent a heat treatment at 400 ºC for 4 h at a heating rate of 10 ºC $min^{-1}$. The obtained powder was grounded in an agate mortar for its deagglomeration. The resulting compound, denoted as precursor powder, was heat-treated at 700 °C.

### 3.2.2. Characterization of samples

The thermal decomposition and crystallization of the as-obtained powders were studied by thermal analysis techniques, such as TG (thermogravimetric analysis) (Netzsch STA 409C) and DSC (differential scanning calorimetry), under oxygen atmosphere and at a heating rate of 10 °C $min^{-1}$. The material chosen to be used as reference during the thermal analyses was $Al_2O_3$. In order to get a significant insight into its phase development, the precursor powder was heat-treated at a temperature of 700 ºC for 2 h in an electric furnace under air atmosphere and at a heating rate of 10 ºC $min^{-1}$. Aiming to obtain information about the crystalline phase of the studied samples, X-ray Diffraction (XRD) measurements were performed at room temperature in the range of 2θ = 20 to 60 º, with a step of 0.02 º and at a scanning speed of 2 º $min^{-1}$. The

diffraction patterns were determined by a Rigaku diffractometer (model ULTIMA IV) using Cu Kα radiation. Nitrogen adsorption-desorption measurements of the as-obtained samples were carried out at 77 K using a Micromeritics ASAP 2020 adsorption apparatus. The Langmuir model was used to determine the surface areas. The optical properties of the samples were also studied by UV-VIS characterization using a Shimadzu-UV-1601 PC spectrophotometer in the range of 220 to 800 nm. A field-emission gun scanning electron microscope (FEG-SEM Supra 35, Zeiss, Germany) operating at 3 kV was employed for the microstructural characterization. A Thermal Jarrel-Ash Monospec monochromator and a Hamamatsu R955 photomultiplier were used to collect the photoluminescence (PL) spectra. A krypton ion laser (Coherent Innova 200) operating at an exciting wavelength of 350.7 nm was employed in the measurements, and its output was maintained at 500 mW, with a reaching effectiveness of ~14 mW. Hydrogen temperature-programmed reduction ($H_2$-TPR) measurements were obtained on a Quantachrome ChemBET-TPR/TPD instrument at a temperature range of 50 to 1100 °C and heating rate of 10 °C $min^{-1}$, using a 5% $H_2/N_2$ mixture (25 mL $min^{-1}$ of flow rate) as reducing gas and 50 mg of sample. The analysis of the resulting curves was performed using Origin 9.0.0 software, having the observed peaks adjusted according to the Gaussian model.

### 3.2.3. Catalytic measures

In order to study the liquid phase oxidation reactions of thioanisole (Sigma-Aldrich), we used a single-neck round-bottom flask equipped with a magnetic stir bar placed on a hot plate stirrer with an oil bath at 25, 50 and 75 °C. This flask received 10 mg of catalyst, 5 mL of acetonitrile (Synth PA-ACS) used as solvent, 0.10 mL of thioanisole, and finally amounts of $H_2O_2$ (Synth PA, 29% v/v) in the volume range of 0.025-0.1 mL. The reaction was then stirred at the desired temperature for a specific time (2-12 h). After the completion, the reaction medium was centrifuged (Fanem centrifuge 206 BL) for 5 min at 3000 rpm to separate the solid catalyst from the liquid phase. Subsequently, an aliquot of the reaction medium was diluted in chloroform and transferred to the gas chromatograph (Varian GC-FID CP-3380) for the analysis. An external calibration curve was obtained by the injection of authentic samples of known concentrations, and used to quantify the reactant conversion and product formation. The thioanisole conversion was calculated by Equation 32:

$$\text{Conversion (\%)} = \frac{\text{moles of reactant reacted}}{\text{initial moles of reactant used}} \times 100 \quad (32)$$

whereas the selectivity of products was calculated according to the following expression (Equation 33):

$$\text{Selectivity (\%)} = \frac{\text{total moles of product formed}}{\text{the sum of total moles of all oxidation products formed}} \times 100 \quad (33)$$

## 3.3. RESULTS AND DISCUSSION

The thermal analysis of the $CuWO_4$, $NiWO_4$ and $ZnWO_4$ samples are presented in Figure 15. From the TG curves, a series of decomposition reactions related to mass loss can be noted, which can be attributed to different exothermic events, as indicated by the DSC curves. The thermal events, weight loss and corresponding temperature ranges inferred from the TG and DSC data are described in Table 3.

Figure 15- TG and DSC curves of (a) $CuWO_4$, (b) $NiWO_4$ and (c) $ZnWO_4$ precursor powders

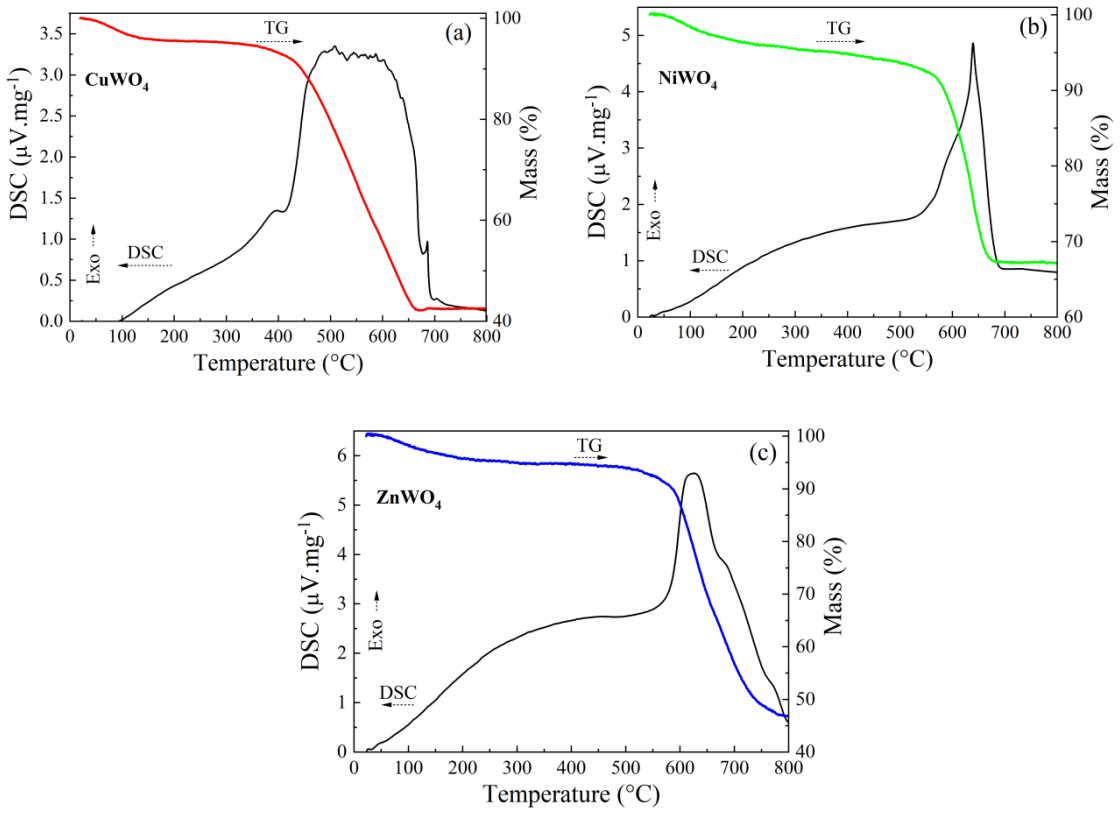


Source: author

Table 3- Thermal analysis results of $CuWO_4$, $NiWO_4$ and $ZnWO_4$ samples

| Sample | Temperature range according to TG data (°C) | Weight loss (%) according to TG data | Thermal event details |
|---|---|---|---|
| $CuWO_4$ | 43 – 112 | 5.0 | $H_2O$ and adsorbed gas elimination |
| $NiWO_4$ | 50 – 169 | 2.0 | |
| $ZnWO_4$ | 56 – 115 | 2.0 | |
| $CuWO_4$ | 112 – 394 | 7.0 | polymeric degradation ($-CH_2-$ groups) |
| $NiWO_4$ | 169 – 562 | 10 | |
| $ZnWO_4$ | 115 – 549 | 5.1 | |
| $CuWO_4$ | 439 – 664 | 51.0 | polymeric degradation (-CO- and -COO- groups) |
| $NiWO_4$ | 562 – 672 | 25.0 | |
| $ZnWO_4$ | 549 –737 | 45.0 | |

Source: author

XRD patterns of the $CuWO_4$, $NiWO_4$ and $ZnWO_4$ samples after annealing at 700 ºC for 2 h are shown in Figure 16, where it can be seen that all diffraction peaks are indexed in the monoclinic wolframite structure (P21/c space group for $NiWO_4$ and $ZnWO_4$ and $P\bar{1}$ space group for $CuWO_4$). The values obtained are congruent with those reported in the *Inorganic Crystal Structure Database* (ICDS) - cards numbers 73-1823, 15-0755 and 73-0554, respectively, indicating an absence of a second phase. From the Rietveld refinement results in Table 2, we can observe a good agreement between the experimental and calculated patterns. Unlike the cell lattice parameters reported in ICSD cards, we could not identify any significant changes in all samples. The Rietveld refinement analysis was also used to determine the occupancy factor for all powders. The occupancy factor value is related to defect density, which is attributed to O vacancies. Table 4 shows a lower occupancy factor, and consequently a higher number of oxygen vacancies for $CuWO_4$, followed by $NiWO_4$ and $ZnWO_4$.

Figure 16- XRD patterns of (a) $CuWO_4$, (b) $NiWO_4$ and (c) $ZnWO_4$ powders after annealing at 700 °C for 2 h

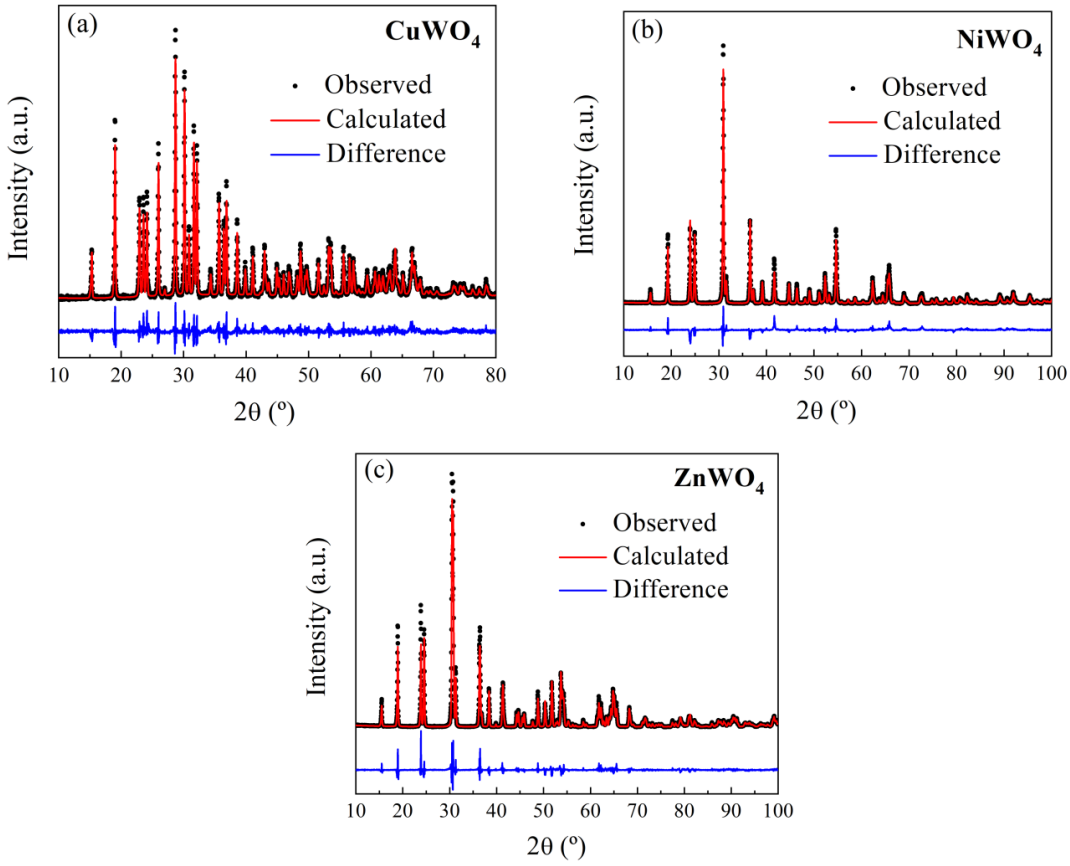


Source: author

Table 4- Lattice parameters (a, b, c), occupancy factor ($O_{occup}$), weighted profile R-factors ($R_{wp}$), goodness-of-fit factors ($\chi^2$) for $CuWO_4$, $NiWO_4$ and $ZnWO_4$ samples

| **Sample** | **Lattice Parameters (Å)** | | | **$O_{occup}$** | **Quality parameters** | |
|---|---|---|---|---|---|---|
| | **a** | **b** | **c** | | **$R_{wp}$** | **$\chi^2$** |
| $CuWO_4$ | 4.7083(1) | 5.8434(1) | 4.8823(1) | 0.975(12) | 0.0966 | 1.137 |
| $ZnWO_4$ | 4.6924(1) | 5.7208(1) | 4.9278(1) | 0.956(11) | 0.1294 | 1.106 |
| $NiWO_4$ | 4.6012(1) | 5.6678(1) | 4.9137(1) | 0.986(13) | 0.1358 | 1.317 |

Source: author

The surface areas of 1.0, 2.3 and 7.2 $m^2 g^{-1}$ were measured for Cu, Zn and Ni tungstates, respectively, after annealing at 700 $^oC$ for 2 h. It is possible to see the existence of type IV isotherms with H1 hysteresis loops, typical of mesoporous materials with a narrow pore size distribution. [91]

The SEM-FEG images of the $CuWO_4$, $NiWO_4$ and $ZnWO_4$ powders after annealing at 700 $^oC$ for 2 h are displayed in Figure 17. A strong particle coalescence forming agglomerates can be observed in all samples. It can be noticed that the particle size ($CuWO_4$ > $ZnWO_4$ > $NiWO_4$) is consistent with the surface area values ($CuWO_4$ < $ZnWO_4$ < $NiWO_4$).

Figure 17- SEM-FEG images of (a) $CuWO_4$, (b) $NiWO_4$ and (c) $ZnWO_4$ powders after annealing at 700 °C for 2h

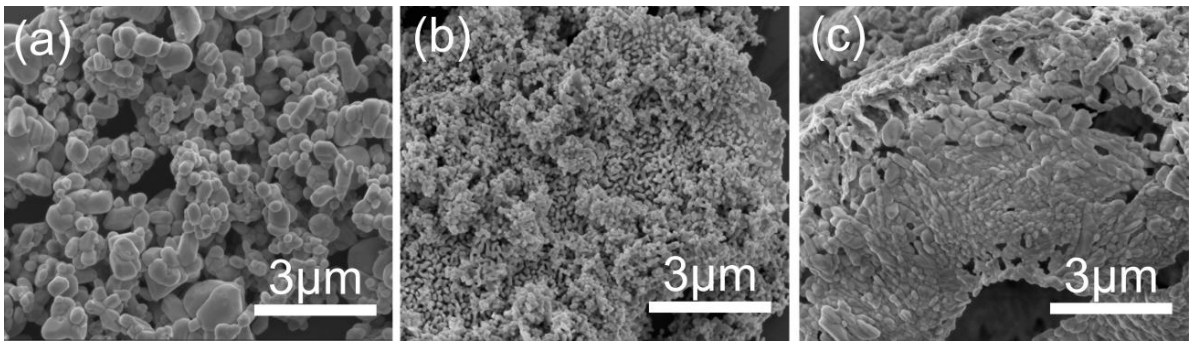


Source: author

In order to check the optical properties and band gap of the studied samples, UV-Visible absorption spectra were acquired. Figure 18a shows that the $CuWO_4$ and $NiWO_4$ powders are responsive in the visible region, while $ZnWO_4$ absorbs only in the ultraviolet region. The band gaps were obtained according to the following equation 34:

$$\alpha h\nu = B\,(h\nu - E_g)^n \quad (34)$$

where $\alpha$ is the absorption coefficient of the material, $h$ is the Plank's constant, $\nu$ is the radiation frequency, $B$ is a constant, $E_g$ is the band gap energy, and $n$ is a coefficient dependent on the type of transition considered (n = ½ for allowed direct transitions and n = 2 for allowed indirect transitions). [92] In Figure 18b, $(\alpha h\nu)^2$ or $(\alpha h\nu)^{1/2}$ was plotted against $h\nu$ to determine the direct and indirect band gaps, respectively. To obtain the band gap values, the linear part of the plot corresponding to the onset of strong absorption of the material was extrapolated. $CuWO_4$ crystals have an optical absorption governed by indirect transitions, [93] while the absorption of $NiWO_4$ and $ZnWO_4$ powders occur by direct electronic transitions. [94; 95] The results obtained for the $CuWO_4$, $NiWO_4$ and $ZnWO_4$ powders were 2.2, 2.5 and 3.2 eV, respectively, somewhat different from those found in the literature, which were 2.4 eV, [93] 2.2 eV [96] and 2.1 eV; [97] approximately 3.0 eV; [95; 98] and 3.9 to 4.4 eV, [94; 99] respectively.

Figure 18- (a) Reflectance and (b) optical band gap energy ($E_g$) calculated by the method proposed by Kubelka–Munk for any wavelength of $CuWO_4$, $NiWO_4$ and $ZnWO_4$ powders after annealing at 700 °C for 2h. On the axis $(\alpha h\nu)^m$ ($eV^m$), m = 2 and m = 1/2 for direct and indirect band gaps, respectively

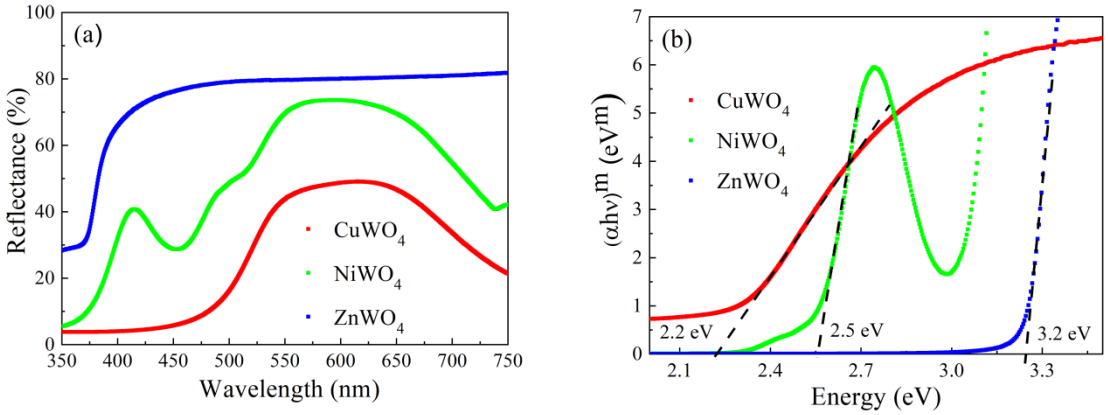


Source: author

In Figure 19, the PL spectra of $CuWO_4$, $NiWO_4$ and $ZnWO_4$ in the excited wavelength of 350.7 nm show the presence of a broad emission range typical of systems whose relaxation involves the participation of numerous states. [98] While the blue and green regions of the $CuWO_4$ samples indicate spectra with two maximum emission peaks centered at 445 nm and 532 nm,

respectively, the $NiWO_4$ PL spectrum is blue-green with spectral range peaking at 447 nm and 515 nm. The PL emissions are attributed to $WO_4^{-2}$ groups as a result of the recombination of electrons in the $^3T_{1u}$ state and holes in the $^1A_{1g}$ ground state. [100; 101] The $ZnWO_4$ PL emission centered at 637 nm (red region) is also blue-green, according to the literature, [102] however, the oxygen vacancies induce red-shift emission given the deep defects in the lattice. [99; 103]

Figure 19- PL spectra of (a) $CuWO_4$, (b) $NiWO_4$ and (c) $ZnWO_4$ powders after annealing at 700 °C for 2 h ($\lambda_{EXC}$ = 350.7 nm)

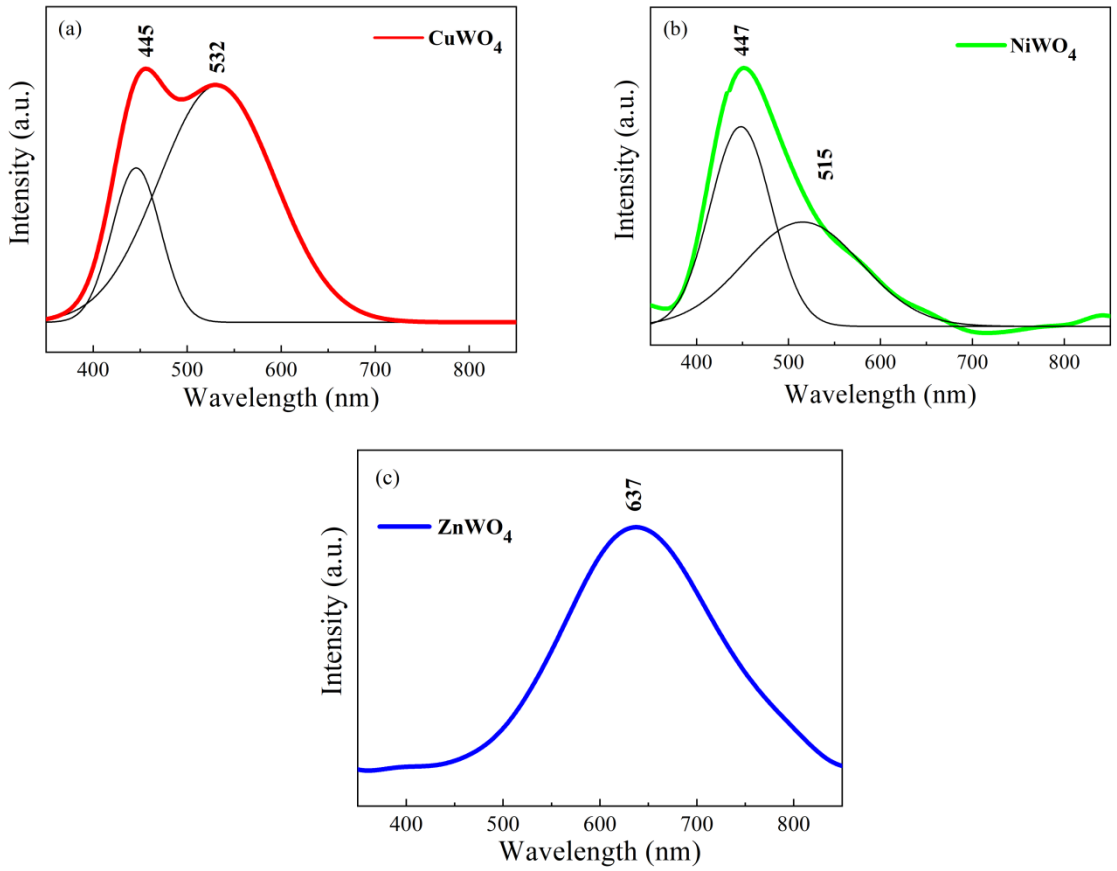


Source: author

From the $H_2$-TPR profiles obtained for the produced $MWO_4$ materials in Figure 20, it is possible to note the presence of more than one peak during the reduction processes to obtain tungstates, thus indicating multiple stages of reduction. For the $CuWO_4$ powder, the reduction begins at a lower temperature (~350 °C) than that for $NiWO_4$ (~500 °C) and $ZnWO_4$ (~700 °C), which concurs with the reduction potentials of the metals ($M^{2+}$ $2e^-$ →M), with E°red = +0.34, -0.25 and -0,76 V for M = Cu, Ni and Zn, respectively. The TPR profile for $CuWO_4$ shows a

first intense signal at 400-550 °C, a higher temperature than that for the typical CuO peak (200-350 °C). [104; 105] This is in accordance with the XRD results, suggesting that copper is present in the tungstate structure, and not in a secondary copper oxide phase. Similar results were observed for $NiWO_4$ and $ZnWO_4$. [106; 107; 108; 109]

Figure 20- (a) $H_2$-TPR profiles obtained for (b) $CuWO_4$, (c) $NiWO_4$ and (d) $ZnWO_4$ samples

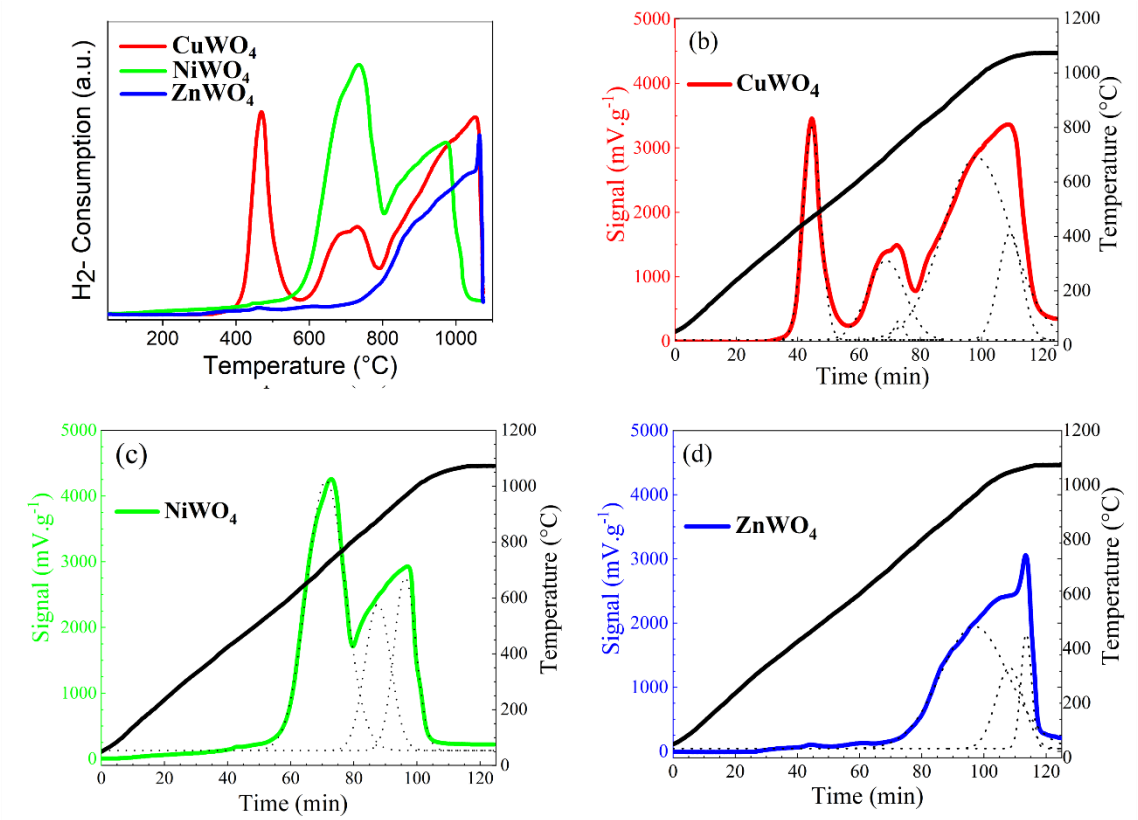


Source: author

Table 5 exhibits the adjusted peaks and hydrogen consumption for the three $MWO_4$ samples. The signals observed at temperatures higher than 700 °C for all catalysts can be associated with the reduction of $WO_3$ or $MWO_{4-x}$ phases formed after the initial reduction of copper or nickel catalyst. For $ZnWO_4$, it is evident the absence of a signal bellow 700 °C since $Zn^{2+}$ is reduced above this temperature. The $CuWO_4$ sample proved to have higher hydrogen consumption (and oxygen removal) than the $NiWO_4$ and $ZnWO_4$ powders (Table 5). This fact can be directly linked to the high reducibility of copper in comparison with nickel and zinc, suggesting that $CuWO_4$ would probably be more active in the oxidation reaction than the others (especially in comparison with $ZnWO_4$) due to its higher oxygen mobility.

Table 5- Results of $H_2$-TPR for $CuWO_4$, $NiWO_4$ and $ZnWO_4$ samples

| Sample | Peak | Temperature (°C) | Relative Area (%) | $H_2$ Consumption (x $10^{-3}$ mol $g^{-1}$) | |
|---|---|---|---|---|---|
| | 1 | 469.3 | 17 | 2.70 | |
| | 2 | 693.5 | 14 | 2.12 | |
| $CuWO_4$ | 3 | 737.6 | 1 | 0.13 | 15.5 |
| | 4 | 981.0 | 57 | 8.77 | |
| | 5 | 1055.5 | 11 | 1.78 | |
| | 1 | 717.8 | 58 | 7.08 | |
| $NiWO_4$ | 2 | 879.2 | 21 | 2.56 | 12.2 |
| | 3 | 964.6 | 21 | 2.57 | |
| | 1 | 960.6 | 71 | 5.87 | |
| $ZnWO_4$ | 2 | 1047.3 | 19 | 1.57 | 8.30 |
| | 3 | 1065.0 | 10 | 0.85 | |

Source: author

The prepared $MWO_4$ materials were used to promote the liquid phase oxidation of thioanisole in order to understand the effect of their textural properties on the sulfoxidation reaction. The catalytic thioanisole oxidation generates methyl phenyl sulfoxide and methyl phenyl sulfone as its oxidation products. For control, the homogeneous oxidation of thioanisole was performed using hydrogen peroxide and no catalyst. From this experiment, we could observe very low consumption (up to 12.1%) of thioanisole and the presence of methyl phenyl sulfoxide as the only product detected, demonstrating the importance of a catalyst in the reaction (Figure 21a). The $MWO_4$ powders were active catalysts, and the thioanisole conversion was affected by the nature of the catalyst (Figure 21b). $CuWO_4$ was the most active catalyst, accounting for 93.2% of conversion, followed by $NiWO_4$ (80.0%) and $ZnWO_4$ (68.9%), being the latter considered the least efficient.

The product selectivity was not significantly influenced by the nature of the catalysts (Figure 21b). Methyl phenyl sulfoxide was the major product formed after 12 h of reaction, with selectivity greater than 70.0% (Figure 21c). Comparing the BET results, it could be concluded that specific surface areas did not influence the catalytic activities in this work. The superior performance of $CuWO_4$ was associated with its higher reducibility and oxygen mobility (higher hydrogen consumption, according to $H_2$-TPR measurements). [29] The hydrogen consumption (Table 5) of $CuWO_4$ is almost twice as high as that of $ZnWO_4$ (the least active catalyst). Besides, the higher amount of oxygen vacancies observed in the $CuWO_4$ sample (Table 4) resulted in enhanced oxygen mobility.

The oxidation reactions of organic compounds involve two essential phenomena: bulk and surface oxygen mobilities. Higher oxygen mobility tends to cause the migration of active oxygen species through the catalyst structure, leading to an enhanced oxidation activity. [110] In addition, the intensity of $H_2O_2$ adsorption can be enhanced by oxygen vacancies on the catalyst surface, which can facilitate the generation of active oxygen species leading to an increase in catalytic activity. [111; 112] Because of the higher activity presented by the $CuWO_4$ catalyst, some tests were performed in order to understand the influence of some chosen reaction parameters (temperature, time and $H_2O_2$ volume) on the thioanisole conversion and product selectivity values. The results revealed an increase in the thioanisole conversion and in the selectivity towards the sulfone as a function of reaction time (Figure 21c). The thioaniole conversion increased dramatically as the reaction temperature increased (Figure 21d), which in turn is also responsible for altering the ratio of methyl phenyl sulfoxide to the methyl phenyl sulfone, highlighting the oxidation sequence of sulfide to sulfoxide, and then to sulfone. [70] Finally, the $H_2O_2$ volume was another factor that caused an enhancement in the thioanisole conversion efficiency, which reached 93.2% after 12 hours upon the addition of 1.0 mL of oxidant. When the $H_2O_2$ volume was increased up to 1.0 mL, the selectivity towards methyl phenyl sulfoxide dropped from 100% to 78.1%, with concomitant increase in the methyl phenyl sulfoxide formation (21.9%). Greater availability of the oxidant resulted in over-oxidation to the corresponding sulfone. [113]

Figure 21- Thioanisole conversion and selectivity of sulfoxide and sulfone (with and without catalyst) as a function of (a) $H_2O_2$ concentration (T = 50 °C, t = 12h); (b) different catalysts (0.1 mL of $H_2O_2$, T = 50 °C, t = 12h); (c) different times (0.1 mL of $H_2O_2$, T = 50 °C); and (d) different temperatures (0.1 mL of $H_2O_2$, t = 12h)

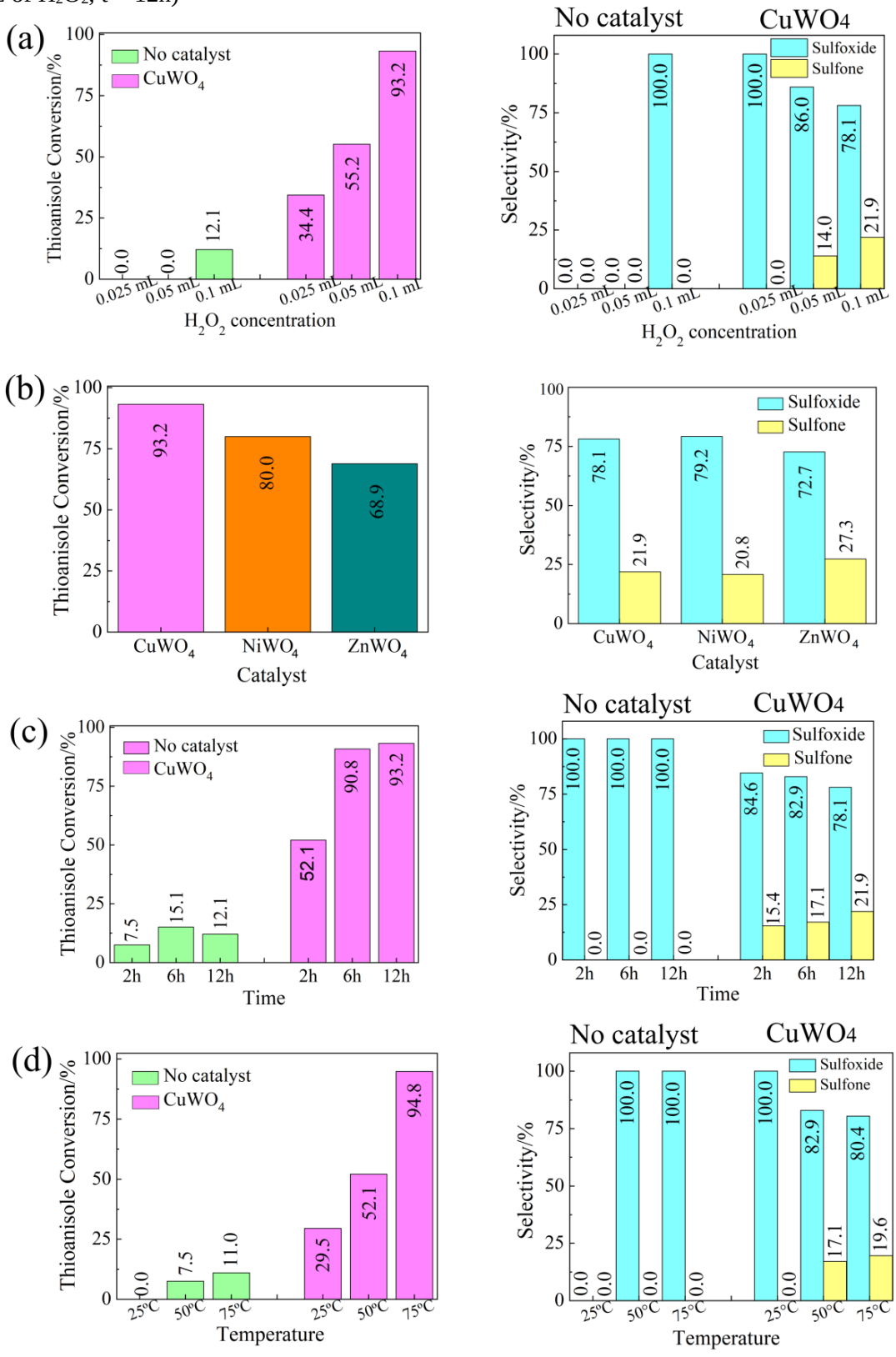


Source: author

## 3.4.CONCLUSIONS

In conclusion, we successfully and efficiently synthesized pure metal tungstates by the polymeric precursor method, which in comparison with other conventional methods is considered to be more efficient to save time and energy. The characterization results confirmed that a monoclinic wolframite structure can be obtained. The catalytic tests revealed that thioanisole could be oxidized by $H_2O_2$ to sulfoxides and sulfones at ambient conditions in the presence of the described metal tungstates. The product conversion and distribution changed according to the experimental parameters used, especially oxidant volume and catalyst nature. Analyses of the material indicated that a higher surface oxygen content and enhanced surface oxygen mobility were responsible for improving the reaction activity and selectivity.

**Acknowledgements**

The authors gratefully acknowledge the financial support from the Brazilian research funding agencies FAPESP (under grant number 2013/07296-2), CAPES, PROPP/UFOP and CNPq (under grant number 405033/2018-4).

**Note**

The authors declare no competing financial interest.

## 4. PAPER 2: INFLUENCE OF THE SYNTHESIS METHOD ON $CuWO_4$ NANOPARTICLES FOR PHOTOCATALYTIC APPLICATION

Naiara Arantes Lima [1], Gabryella Cerri Mendonça [1], Gelson Tiago Santos Tavares da Silva [2], Bruno Sanches de Lima [1], Elaine C. Paris [2] and Maria Inês Basso Bernardi [1]

[1] University of São Paulo, Physics Institute of São Carlos, São Carlos, SP, Brazil.

[2] Nanotechnology National Laboratory for Agriculture (LNNA), Embrapa Instrumentação, São Carlos, SP, Brazil.

Journal of Materials Science: Materials in Electronics - Received: 20 July, 2020; Accepted: 13 November, 2020. DOI: 10.1007/s10854-020-04887-2

Figure 22 - Graphical abstract of paper 2

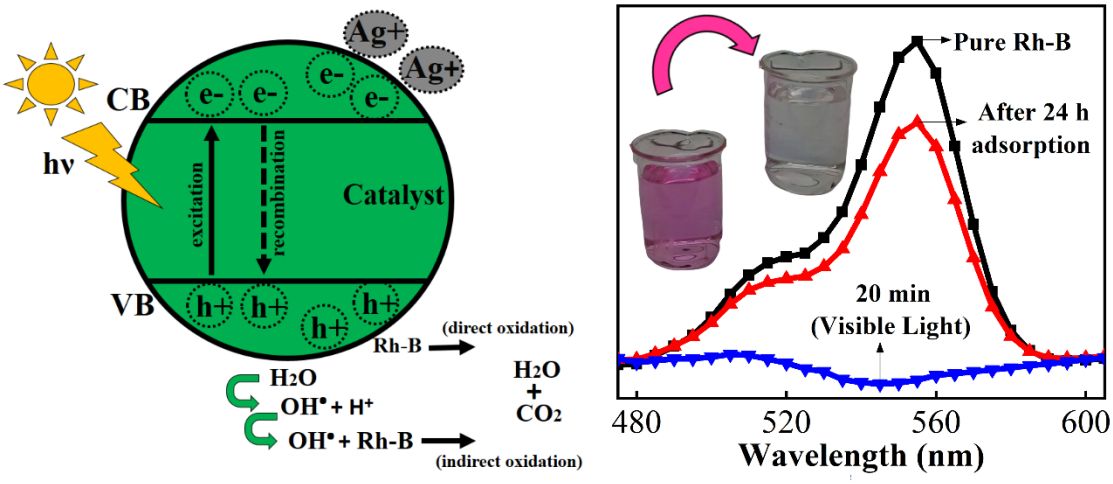


Source: author

ABSTRACT

The textile industry is responsible for most of the consumption and inappropriate disposal of organic and highly toxic pollutants, such as dyes. Therefore, it is necessary to remediate

polluting molecules before returning the water to the environment. Photocatalysis is a promising method for dye molecule degradation as it can provide complete mineralization through an efficient photocatalytic process. $CuWO_4$ exhibits a band gap of 2.40 eV and can be excited with visible light, making it economically advantageous for industrial-scale applications. In this work, $CuWO_4$ was synthesized by coprecipitation (CM), microwave-assisted hydrothermal (HM) and polymeric precursor (PPM) methods to evaluate the photocatalytic behavior in response to the different characteristics obtained from the synthesis routes. In photocatalytic measurements for OH• radical generation, the sacrificial agent $H_2O_2$ was used, and in order to delay the recombination process sodium oxalate and silver nitrate scavengers were applied under visible light. $CuWO_4$ synthesized by PPM was more efficient in the dye degradation when the $Ag^+$ scavenger was used, indicating that the predominant reaction mechanism was by direct oxidation or hydroxyl radicals. The surface charge (-38.5 (PPM), -29.7 (CM), and -16.2 mV (HM)) influence was more relevant than the specific surface area (1 (PPM), 22 (CM), and 21 $m^2$ $g^{-1}$ (HM)) of the samples in the photocatalytic process. The complete degradation occurred in 80 min for the samples obtained by CM and HM and only 20 minutes were necessary for the sample synthesized by PPM.

Keywords: Organic pollutants. Rhodamine B. Photocatalysis. Visible light. $CuWO_4$. Scavengers. Degradation.

## 4.1. INTRODUCTION

Currently, one of the biggest concerns in the world is the water quality of rivers, effluents, and the sea. In general, industries are believed to be mostly responsible for environmental pollution. Among them, the textile, paper, tannery, and food industries are a major threat to the water system, as their by-product is a large amount of water contaminated with numerous types of pollutants, including a segment of dyes called AZO, which is highly toxic and carcinogenic. [114; 115; 116] It is estimated that 70% of the industrial dyes are AZO-type (Tarkwa et al., 2019). Such dyes are widely used because of their high thermal and chemical stabilities, making them important dyeing products due to their capability of maintaining color for a long period. On the other hand, it is estimated that to produce 1 kg of dyed clothing, approximately 80 to 150 liters of dye-contaminated water are generated, being discarded in the wild without proper treatment. [117]

Among the most used AZO dyes by the industries is Rhodamine B, a reddish dye. Some dye removal techniques, such as adsorption, [118; 119] coagulation, [120] reverse osmosis, [121] and ultrafiltration, [122] have been used to treat effluents contaminated with this type of dye. However, these methods only separate the dye molecule from the water, making them unfeasible. In order to accelerate the process of degradation of the dye molecule, some free radicals with high oxidizing power must be generated. This process can occur through advanced oxidative processes (AOPs), for instance, $H_2O_2$, UV, UV / $H_2O_2$, $Fe^{2+}$ / $H_2O_2$, UV/$Fe^{2+}$/ $H_2O_2$. [123]

AOPs are based on the generation of highly oxidizing radicals, such as hydroxyl radical (OH•) and superoxide (O2-), which have a potential standard of reduction of E ° = 2.38 and -0.28 V, [124] being able to degrade organic molecules like AZO dyes. [118; 119; 120; 121] An effective method for generating free $OH^{\bullet}$ and $O_2^-$ radicals is heterogeneous photocatalysis, which occurs through a catalyst and adequate radiation. Semiconductors are considered the most common catalysts as they have a band gap with sufficiently low energy, being able to promote electrons from the valence band (VB) to the conduction band (CB) in the presence of ultraviolet or visible radiation. [123] If the photons have enough energy to promote electrons from VB to CB, the so-called electron-hole pair is generated. These gaps have positive potentials (between + 2.5 and + 3.5 eV) capable of forming the two necessary free radicals. The OH radical is generated when the VB hole interacts with water molecules adsorbed on the catalyst surface, and the $O_2^-$ radical arises when the CB electron interacts with dissolved oxygen. [125]

The $CuWO_4$ semiconductor is considered to be a promising catalyst as it presents a band gap with energies around 2.25 eV, being possible to be excited with radiation in the visible range of the electromagnetic spectrum. [41] The advantage of using visible radiation is that solar energy comprises more than 40% of this kind of radiation and only less than 5% of ultraviolet rays, making $CuWO_4$ an economically viable catalyst for application in several areas. [126]

For the photocatalysis to occur effectively, it is important that the recombination process is delayed as much as possible, allowing CB electrons and VB holes to be free in order to form radicals responsible for the degradation of organic molecules. One strategy to avoid recombination is the use of scavengers, such as $Ag^+$ and sodium oxalate, [127] since they are responsible for capturing electrons from the CB or donating electrons to the VB.

In the literature, it is possible to find studies using $CuWO_4$ as a catalyst for the degradation of organic dyes, such as methylene blue (MB), amido black (AB), orange G (OG)

[14] and Rhodamine B. [128] However, there are no studies comparing the efficiency of $CuWO_4$ using different methods of synthesis. Therefore, in search of a better understanding of its properties and in order to optimize the catalytic system, in this work we seek to evaluate the subtle differences obtained by three different methods of synthesis of $CuWO_4$ (coprecipitation (CM), microwave-assisted hydrothermal (HM) and polymeric precursor (PPM)). The objective is to study its structural properties to elucidate the mechanisms involved in the photocatalytic process for the total degradation Rhodamine B when using scavengers.

## 4.2. Experimental

### 4.2.1. Chemicals

All the chemicals used were of reagent-grade, and they were used without any further purification. Three different methods were used to prepare the $CuWO_4$: Coprecipitation (CM), Microwave-assisted Hydrothermal (HM), and Polymeric Precursors methods (PPM). [41; 129; 130] The materials used for the synthesis of $CuWO_4$ were copper(II) chloride dihydrate (Carlo Erba, 95%), sodium tungstate dihydrate (Sigma Aldrich, 99%), citric acid (Synth, 99,5%), ethylene glycol (Synth, 99%). The reagents used for the catalytic tests were rhodamine B (Sigma Aldrich, 95%), silver nitrate (Sigma Aldrich, 98%), hydrogen peroxide (Synth, 30%), sodium oxalate (Sigma Aldrich, 99%). All solutions were prepared using water purified by a Milli-Q system.

### 4.2.2. Coprecipitation method (CM)

This typical route was performed in two different steps. Firstly, equal molar amounts of copper (II) chloride dihydrate and sodium tungstate dihydrate (40 mmol) were dissolved in two different recipients with 250 mL of water each. The solutions were kept under stirring at room temperature until complete discoloration, and then mixed under the same conditions for 1 h. The final products were centrifuged, washed in water three times, and dried at 80 °C for 24 h in air. The powder was then grounded in an agate mortar and heat-treated in a conventional oven at 500 °C for 2 h at a heating rate of 10 °C $min^{-1}$. [129]

### 4.2.3. Microwave-assisted hydrothermal method (HM)

Similar to the route described above, the first step for obtaining the powder was the dissolution, in 80 mL of water, of equal molar amounts of copper(II) chloride dihydrate and sodium tungstate dihydrate (40 mmol) in two different recipients. After discoloration and mixing, 40 mL of sodium citrate (1.0 mmol) was added to the solution. The mixture was then kept under stirring at room temperature for 1 h. The resulting solution was microwaved at 160 °C for 1 h at a heating rate of 30 °C $min^{-1}$. The final products were centrifuged, washed with water three times, and then dried at 80 °C for 24 h in air. Afterwards, the powder was grounded in an agate mortar and heat-treated at 500 °C for 2 h at a heating rate of 10 °C $min^{-1}$. [41]

### 4.2.4. Polymeric precursor method (PPM)

The $CuWO_4$ nanoparticle synthesis procedure consisted of the dissolution of citric acid, tungstic acid and copper nitrate in water in three different containers, keeping a volume ratio of 3:1 of citric acid-metal precursors. After 1 h of stirring, the solutions were mixed, and a single solution was obtained. The pH of the solution was adjusted to 8 with sodium hydroxide heated to 120 °C, followed by the addition of ethylene glycol in a 2:3 molar ratio (citric acid: ethylene glycol). The resulting resin was pre-heated at 300 °C for 3 h at a heating rate of 10 °C $min^{-1}$ to obtain the precursor, from now on called puff. Finally, the heat treatment was performed at 500 °C for 2 h. [130]

### 4.2.5. Characterization

The structural characterization was made by X-ray diffraction (XDR) in the range of 20 to 50° and step of 0.02°, and scanned at 2° per minute using Cu kα radiation (λ = 1.5418 Å) on a Rigaku ULTIMA IV. For confirmation of the crystalline phase, the Raman spectroscopy

technique was performed using a Witec (Ulm, Germany) microscope equipped with a highly linear stage and objective lens from Nikon (100xNA=0.9). Raman signals of our samples were excited with an ion-Ar laser (514 nm; 10 mW) Melles Griot, and the Raman light was detected by high-sensitivity, back-illuminated Peltier-cooled CCD behind a 600 grooves/mm grating. The data were recorded in the wavenumber range from 130 to 1000 $cm^{-1}$. The morphology and particle size were determined by a scanning electron microscope (SEM-FEG) (Supra 35, Zeiss, Germany) operating at 3 kV. Image analysis was carried out with Image-J software. Specific surface area (SSA) analysis was made through the multimolecular adsorption theory (BET) using the Langmuir model. Nitrogen adsorption-desorption measurements were obtained by ASAP 2020 (Micrometrics, Brazil). Optical properties and photocatalytic activities were performed on a Cary 60 device by UV-Vis spectroscopy. X-ray photoelectron spectroscopy (XPS) measurements were carried out in a Scientia Omicron ESCA spectrometer with monochromatic Al Kα X-ray source (1486.7 eV, with power of 280 W and a constant pass energy mode of 50 eV). The XPS peaks were fitted using a Voigt function after subtracting a Shirley background and considering C-$sp^2$ binding energy of 248.8 eV. The zeta potential was analyzed in a Zetasizer (Malvern, Brazil) model Nano ZS.

### 4.2.6. Photocatalytic tests

The photocatalytic performance of the samples towards discoloration of Rhodamine B (RhB) in aqueous solution was evaluated in a quartz reactor and irradiated with a 150 W Hg lamp with maximum visible region wavelength emission. The photocatalytic experiments were carried out using 22 mg of the as-synthesized sample in a 40 mL solution with 1 mg $L^{-1}$ of RhB. The RhB discoloration was monitored by its absorption maximum at 554 nm at regular periods using a UV-Vis spectrophotometer in the absorbance mode. Before irradiation, the suspension was stirred for 24 h in the dark to establish an adsorption-desorption equilibrium.

### 4.2.7. Sacrificial agent and scavengers

0.1 mL of hydrogen peroxide ($H_2O_2$) was used as sacrificial agent, and 22 mg of sodium oxalate ($Na_2SO_4$) and 68 mg of silver nitrate ($AgNO_3$) were chosen as scavengers.

## 4.3. RESULTS AND DISCUSSION

The crystallographic pattern of the as-prepared $CuWO_4$ is shown in Figure 23. The peaks found were compared to the ICSD database. All samples exhibited a wolframite-type triclinic phase with P-1 spatial group and equal lattice parameters: a = 4.7026; b = 5.8389; c = 4.8784; A = 0.8054; C = 0.8355; α = 92.677; β = 92.469; and γ = 82.80. [131] The density of the material was 7.791 g $cm^{-3}$, which is in accordance with the crystallographic pattern No. 73-1823. [132] From the analyzed standards, the crystallographic profiles of $CuWO_4$ samples indicated that all synthesis methods (CM, HM, and PPM) used were efficient to obtain pure oxide phases without impurities.

Figure 23- XRD patterns of $CuWO_4$ powders synthesized by CM, HM and PPM after annealing at 500 °C for 2 h

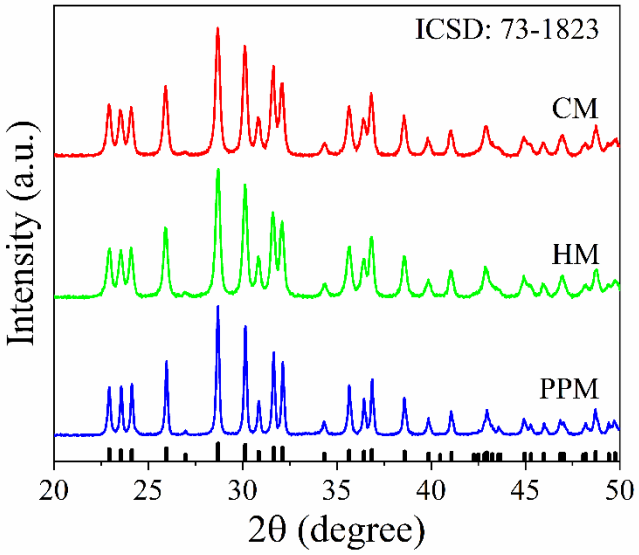


Source: author

Figure 24 shows the vibrational modes observed for $CuWO_4$ synthesized by CM, HM, and PPM. Theoretical studies indicated the existence of 36 vibrational modes for triclinic structures of the (P1) group and (Ci) group symmetry, which are divided into 18 vibrational modes corresponding to active Raman modes and another 18 corresponding to the infrared vibrational modes. [96] The Raman modes are attributed to the internal vibrational modes of $WO_6$ octahedron and external vibrational modes caused by the movement of the distorted

octahedrons of $CuO_6$ clusters. These Raman scattering data confirmed the displayed XRD results for all synthesized $CuWO_4$ samples, which revealed samples containing only the wolframite phase, regardless of the synthesis method used. [131]

Figure 24- Raman vibrational spectra of $CuWO_4$ powders synthesized by CM, HM and PPM after annealing at 500 °C for 2 h

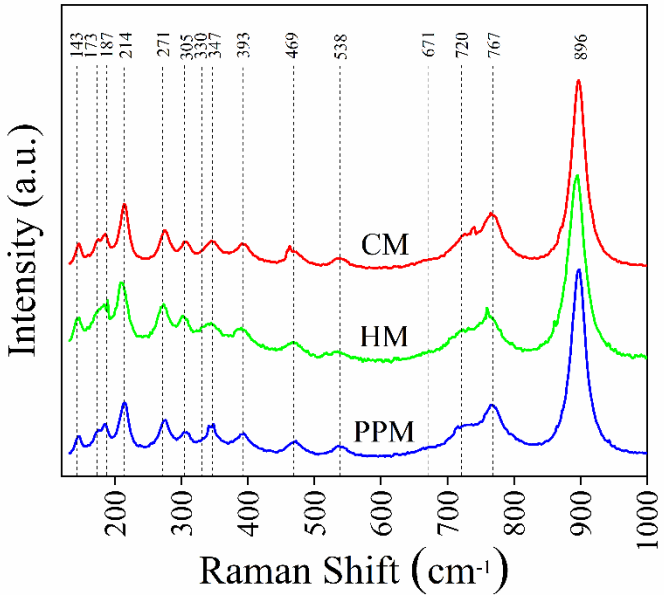


Source: author

Figures 25a-c shows the morphology and histograms of $CuWO_4$ samples synthesized by CM, HM, and PPM. The $CuWO_4$ synthesized by CM and HM showed spherical shape for both methods and similar nanoparticle size. On the other hand, the sample synthesized by PPM exhibited large and irregular-shaped particles. The narrower half-height width shown in the PPM diffractogram of Figure 23 is directly related to larger particle sizes, confirmed by the histogram of the particle size distribution in Figure 25c, [133] where it is possible to observe the difference between the particle size distributions according to the synthesis method. For instance, the mean values estimated for CM, HM and PPM methods were 42, 43 and 321 nm, respectively. The small particle size obtained by CM and HM can be attributed to the slow nucleation rate, while the particles obtained via PPM had faster nucleation and growth, which are inherent to the method itself.

Figure 25- Morphology and mean particle size of $CuWO_4$ powders synthesized by (a) CM, (b) HM and (c) PPM after annealing at 500 °C for 2 h

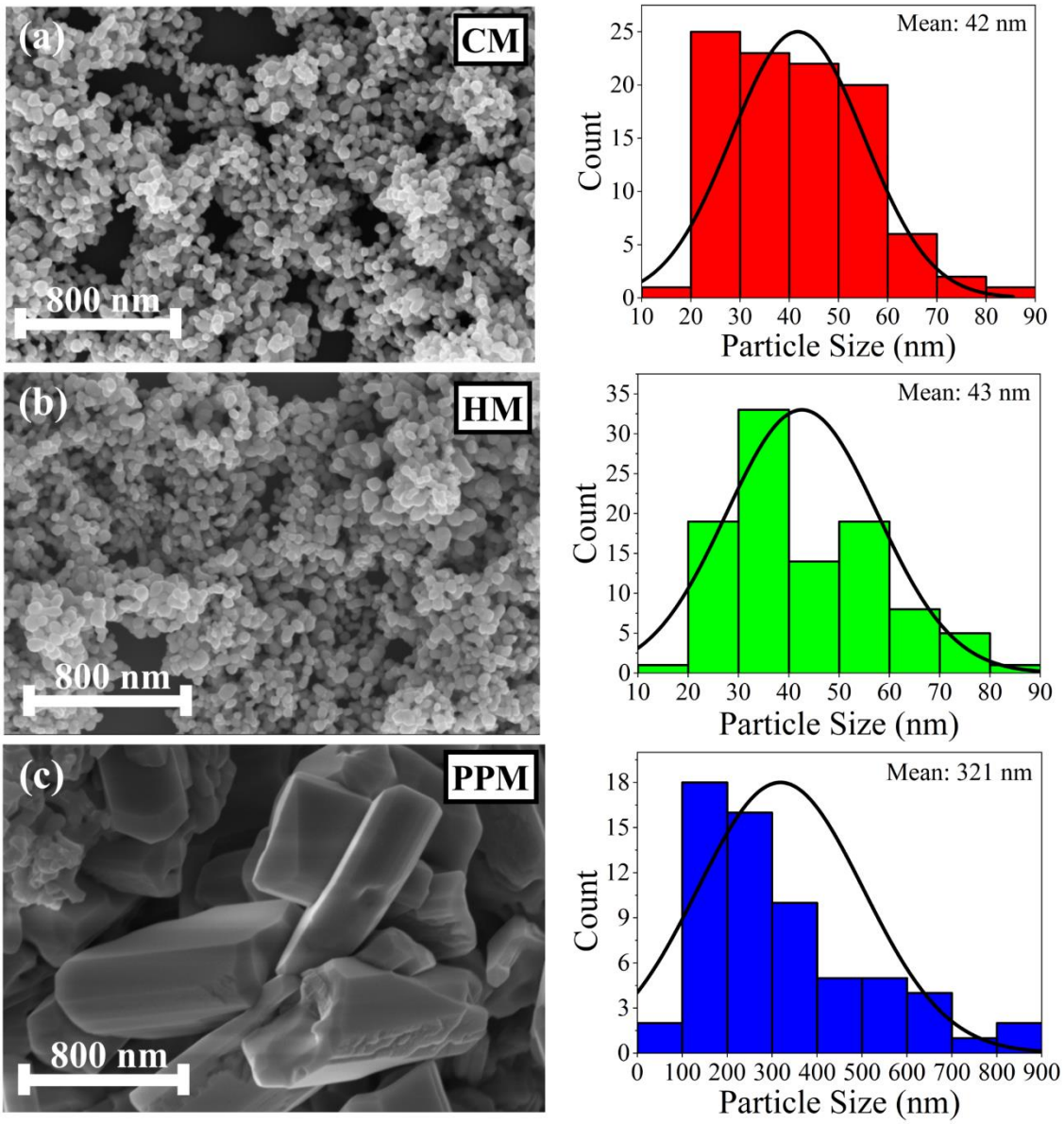


Source: author

The adsorption-desorption curves of nitrogen were found to be type III for the $CuWO_4$ obtained by all methods (CM, HM and PPM). From the BET results in Table 6, it is possible to observe that the samples synthesized by CM and HM exhibited similar surface areas (22 and 21 $m^2\ g^{-1}$) and pore sizes (9.8 and 9.5 nm), and equal pore volumes (0.0013 $cm^3\ g^{-1}$), while the catalyst obtained by PPM presented an area approximately 20 times smaller, half the volume of pores and smaller pores than the other samples.

Table 6- Langmuir surface area, pore volume and pore size results of $CuWO_4$

| Method | Langmuir Surface Area ($m^2\ g^{-1}$) | Pore Volume ($cm^3\ g^{-1}$) | Pore Size (nm) |
|---|---|---|---|
| CM | 22 | 0.0013 | 9.8 |
| HM | 21 | 0.0013 | 9.5 |
| PPM | 1 | 0.0007 | 6.9 |

Source: author

The band gap value of the $CuWO_4$ samples (CM, HM and PPM) were determined by UV-V spectroscopy shown in Figure 26. The extrapolated line intercedes the X-axis at 0 of the X axis and shows band gap values between 2.26 and 2.40 eV, indicating that all materials synthesized in this study can be activated under visible light, promoting low energy charge separation (< 3.0 eV). [129]

Figure 26- Band gap energy of $CuWO_4$ samples synthesized by HM, CM and PPM

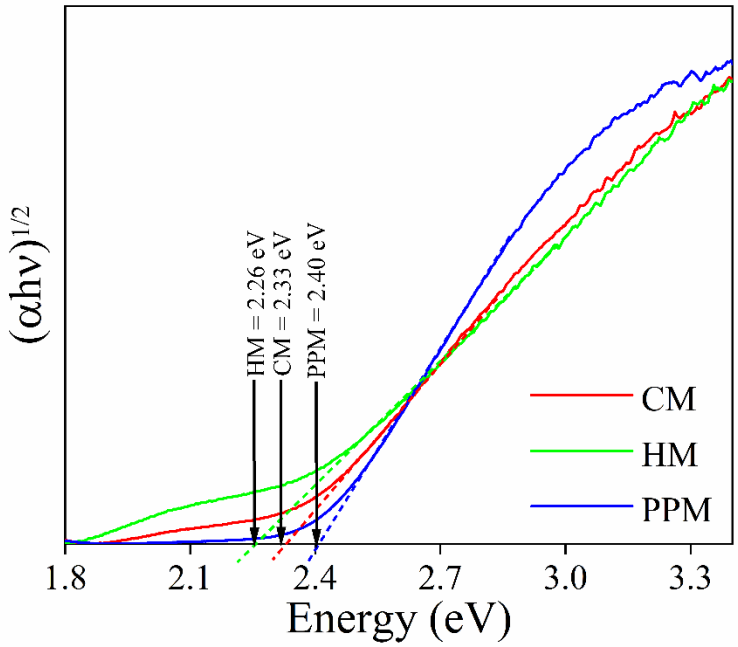


Source: author

X-ray photoelectron spectroscopy analysis was carried out to further characterize the chemical surface state of the resulting materials prepared by different methods. Figure 27a

presents the XPS survey spectra, where it is possible to observe peaks related to Cu, W, O and adventitious C, which are in agreement with the single-phase samples observed in the XRD results (Figure 23). In Figure 27b, the edge of the valence band was estimated at 1.9 eV by linearly extrapolating it to zero baselines. These values demonstrate the n-type nature of $CuWO_4$ and suggest that the Fermi level is located approximately at 0.4 eV below the conduction band, considering the optical band gap of 2.26 to 2.40 eV seen in Figure 26 for the samples synthesized by HM, CM and PPM. Figure 27c shows the O 1s high-resolution spectra of $CuWO_4$ prepared by the mentioned methods. The O 1s peak was deconvoluted into three components located at 530.5 eV, which can be attributed to structural oxygen ions ($O^{2-}$) bonded to $Cu^{2+}$ or $W^{6+}$, and at 531.9 eV, which can be associated with oxygen species such as peroxide ($O^{-}$) or hydroxide ions ($OH^{-}$) adsorbed on the material surface or oxygen vacancies in the crystal structure. [134] If we consider that the central component is a measure of point defects in the structure, it is possible to observe that the $CuWO_4$ prepared by CM exhibits the lowest number of defects, while the $CuWO_4$ obtained by PPM shows the highest number. The component at higher energies (533.3 eV) can be attributed to other species weakly adsorbed on the surface. Figure 27d presents a comparison between the W 4f high-resolution spectra of the samples prepared by the different methods. In Figure 27d, three peaks related to W 4f 7/2 (35.3 eV), W 4f 5/2 (37.5 eV) and to W 5p 3/2 (41.2 eV) can be noted. [135; 136] The core level of Cu 2p is shown in Figure 27e. The peaks in the vicinity of 934.3 eV and 954.1 eV are attributed to Cu 2p 3/2 and Cu 2p ½, respectively, whereas the peaks observed near 945 eV and 963 eV are satellite peaks commonly observed in $Cu^{2+}$ compounds. [137; 138]

Figure 27- High-resolution XPS spectra of $CuWO_4$ samples synthesized by HM, CM and PPM: (a) survey, (b) valence band, (c) O 1s, (d) W 4f and (e) Cu 2p regions

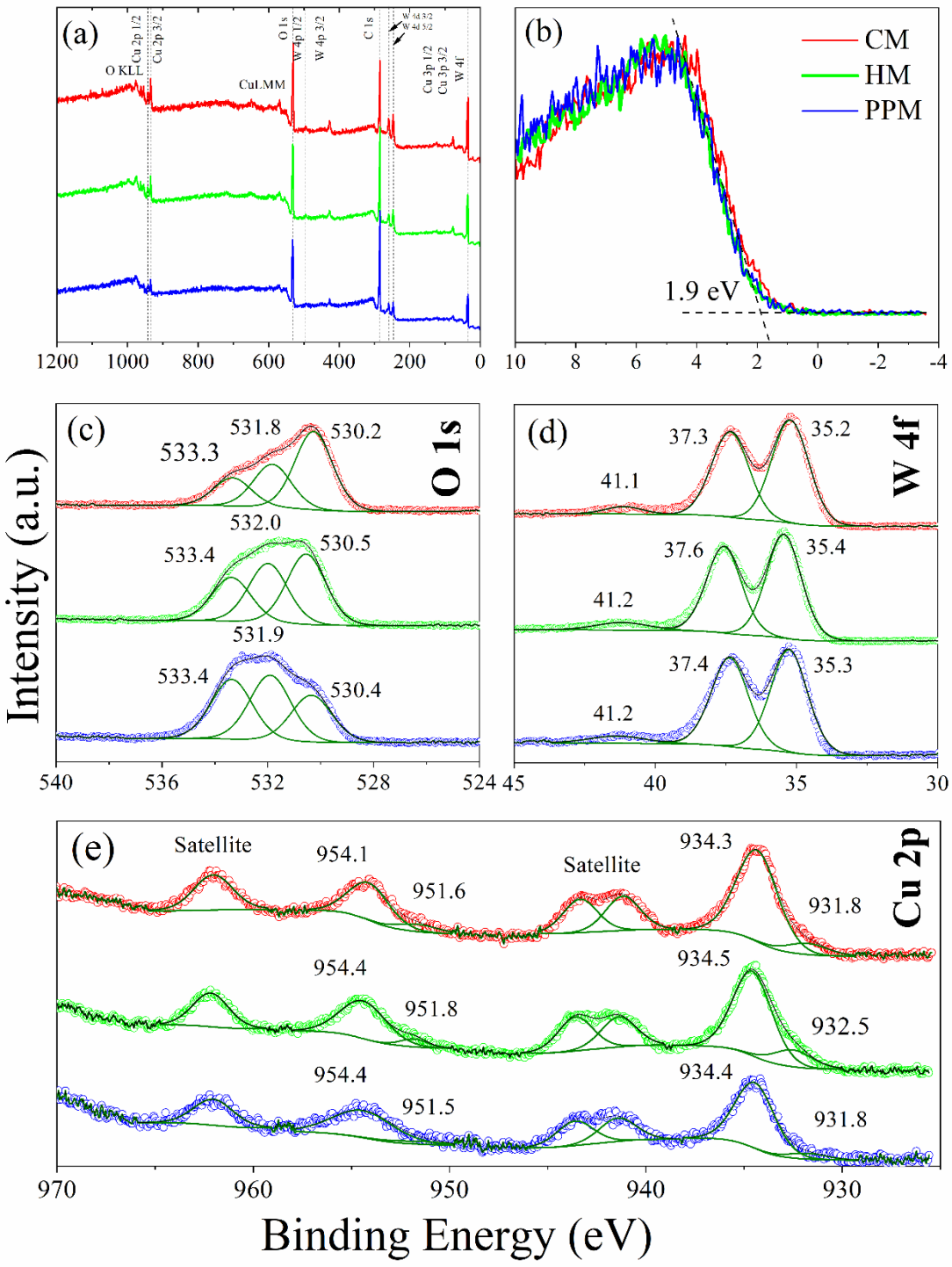


Source: author

DLS and zeta potential measurements were performed in triplicate at pure deionized water pH. The obtained values and standard deviation are displayed in Figures 28a-d. The nanoparticles exhibited different average hydrodynamic diameters and stability behavior in

suspension under this pH range condition (5.9-6.5), indicating a decrease of dispersibility for MPP, MC and MH syntheses. $CuWO_4$ particles obtained by CM with a medium particle diameter of 42 nm (Figure 25) showed a mean particle size distribution of 163 nm (Figure 28a). Comparing this sample (Figure 28b) to that synthetized by the HM method, it is possible to note that the latter exhibited particles with medium diameter of 43 nm (Figure 28b), cluster average size of 305 nm, wide distribution range and great heterogeneity. For the catalyst obtained by the PPM method, the medium DLS diameter was approximately 750 nm (Figure 28c) as a result of the largest particle size (321 nm) obtained by this route. However, such sample presented the narrowest distribution range when compared to the other synthesis methods. This difference in the size distribution of nanoparticle agglomerates is due to the surface charge difference of $CuWO_4$ obtained by the CM, HM and PPM methods, which was -29.7, -16.2 and 38.5 mV (Figure 28d), respectively. The highest modulus value of the zeta potential and best particle dispersion were found for CM and PPM. The different values found for the zeta value of the particles may be attributed to the different synthesis conditions, the choice and concentration of precursors and mineralizers, and the presence of actives, such as sodium citrate (HM), citric acid and ethylene glycol (PPM), required in the synthesis steps to obtain $CuWO_4$ in each synthetic route. Some studies have reported negative values between -10 and - 40 mV of other tungstate-based materials, such as $CoWO_4$, [139] $ZnWO_4$ [140] and $SnWO_4$, [141] which represents a similar behavior to that reported in this paper. Dutta et al. [128] synthesized $CuWO_4$ nanoparticles sized 36.6 ± 12.2 nm by the sonification method. In the zeta potential analysis, a surface load of -15.47 mV and -15.67 mV was observed at pH 5 and 7, respectively. Thus, the three synthesis routes used in the present work proved to be efficient to obtain negatively charged $CuWO_4$ nanoparticles and expected stability for tungsten-based materials. More specifically, the coprecipitation method enabled the synthesis of particles with nanoparticle dimensions similar to those found in the literature and higher stability in medium suspension under the same pH conditions.

Figure 28- Histogram of the DLS results for $CuWO_4$ nanoparticles obtained by (a) coprecipitation, (b) hydrothermal and (c) polymeric precursor methods, and (d) potential zeta and pH values

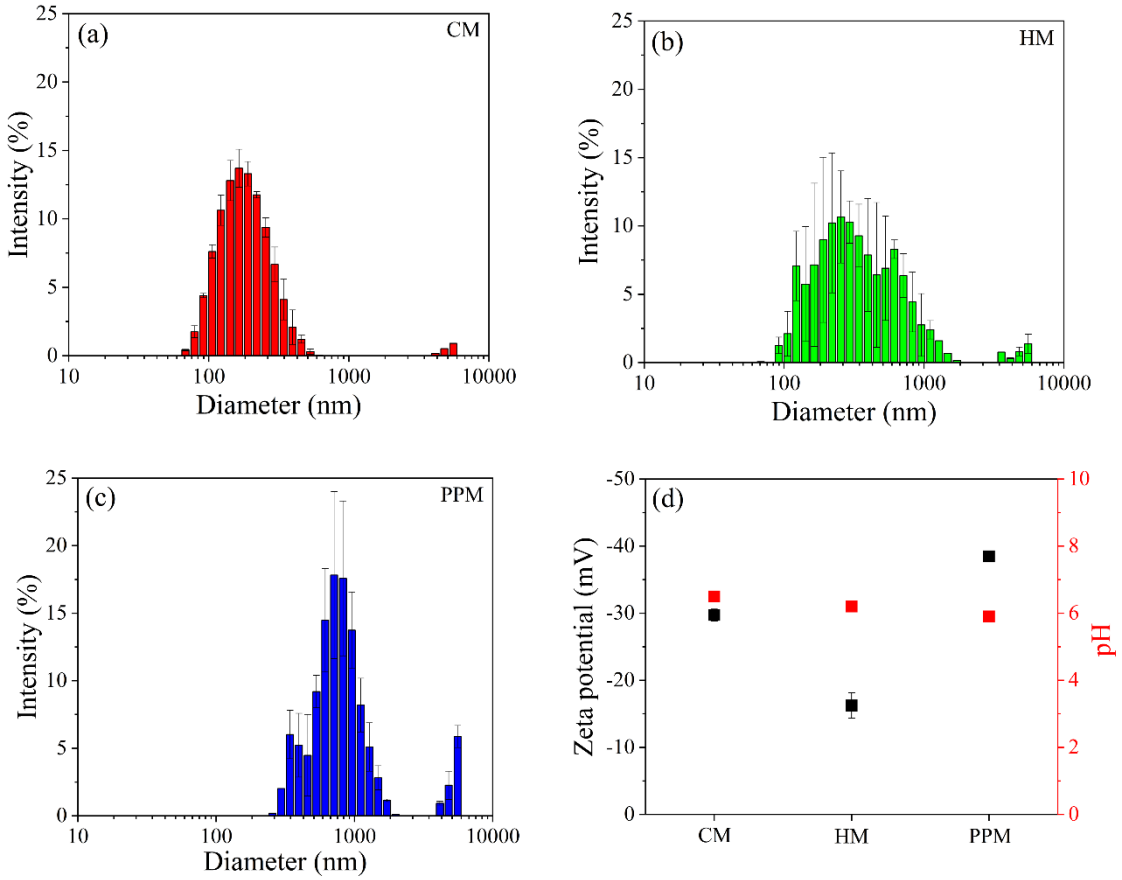


Source: author

The RhB dye was used as probing molecules to explore the discoloration property of the as-prepared samples. The synthesized semiconductors promoted the discoloration in two effects, as it can be seen in Figures 29a-d. The first effect was induced by adsorption, which was evident after a few hours of contact between the synthesized materials and the dye due to the physical interaction between them. After the equilibrium period (24 h), it was observed that all analyzed samples reached a similar percentage of discoloration (around 25%), indicating that both the specific surface areas and the surface charges directly influenced this process. The combination of these two properties can be observed in the PPM sample. Despite the low specific surface area (1 $m^2$ $g^{-1}$) of this sample, such property was compensated by the surface load (-39 mV), which may have favored the interaction with the positive charges for RhB. The second effect associated with the discoloration of Rhodamine B was attributed to the photoactivation of the synthesized materials, as also seen in Figures 29a-d.

This effect is due to the semiconductor activation by energy equal to or greater than its band gap value. When this occurs, the valence band electrons are promoted to the conduction band, thereby forming oxidizing and reducing species in the valence and conduction bands, respectively (Equations 35-38). However, although the prepared samples exhibited a band gap that allowed them to be activated under visible radiation, their photocatalytic activity was relatively low, degrading only 20, 7 and 1% after 80 min for CM, HM and PPM samples, respectively (Figure 29a).

This higher photocatalytic activity exhibited by the sample obtained by CM can be attributed to its smaller particle size, higher specific surface area, and opposing charge surface. In contrast, even with low performance, this combination allowed a more significant interaction between the dye and the catalyst compared to the other methods.

The photocatalytic performance of copper tungstate has been extensively investigated in recent years as it is a potential candidate for the degradation of organic pollutants in reactions driven by visible radiation. [14; 142] However, its low activity is still a challenge. Among the alternatives found, the use of sacrificial agents can be considered promising. As it can be seen in Figure 29a, the synthesized samples showed low photocatalytic activity after 80 min of exposure to visible radiation. The addition of sodium oxalate, a hole scavenger, induced quenching of the photocatalytic performance for all synthesized samples during the photocatalytic tests, demonstrating that direct process oxidation (Equations 35 and 36) represents one of the main pathways for the RhB discoloration using $CuWO_4$ synthesized by different methods. Additionally, the photogenerated hole in the semiconductor valence band oxidized oxalate, generating carbon dioxide and neglecting dye degradation, as shown in Equations 39 and 40. On the other hand, with the addition of silver nitrate or peroxide hydrogen it is possible to observe a sharp increase in RhB discoloration promoted by the synthesized catalysts, since both sacrificial agents favored the formation/performance of radical species with high oxidative capacity, such as valence band holes ($h^+$) and hydroxyl radicals ($OH^{\bullet}$). The addition of silver nitrate during the tests for RhB photodegradation conducted by the synthesized catalysts promoted significant dye discoloration in a few minutes of experiment. After 20 min of exposure to visible light, the catalysts obtained by CM and HM induced approximately 80% of RhB discoloration. However, after the same exposure period, the PPM sample degraded 100% of the organic molecule. This process may be associated with the negative charges present in large quantities on the surface of this sample compared to the other synthesis methods. Besides, there may have been a more significant interaction between the

silver present in the solution and this catalyst since silver is responsible for inducing an increase in the lifetime of the photogenerated $e^-/h^+$ pairs in the semiconductor sequestering the electrons generated in the conduction band of the semiconductor. This way, the photogenerated hole, one of the main oxidizing agents of synthesis materials, is available for interaction with water for a longer period, generating more hydroxyl radicals and the direct oxidation of the organic molecule (Equation 37). When evaluating the RhB photodegradation experiments using catalysts synthesized with the addition of hydrogen peroxide, a considerable increase in the photocatalytic activity of the oxide could also be observed. This can be explained by the fact that, when irradiated with sufficient energy to promote the formation of $e^-/h^+$ charge pairs, the hole directly oxidizes hydrogen peroxide, generating hydroxyl radicals (Equations 41 and 42), or the hole oxidizes water, generating hydroxyl radicals that react with peroxide, doubling its presence in the solution and leading to a complete dye discoloration after 80 min for all samples.

Figure 29- Adsorption and photocatalytic effect of $CuWO_4$ catalysts synthesized by CM, HM and PPM on the degradation of Rhodamine B

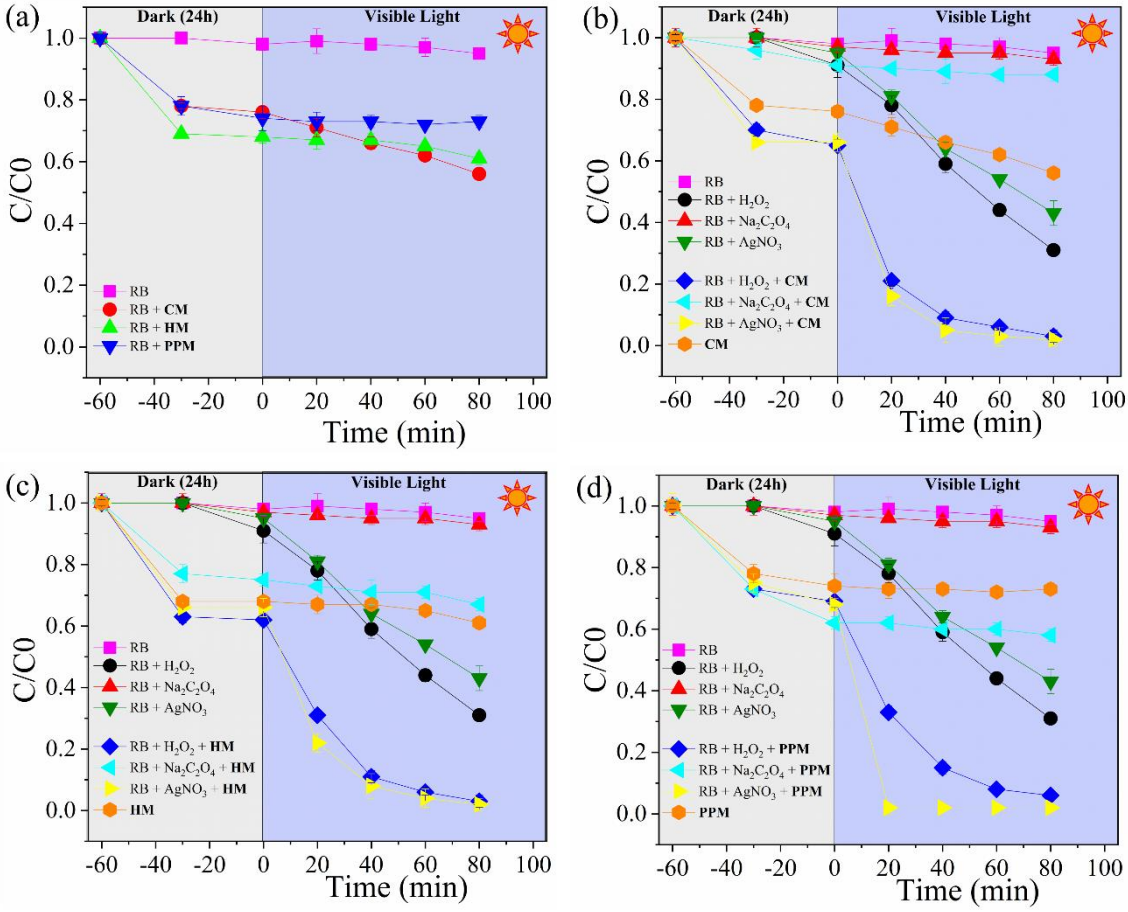


Source: author

$$CuWO_4 + h\nu \rightarrow h^+_{VB} + e^-_{CB} \quad (35)$$

$$h^+_{VB} + RhB_{(ads)} \rightarrow CO_2 + H_2O \quad (36)$$

(direct oxidation)

$$h^+_{VB} + H_2O_{(ads)} \rightarrow OH^\bullet + H^+ \quad (37)$$

$$OH^\bullet + RhB_{(ads)} \rightarrow CO_2 + H_2O \quad (38)$$

(indirect oxidation)

$$C_2O_4^{2-} + h^+_{CB} \rightarrow C_2O^-_{4(ads)} \quad (39)$$

$$OH^\bullet_{(ads)} + C_2O_4^- \rightarrow HCO^-_{3(ads)} + CO_{2(ads)} \quad (40)$$

$$h^+_{CB} + H_2O_2 \rightarrow 2OH^\bullet \quad (41)$$

$$OH^\bullet + H_2O_2 \rightarrow H_2O + 2OH^\bullet \quad (42)$$

## 4.4. CONCLUSION

We observed that of all possible variables involved in the RhB photodegradation process, the most important was surface load (-38.5 for PPM, -29.7 for CM, and -16.2 for HM). From the XPS results, we could note that the only difference was in the oxygen amount, which indicates that the different synthesis procedures yield materials with different density of defects in the crystal structure, such as oxygen vacancies (CM < HM < PPM). Furthermore, the surface area was relevant only when the catalyst was used in the dark and induced by adsorption, which was evident after a few hours of contact between the synthesized materials and the dye due to

the physical interaction between them After the equilibrium period (24 h), we observed that all analyzed samples reached a similar percentage of discoloration (around 25%). (CM = HM ≠ PPM). Finally, the scavenger $Ag^{+}$ captured electrons from the conduction band, preventing the recombination of the electron-hole pair and optimizing the degradation process of Rhodamine B, thus favoring direct and indirect oxidation.

**Funding:** The authors gratefully acknowledge Dr. Renato Vitalino Gonçalves and the financial support from the Brazilian research funding agencies, namely, FAPESP (under grant number 2013/07296-2), CAPES, PROPP/UFOP and CNPq (under grant numbers 405033/2018-4 and 159866/2018-9).

**Conflict of Interest:** The authors declare that they have no conflict of interest.

## 5. PAPER 3*:* $NiWO_4$ POWDERS PREPARED VIA POLYMERIC PRECURSOR METHOD FOR APPLICATION AS CERAMIC LUMINESCENT PIGMENTS

Naiara Arantes Lima [1], Lorena Dariane da Silva Alencar [2], Maximo Siu Li [1], Carlos Alberto Carneiro Feitosa [3], Alexandre Mesquita [4], Jean Claude M'Peko [1], Maria Inês Basso Bernardi [1]

[1] Instituto de Física de São Carlos, Universidade de São Paulo, 13560-970 São Carlos, SP, Brazil

[2] Instituto Federal de Mato Grosso do Sul, IFMS, 79200-000 Aquidauana, MS, Brazil

[3] Departamento de Física, Centro de Ciências Exatas e Tecnologia, Universidade Federal do Maranhão, UFMA, 65080-805, São Luis, MA, Brazil

[4] Instituto de Geociências e Ciências Exatas, Universidade Estadual Paulista, Departamento de Física, 13506-900, Rio Claro, SP, Brazil

Journal of Advanced Ceramics - Received: 24 March, 2019; Accepted: 13 August, 2019. DOI: 10.1007 / s40145-019-0347-z

### ABSTRACT

$NiWO_4$ was prepared using the polymeric precursor method and studied in terms of physical and chemical properties to verify its stability for industrial applications as pigments. The characterization was accomplished using thermal analyses, X-ray diffraction (XRD), scanning electronic microscopy (SEM), photoluminescence (PL) and UV–Vis spectroscopies, colorimetric coordinates, and Raman spectra. Increasing temperature, successive exothermic reactions were observed and they are related with thermal decomposition of the organic compound. The stability was reached at ~700 °C. The material is verified to become completely free of second phase at ~800 °C. The end $NiWO_4$ powder showed an intense charge transfer-related tail centered in the ultraviolet region, resulting in a yellow product. In addition, this powder exhibited broad excitation band and broad deep blue–green emission band, which were enhanced with increasing powder's crystallinity.

Keywords: Nickel tungstate. Yellow pigment. Colorimetric coordinate. Optical property. Structural characterization.

## 5.1. INTRODUCTION

Organic and inorganic materials have been largely used as yellow pigments, such as gamboge which is a pigment derived from a tree, the $Fe_2O_3 \cdot H_2O$, which is found in clays, lead antimonate, zinc chromate, CdS, $PbCrO_4$, $NiOSb_2O_5 \cdot 20TiO_2$ and $As_2S_3$. However, these pigments have some characteristics that make them not ideal for use, such as toxicity, chemical, and thermal instability.

Due to the superior acid–alkaline, chemical and thermal stability, and coverage power of these materials, [143] inorganic pigments are known to present several applications in the manufacture of porcelains, ceramic tiles, enamels, paints, rubber, imitation leather, varnishes, building materials, glass, glazes, and floor covering. However, many inorganic pigments with brilliant color and good functionality are contaminating products to be avoided because of their negative effect on environment and human health. With regard to yellow inorganic pigments, chromates of alkaline-earth metal ions (e.g., calcium, strontium, and barium), Naples yellow (lead antimonite), litharge (lead oxide) and yellow cadmium (cadmium sulfide) were for long time of particular importance due to their specific coloration, which was the reason of their wide use in ceramic tiles. [143] However, the use of these pigments is restricted in terms of commercial applications because of the toxicity of Cr, Cd, Sb and Pb atoms. [144; 145; 146; 147] Consequently, development of sustainable and environmentally friendly inorganic pigments and/or reducing the toxicity of existing inorganic pigments are two approaches strongly required.

Tungstates of formula $AWO_4$ ($A = Ni^{2+}$, $Ca^{2+}$, $Sr^{2+}$, $Ba^{2+}$) belong to an important family of functional inorganic materials [148; 149] that have attracted great attention in the industry because of their interesting physical and chemical properties, [150; 151] mainly because they are not toxic. The divalent cations are called network modifiers and the tungsten atoms are called network formers. They can form two distinct structures depending on the ionic radius or cations. When the radius is greater than or equal to 0.99 angstroms, it allows the formation of the Scheelite structure ($Ca^{2+}$, $Sr^{2+}$, $Ba^{2+}$) and for radius smaller than 0.77 angstroms, the Wolframite structure is formed, which is the case of $NiWO_4$ 12]. [152; 153; 154] From a technological viewpoint, the versatility of these materials in terms of possible applications includes: light emitting diodes

(LEDs), [150] electrodes, [154] cathode material for supercapacitors, [155] photoluminescent materials, [64] and photocatalyst. [156; 157] In particular, nickel tungstate, the material targeted in this work, is one of the potential candidates to be used as yellow inorganic luminescent pigment. [158]

Luminescent materials have the characteristic of emitting light when stimulated by chemicals and ionizing radiation. The luminescent pigments have several applications, among them, they are used in plates and transit lanes, markings on money notes to make it difficult to fade, in fabrics and wall paintings for decoration. [64] It should be pointed out that scientific and technological interest on these materials also arises because of dealing with low-cost and no polluting materials, that can be included in the group of sustainable products.

The chemical and physical properties of metal oxides, including tungsten oxides, depend on the synthetic route employed. There are two ways of synthesizing ceramic pigments: by chemical method such as co-precipitation, [101; 129; 159] hydrothermal, [160; 161; 162] and polymeric precursor method [163] or by solid state reaction method. Among them, chemical methods, particularly the polymeric precursor method, show several advantages, such as homogeneous mixture of the reactants, purity, low cost, simple synthesis, temperatures below 800 °C, and short time processing. [164]

Therefore, the present work involved the synthesis of $NiWO_4$ nanoparticles achieved by applying the polymeric precursor method, which is a low-cost processing procedure, when compared to other chemical methods, besides ensuring high material reproducibility. The method has been successfully used in the synthesis of nanoparticles of different oxides, [165] and is based on the chelation of cations by a hydrocarboxylic acid (normally citric acid), followed by polyesterification using a glycol (normally ethylene glycol). [166] The formed precursor resins contain cations randomly distributed throughout the polymer. [167; 168; 169] The synthesized nickel tungstate powder was subsequently characterized by thermal analyses: thermogravimetric (TG), differential scanning calorimetry (DSC), X-ray diffraction (XRD), diffuse reflectance, colorimetric coordinate, scanning electron microscope (SEM), Raman and photoluminescence (PL) spectroscopies.

## 5.2. EXPERIMENTAL

The processing of materials involved the dissolution of nickel nitrate in milli-Q water and the dissolution of tungstic acid in milli-Q water at 90 °C with a pH of 11. For the pH of tungstic acid solution reaches the value of 11, it is necessary to add ammonium hydroxide. On the other hand, citric acid was dissolved in milli-Q water. Both intermediary products were

mixed so as to produce a tungsten citrate solution. The polymeric resin was synthesized by adding nickel nitrate to this solution, under constant stirring, and at a temperature of 120 ℃. Addition of ethylene glycol promoted the polyesterification reaction. The citric acid:metal molar ratio was 3:1, while the citric acid:ethylene glycol mass ratio was 2:3.

The polymeric precursor solution was heat-treated at 400 ℃ for 4 h at a heating rate of 10 ℃·min$^{-1}$. The obtained powder was grounded in an agate mortar in order to deagglomerate the powder, hereafter called the precursor powder which was treated at temperatures of 500–800 ℃ for 2 h, with a heating rate of 10 ℃·min$^{-1}$.

The material was characterized by thermal decomposition, XRD, UV–Vis spectroscopy, colorimetric coordinates, SEM, and Raman and PL spectroscopies. The thermal decomposition and crystallization of this powder were studied by TG (Netzsch STA 409C) and DSC techniques under oxygen atmosphere at a heating rate of 10 ℃·min$^{-1}$. $Al_2O_3$ was used as reference material during the thermal analyses. Based on the results from the thermal analyses, as later presented, we considered heat-treating the precursor powder at 500–800 ℃ for 2 h to get a close insight into phase development. These heat treatments were performed in an electric furnace under air atmosphere, at a heating rate of 10 ℃·min$^{-1}$.

In the following, the samples were characterized by XRD at room temperature, towards the 2θ ranged from 20 º to 80º, with a step of 0.020º, a scanning speed of 2 (º)· min$^{-1}$, and using Cu Kα radiation (Rigaku, ULTIMA IV).

The samples were also subjected to UV–VIS characterization (Shimadzu-UV-1601 PC spectrophotometer), and the spectra were measured in the range of 220–900 nm.

Colorimetric coordinates of the pigments were measured in the range of 300–700 nm, using a spectrophotometer (Minolta, CM2600d) equipped with a standard type D65 (day light) light source, and following the CIE-L*a*b* colorimetric method recommended by the Commission Internationale de l'Eclairage (CIE). [170] In this method, $L^*$ is the lightness axis [black (0) → white (100)], $b^*$ is the blue (-) → yellow (+) axis, and $a^*$ is the green (-) → red (+) axis, while $\Delta E$ is defined as the total color difference ($\Delta E^2 = L^{*2} + a^{*2} + b^{*2}$).

Microstructural characterization of the powders was carried out using a high resolution SEM (FEG-SEM Supra 35, Zeiss, Germany) operating at 3 kV.

Raman spectra were measured with a MonoVista CRS Raman spectrometer from Spectroscopy and Imaging GmbH. The samples were irradiated with a laser beam focused with an Olympus microscope. For the excitation in backscattering geometry, the 633 nm line of a He-Ne laser with 35 mW was used. Photoluminescence spectra were collected with a Thermal Jarrel-Ash Monospec monochromator and a Hamamatsu R955 photomultiplier. The 350.7 nm

exciting wavelength of a krypton ion laser (Coherent Innova 200) was used; the output of the laser was maintained at 500 mW, with ~14 mW.

## 5.3. RESULTS AND DISCUSSION

### 5.3.1. Thermal analysis

Figure 30 presents the TG, Derivative Thermogravimetry (DTG), and DSC curves of the $NiWO_4$ amorphous precursor powder. The TG curves reveal a series of mass loss-related decomposition reactions, connected to different exothermic events as indicating the DSC curve.

Figure 30- TG, DTG, and DSC curves of the $NiWO_4$ precursor powder

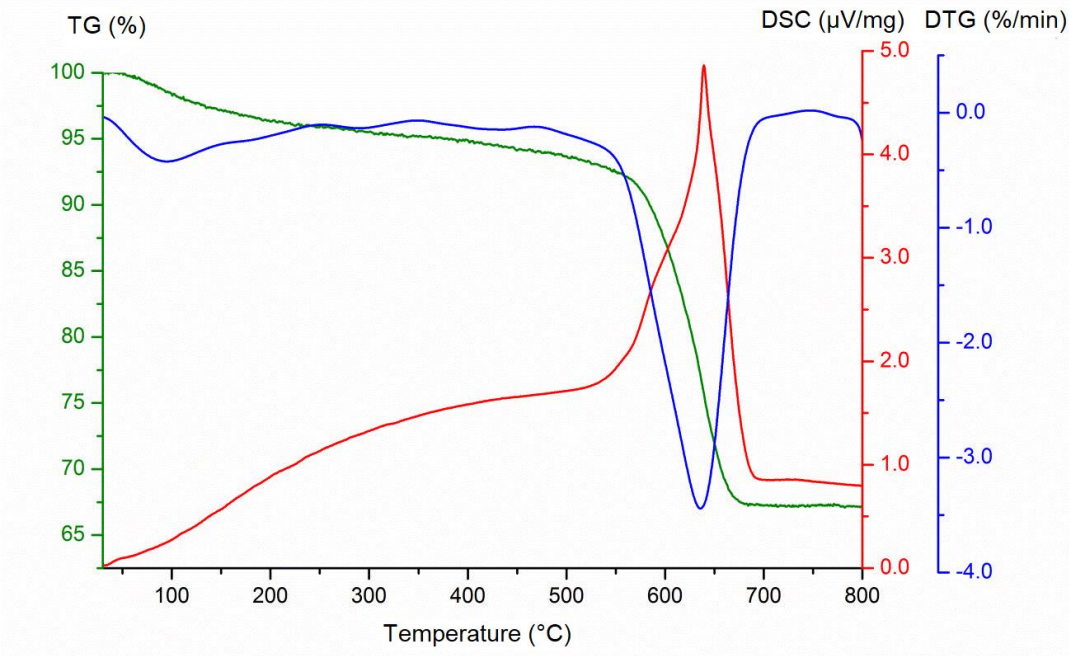


Source: author

Development of these decomposition processes should be described considering the complexation of nickel with citric acid leads to the following reaction, noting formation of nitric acid, and water as products (Equation 43).

$$Ni(NO_3)_2 \cdot 6H_2O + 2C_6H_8O_7 \rightarrow Ni(C_6H_7O_7)_2 + 2HNO_3 + 6H_2O \quad (43)$$

Meanwhile, the tungsten complexation reactions occur as follows, forming ammonium hydroxide (Equations 44-46).

$$H_2WO_{4(aq.)} \xrightarrow{90\ ^\circ C} WO_3 + H_2O \quad (44)$$

$$WO_3 + H_2O + 2\ NH_4OH \rightarrow W^{2+} + 2NH_4^+ + 2OH^- + O_2(g) \quad (45)$$

$$W^{2+} + 2NH_4^+ + 2OH^- + 2\ C_6H_8O_7 \rightarrow W(C_6H_7O_7)_2 + 2H^+ + 2NH_4^+ + 2OH^- \quad (46)$$

Mixing these metallic complexes (metallic citrates) above 70 °C triggers the onset of the esterification reaction between metal citrate and ethylene glycol, as follows (Equation 47):

$$M^{n+}\ [OCOCH_2C(OH)(COOH)CH_2COOH]_x + 3HOCH_2CH_2OH \rightarrow$$
$$M^{n+}[OCOCH_2C(OH)(COOH)CH_2COOCH_2CH_2OH]_x + xH_2O \quad (47)$$

For the $NiWO_4$ compound studied here, the polyesterification reaction occurs continuously until the polymer network is formed. This network is expected to consist of the following basic units (Equation 48):

$$\{W^{4+}[OCOCH_2C(OCH_2\text{-}\ldots)(COOCH_2\text{-}\ldots)CH_2COOCH_2\text{-}\ldots]_4\}$$
$$\{Ni^{2+}[OCOCH_2C(OCH_2\text{-}\ldots)(COOCH_2\text{-}\ldots)CH_2COOCH_2\text{-}\ldots]_2\} \quad (48)$$

Accordingly, the main organic compounds contained in the resin are water, ammonium hydroxide, nitric acid, and polyester. During heat treatment of the $NiWO_4$ precursor powder, total elimination of these compounds traduces into a mass loss of about 33% accomplished when approaching 700 °C, as reveals the TG curve in Figure 30. In terms of details, three thermal superposed events are visible in the TG curve. The first region occurs in the temperature range of 50 to 169 °C and accounts for a mass loss of around 2.6%, attributed to the elimination of adsorbed $H_2O$. The second region involves a mass loss of 5.3% from 169 to 562 °C, and this is related to dehydration of the resin, which becomes anhydrous due to the break of weakly bonded $CH_2$ groups. Finally, the third region goes from 562 to 672 °C, and it involves a mass

loss of 24.4%, attributed to the elimination of C–O groups as well as strongly bonded carbon atoms from the M–O–C groups, forming $CO/CO_2$.

Regarding the DSC curve, the elimination of water and decomposition of the organic compounds were also detected, all manifesting as exothermic events, followed by crystallization immediately taking place with a further increase of temperature. The highest crystallization peak occurs at ~639 °C. Table 7 summarizes the thermal events and corresponding temperature ranges, as inferred from the TG and DSC data.

Table 7- Results of thermal analyses for the $NiWO_4$ sample

| **Temperature range from TG (°C)** | **Weight loss (%) from TG** | **Thermal event details** |
|---|---|---|
| 50–169 | 2.6 | $H_2O$ and adsorbed gases elimination |
| 169–562 | 5.3 | Polymeric degradation (-$CH_2$- groups) |
| 562–672 | 24.4 | Polymeric degradation (-CO- and -COO- groups) |

Source: author

5.3.2. Structural analysis

Crystallization and phase development were accompanied by XRD technique. The data are shown in Figure 31.

Figure 31- XRD patterns of $NiWO_4$ powders after annealing at 500, 600, 700, and 800 ℃ for 2 h

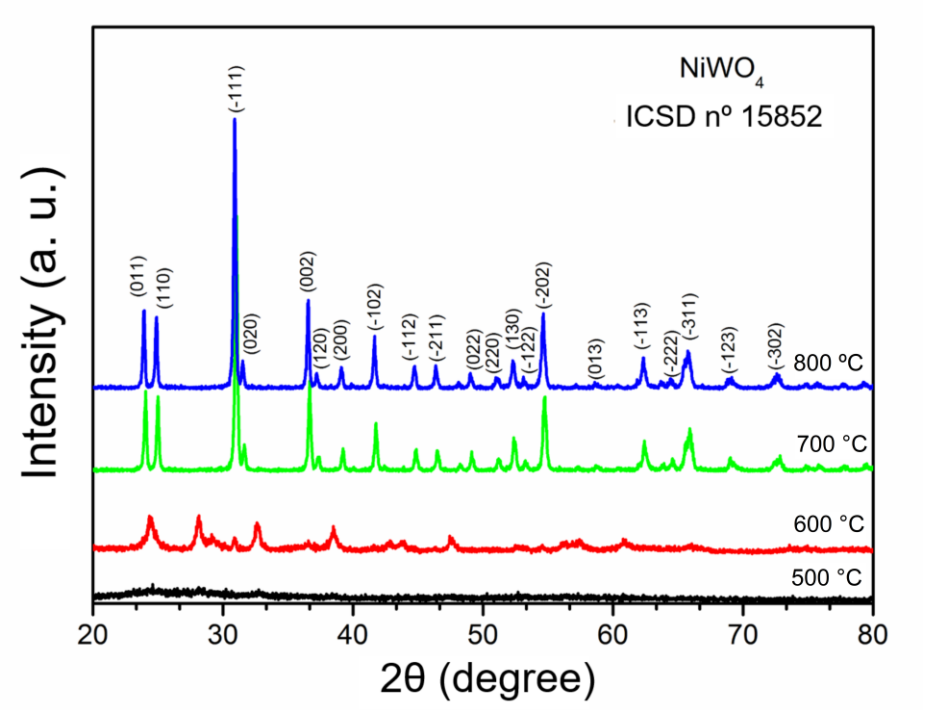


Source: author

It is observed that, after heat treatment at 500 ℃/2 h, the $NiWO_4$ precursor powder still reveals amorphous, while heat treatment at 600 ℃/2 h shows that formation of the crystalline phase already occurred, but with traces of $WO_3$, as also reported by Quintana-Melgoza *et al.*. [171] Annealing the powder at 700 and 800 ℃/2 h allows synthesizing $NiWO_4$ powder without spurious phases, in good agreement with observation of a huge DSC peak at ~639 ℃ (Figure 30) from the thermal analyses measurements conducted in dynamic mode (10 ℃·$min^{-1}$). This peak is asymmetric towards lower temperatures, suggesting to involve an overlap with a low-intensity one, most likely related to synthesis of the above-mentioned $WO_3$ phase when approaching 600 ℃ (Figure 31). In particular, the $NiWO_4$ was indexed in the wolframite monoclinic structure (space group: *P*2/*c*, with *Z* = 2), characterized by alternating layers of transition-metal and tungsten atoms parallel to the (100) plane. This is a structure where the oxygen atoms are hexagonally closely packed, and the metal ions occupy a quarter of all the octahedral sites. [172] The crystallite size in the $NiWO_4$ powder was estimated from the XRD data by using the Scherrer equation (49):

$$Dc = \frac{K\lambda}{\beta \cos\theta} \tag{49}$$

where $\beta$ is the breadth of the observed diffraction line at its half intensity maximum, $K$ is a shape factor and usually is ~0.9, $\lambda$ is the wavelength of X-ray source that used in XRD measurements, and $\theta$ is the corresponding angle. The results are 43 and 47 nm after heat treatments at 700 and 800 ℃, respectively.

### 5.3.3. UV–Vis spectra

The Figure 32 shows the UV–Vis spectra performed in the diffuse reflectance mode of the $NiWO_4$ powders annealed at 500 up to 800 ℃/2 h. The pictures of each sample are also presented. As can be seen in Figure 32 and XRD results, $NiWO_4$ sample annealed at 500 ℃ is a black powder in which the material is amorphous, explaining the spectra observed. As the temperature increases, the $NiWO_4$ powder crystallizes and becomes yellow. The reflectance spectra of the samples annealed at 600, 700, and 800 ℃ show broad peak centered in the yellow and a low peak in blue region of the spectra.

Figure 32- Reflectance spectra of $NiWO_4$ samples calcined at 500–800 ℃/2 h

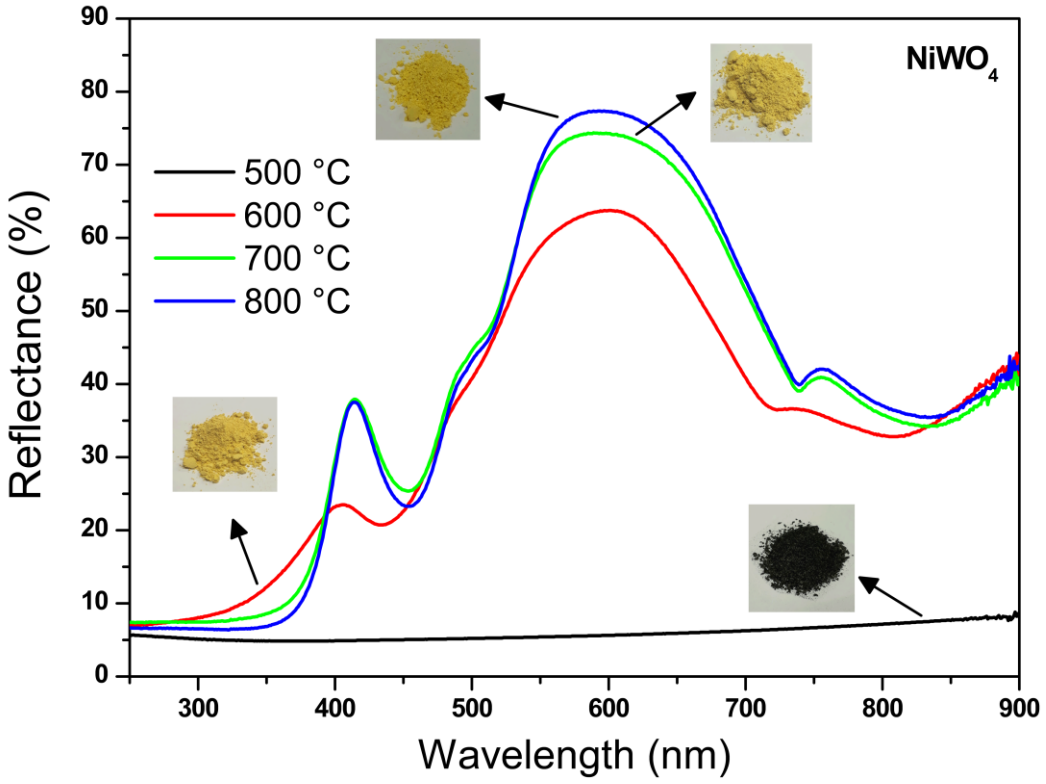


Source: author

Qualitative and quantitative information about the color of the samples are shown in Table 8 which presents the colorimetric coordinates ($L^*$, $a^*$, and $b^*$) of the $NiWO_4$ stable samples calcined at 700 and 800 °C/2 h.

Table 8- Colorimetric coordinates ($L^*$, $a^*$, and $b^*$) of $NiWO_4$ samples calcined at 700 and 800 °C/2 h, using light source type D65-10º (day light), following the CIE-L*a*b* standard colorimetric method

| Samples | $L^*$ | $a^*$ | $b^*$ |
|---|---|---|---|
| Standard (A) | 99.45 | -0.09 | -0.04 |
| Ni700 (D) | 85.31 | 3.07 | 38.32 |
| Ni800 (E) | 85.36 | 4.93 | 42.95 |

Source: author

The data were collected using light source type D65-10º (day light) and analyzed following the CIE-L*a*b* standard colorimetric method. Figure 33 shows the CIELab graphics of such $NiWO_4$ samples.

Figure 33- (a) CIELab graphics of the $NiWO_4$ samples calcined at 700 and 800 °C/2 h. Pictures of samples calcined at (b) 700 and (c) 800 °C/2 h

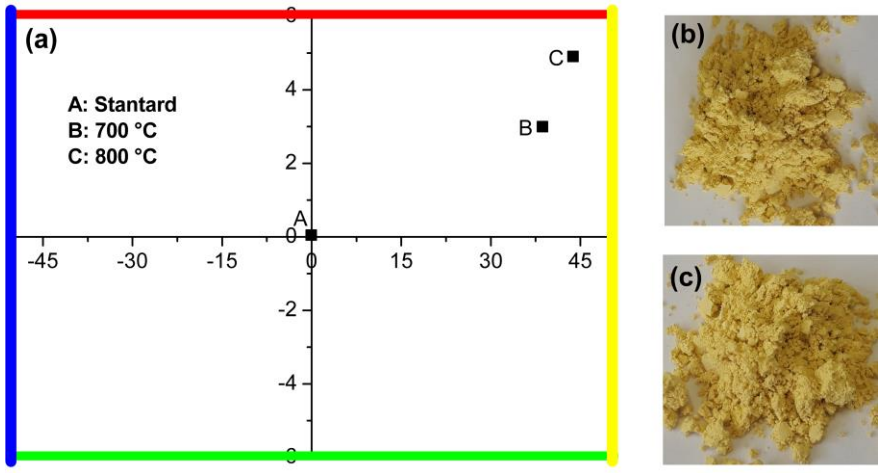


Source: author

The color of $Ni^{2+}$-based compounds is directly influenced by the symmetry of its site. [173] The degeneracy of the $^3T_{1g}$, $^3T_{2g}$, and $^3E_g$ states of $Ni^{2+}$ in octahedral geometry are lifted, and multiple-absorption bands occur when $Ni^{2+}$ is situated in a coordination environment of low symmetry. Bands split by low symmetry will show peak wavelengths, which are polarization

dependent. [173] Bright yellow color results when $Ni^{2+}$ is in a deltahedric-coordinated site significantly distorted from the octahedral symmetry. Increased absorption intensity occurs when the metal ion *d–d* bands are in proximity to an ultraviolet charge transfer band.

Calculated from reflectance, the absorbance spectra of these powders were also processed, the behavior of which revealed qualitatively similar from sample to sample. The results allowed to estimate band gaps according to $\alpha h\nu = B(h\nu - E_g)^n$ [152] where $\alpha$ is the absorption coefficient of the material (calculated from the absorption spectra), *h* is the Plank's constant, $\nu$ is the frequency of the radiation, *B* is a constant (dependent on the nature of the material), and $E_g$ is the energy of the band gap. *n* is a coefficient dependent on the type of transition considered: $n = 1/2$ for allowed direct transitions, while $n = 2$ for allowed indirect transitions.

Figure 34 depicts the absorbance spectra for $NiWO_4$ annealed at 700 and 800 °C. In summary, absorbance bands at 1.55, 1.72, 2.85, and 3.95 eV applied for the sample heat treated at 600 °C, resulting slightly shifted to 1.48, 1.68, 2.73, and 3.84 eV for the samples heat treated at 700 and 800 °C. All these values are very close to those found by de Oliveira *et al.*. [174] We note that the first two bands of low intensity are localized in the blue region, while the third and fourth ones with higher intensity lie in the ultraviolet region. As indicated in Figure 34, these bands have been proposed to arise from presence of $Ni^{2+}$ and charge transfer (CT) between clusters. [174] In particular, the bands at 1.68 and 2.73 eV would originate from the forbidden electronic transitions from $3A_{2g}$ to $1E_g$ and $1T_{2g}$, respectively, while the last band at 3.84 eV would involve charge transfer transitions. In addition, Cimino *et al.* [175] reported that $Ni^{2+}O_4$ presents a $3T_1 \rightarrow 1T_2$ transition at 1.56–1.60 eV. Based on this information, we believe that the band at 1.48 eV should be assigned to the presence of $Ni^{2+}O_4$, indicating that Frenkel defects are present in $NiWO_4$ with the dislocation of $Ni^{2+}$ from octahedral to tetrahedral sites. [174]

Figure 34- Absorbance spectra of the $NiWO_4$ annealing at 700 and 800 °C/2 h

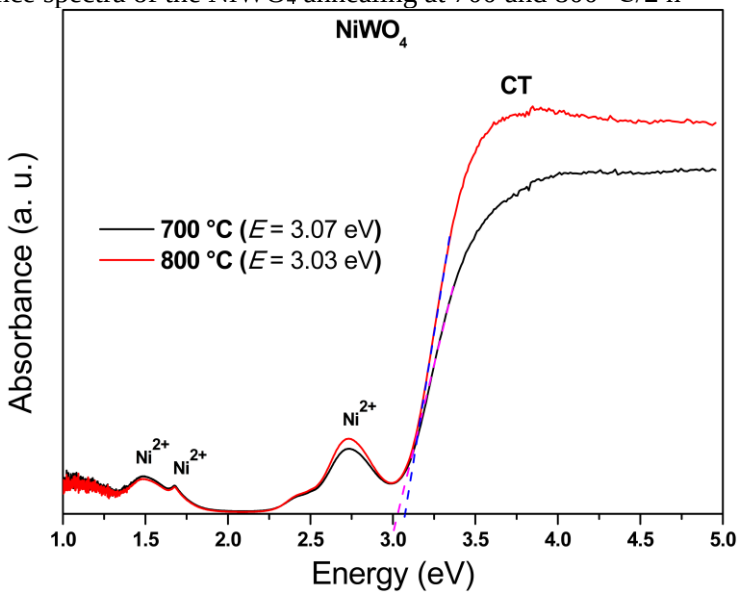


Source: author

5.3.4. Field emitting gun–scanning electron microscopy (FEG–SEM) analysis

Figure 35 shows representative FEG–SEM micrograph from the powder heat treated at 700 °C/2 h. This reveals to be here dealing with spherical-like packed particles, each with an average size of ~90 nm. This value is about twice the crystallite size estimated by XRD. For application as ceramic pigments, it is known that using nanoparticles is advantageous in order to produce more uniform and intense colors because of the huge surface area when compared to micrometer-sized particles. [176]

Figure 35- SEM morphology of the $NiWO_4$ powder calcined at 700 °C/2 h

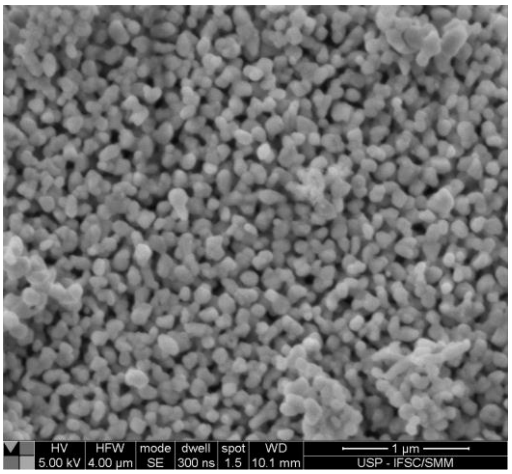


Source: author

3.3.5. Raman analysis

According to group theory calculations, tungstates with triclinic or monoclinic structures exhibit 36 different Raman vibrational modes, 18 of which are expected to be active modes (8Ag +10Bg). Figure 36 is an example of the Raman data collected for the $NiWO_4$ powder heat treated at 700 and 800 ℃/2 h and Table 9 shows a comparison of the vibrational modes and the results found from Ref. [150]. Actually, 18 active Raman modes were observed, in total agreement with the results reported by Ross-Medgaarden and Wachs. [177] In general, according to Ref., [178] vibrational modes observed in the Raman spectra of tungstates may be classified into two groups, namely, external (< 600 $cm^{-1}$) and internal (> 600 $cm^{-1}$) modes. [177] The vibrational external modes are related to a lattice phonon, which involves the motion of distorted octahedral [$NiO_6$] clusters with symmetry and rigid cell units. Meanwhile, vibrational internal modes are related to the vibration of the distorted octahedral [$WO_6$] clusters in the lattice, assuming that the center of mass is in a stationary state. Still according to Ross-Medgaarden and Wachs, [177] the position of the most intense band, located at 891 $cm^{-1}$ in Figure 36, is associated with the $WO_6$ symmetric stretching vibration.

Therefore the characteristic vibrational modes which are shown in the Raman spectrum confirm the presence of a single phase, in agreement with the results of the XRD measurement.

Figure 36- Raman spectra of the $NiWO_4$ powder calcined at 700 and 800 ℃ for 2 h

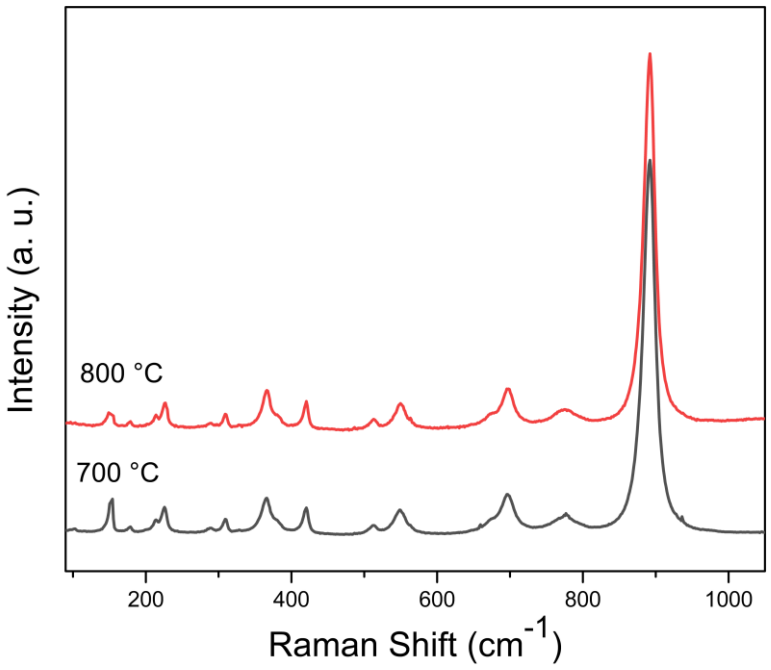


Source: author

Table 9- $NiWO_4$ vibration modes

| ***v*** **(cm $^{-1}$) [150]** | **Phonon symmetry** | **700 °C** | **800 °C** |
|---|---|---|---|
| 97 | $B_g$ | 102 | — |
| 149 | $A_g$ | 151 | 152 |
| 174 | $B_g$ | 178 | 177 |
| 197 | $B_g$ | 199 | 201 |
| 210 | $B_g$ | 213 | 214 |
| 223 | $A_g$ | 225 | 225 |
| 287 | $A_g$ | 288 | 288 |
| 307 | $A_g$ | 308 | 309 |
| 326 | $B_g$ | 327 | 328 |
| 363 | $A_g$ | 365 | 365 |
| 380 | $B_g$ | 378 | 379 |
| 418 | $A_g$ | 419 | 419 |
| 512 | $B_g$ | 512 | 513 |
| 549 | $A_g$ | 548 | 549 |
| 675 | $B_g$ | 673 | 673 |
| 697 | $A_g$ | 696 | 696 |
| 775 | $B_g$ | 776 | 774 |
| 893 | $A_g$ | 891 | 890 |

Source: author

5.3.6. Photoluminescence studies

Figure 37 illustrates the photoluminescence spectra for the $NiWO_4$ samples annealed at 500–800 °C/2 h, collected towards the 350–850 nm wavelength range, using 290 nm as excitation wavelength. Photoluminescence spectra are a fingerprint of electronic transitions associated with the intrinsic emission occurring, here, within the wolframite structure. The $NiWO_4$ powders showed a broad deep blue–green emission band, which was enhanced with increasing crystallinity of the powders. These patterns are similar to those observed in other wolframite compounds, [179] in which the emission bands were argued to arise from the $WO_6^{6-}$ complex, along with defects in the crystal structure. Previous studies [180; 181] proposed that blue and green emissions may be due to the intrinsic $WO_6^{6-}$ complex with a double emission from one and the same center ($^3T_{1u}$–$^1A_{1g}$), while the yellow emission results from recombination of electron-hole pairs localized at oxygen atom-deficient tungstate ions. There is an additional suggestion from refs. [179; 182], according to which self-trapped excision in tungstate crystals with strong electron–phonon coupling may account for the blue band, and the transitions of $T_{2u}$–$T_{2g}$ and $T_{1g}$–$T_{2g}$ in the $WO_6^{6-}$ complex could be responsible for the observation of green and yellow bands.

Figure 37- PL emission spectra at room temperature from the $NiWO_4$ powder calcined at 500–800 °C for 2 hours

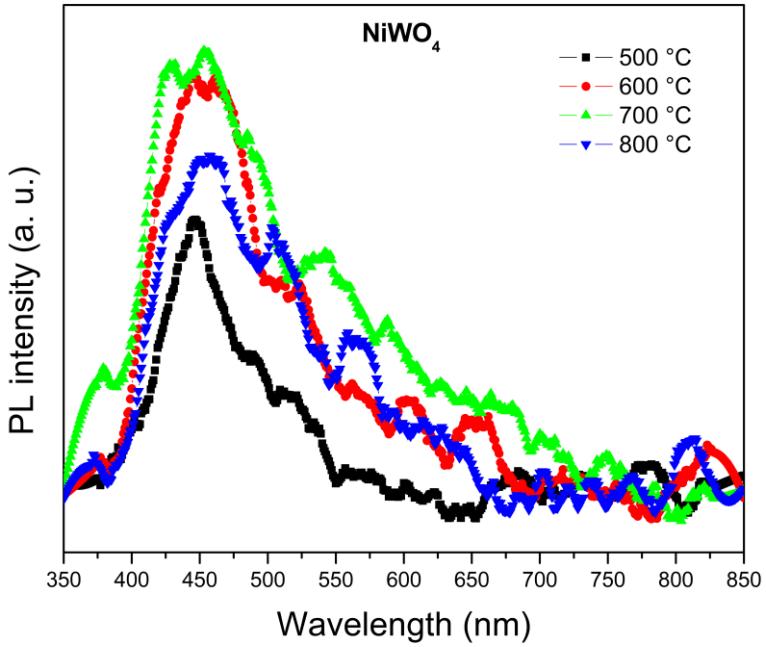


Source: author

As can be seen in Figure 37 that the $NiWO_4$ emission in the visible range between 350 and 700 nm, which means that it can absorb all light from the visible spectrum, which makes it a good material for luminescent applications as in banners and road signs, for example, using white light that contains all the colors of the visible spectrum. Another observation is that for samples calcined at 600, 700, and 800 ℃, they have a higher intensity of light emission and are more visible when they are illuminated.

## 5.4. CONCLUSIONS

$NiWO_4$ nanopowders were successfully obtained by the polymeric precursor method after annealing at 700 ℃/2 h. The $NiWO_4$ was indexed in the wolframite monoclinic structure (space group: *P*2/*c*, with $Z = 2$), noting that increasing the calcination temperature also led to an increase in structural ordering. Bright yellow nickel compounds occur as a consequence of nickel entering in deltaedric-coordinated sites, representing a significant distortion of the octahedral geometry. The color is a result of electronic transitions related with $Ni^{2+}$. In addition, 18 active Raman modes were identified for $NiWO_4$ powders heat treated at 700 and 800 ℃. The $NiWO_4$ powders showed a broad deep blue–green emission band, and calcined samples of 600 to 800 ℃ are the most capable of emitting light when illuminated by white light. Overall, the results show that $NiWO_4$ may be a promising material for industrial application as luminescent pigments. Advantages of this material include the fact that it is a non-toxic inorganic material with good chemical stability and reproducibility, as compared to organic compounds.

**Acknowledgements**

The authors gratefully acknowledge the financial support from Brazilian research funding agencies, namely, FAPESP (under grant numbers 2013/07909-4 and 2013/07296-2), CAPES, and CNPq (under grant number 470069/2013-9).

## 6. GENERAL CONCLUSION

In this thesis, copper ($CuWO_4$), nickel ($NiWO_4$) and zinc ($ZnWO_4$) tugstates were recorded in three distinct themes: catalysis, photocatalysis and pigments. In the application in catalysis, the Cu, Ni and Zn tungstates were synthesized by the polymeric precursor method (PPM) and their catalytic activity was evaluated as a function of the conversion of thioanisole to methyl phenyl sulfoxide and methyl phenyl sulfone. The catalytic activity was evaluated according to the nature of the catalyst, reaction rate, temperature and $H_2O_2$ concentration. We concluded that the ideal temperature is 75 ° C, time of 12 hours and 0.1 mL was the concentration of $H_2O_2$. $CuWO_4$ was the most effective catalyst mainly due to the greater number of vacancies / oxygen mobility that are proportional to the greater catalytic activity. In the application in photocatalysis, copper tunsgtate was synthesized by the methods of Coprecipitation (CM), Microwave assisted hydrothermal (HM) and Polymeric precursors (PPM) and its photocatalytic activity was evaluated for the degradation of the rhodamine B dye in search of understanding the response of the synthesis method in the material properties and consequently in the photocatalytic response. The influence of the oxidizing agent $H_2O_2$ and the sodium oxalate and silver nitrate scavengers were obtained in the reaction. We conclude that $CuWO_4$ can be photoactive with visible radiation and that it has the potential to degrade organic molecules. The recombination process can be delayed by the use of scavengers and that in the presence of $Ag^+$, the degradation reaction of the rhodamine B molecule was favored, degrading 100% in just 20 minutes of exposure in visible light. The most relevant properties that may have influenced the catalytic efficiency for surface loading (-38.5 mV for PPM <-29.7 mV for CM <-16.2 mV for HM) and the amount of oxygen vacancies (PPM> HM> CM ). In the Pigment application, $NiWO_4$ was synthesized by the polymeric precursors method for the manufacture of a yellow pigment. The material was evaluated for its stability, color pattern and luminescence and reproducibility. $NiWO_4$ was stable for calcination temperatures above 700 ° C, the yellow color is due to the electronic transitions of $Ni^{2+}$. We obtained particles of uniform size and nanometer scale. There was light emission in the blue-green region when illuminated, luminescent properties.

REFERENCES


[1] MAUTER, M.; ELIMELECH, M. Environmental applications of carbon-based nanomaterials. **Environmental Science & Technology,** v. 42, n. 16, p. 5843-5859, AUG 15 2008 2008. ISSN 0013-936X.

[2] CHRISTODOULOU, L.; VENABLES, J. Multifunctional material systems: The first generation. **Jom-Journal of the Minerals Metals & Materials Society,** v. 55, n. 12, p. 39-45, DEC 2003 2003. ISSN 1047-4838.

[3] GOESMANN, H.; FELDMANN, C. Nanoparticulate Functional Materials. **Angewandte Chemie-International Edition,** v. 49, n. 8, p. 1362-1395, 2010. ISSN 1433-7851.

[4] LONGO, V. et al. Potentiated Electron Transference in alpha-Ag2WO4 Microcrystals with Ag Nanofilaments as Microbial Agent. **Journal of Physical Chemistry a,** v. 118, n. 31, p. 5769-5778, AUG 7 2014 2014. ISSN 1089-5639.

[5] LIN, Z. et al. Electronic Reconstruction of alpha-Ag2WO4 Nanorods for Visible-Light Photocatalysis. **Acs Nano,** v. 9, n. 7, p. 7256-7265, JUL 2015 2015. ISSN 1936-0851.

[6] CHEN, H.; XU, Y. Photoactivity and stability of Ag2WO4 for organic degradation in aqueous suspensions. **Applied Surface Science,** v. 319, p. 319-323, NOV 15 2014 2014. ISSN 0169-4332.

[7] WANG, X. et al. Hierarchically porous metastable beta-Ag2WO4 hollow nanospheres: controlled synthesis and high photocatalytic activity. **Nanotechnology,** v. 24, n. 16, APR 26 2013 2013. ISSN 0957-4484.

[8] YOUREY, J.; BARTLETT, B. Electrochemical deposition and photoelectrochemistry of CuWO4, a promising photoanode for water oxidation. **Journal of Materials Chemistry,** v. 21, n. 21, p. 7651-7660, 2011 2011. ISSN 0959-9428.

[9] YOUREY, J. et al. Chemical Stability of CuWO4 for Photoelectrochemical Water Oxidation. **Journal of Physical Chemistry C,** v. 117, n. 17, p. 8708-8718, MAY 2 2013 2013. ISSN 1932-7447.

[10] AHMADI, F.; RAHIMI-NASRABADI, M.; EGHBALI-ARANI, M. The synthesize of CuWO4 nano particles by a new morphological control method, characterization of its photocatalytic activity. **Journal of Materials Science-Materials in Electronics,** v. 28, n. 7, p. 5244-5249, APR 2017 2017. ISSN 0957-4522.

11 BI, Y. et al. NiWO4 nanoparticles: a promising catalyst for hydrodesulfurization. **Chemical Communications,** v. 46, n. 39, p. 7430-7432, 2010 2010. ISSN 1359-7345.

12 HE, G. et al. One pot synthesis of nickel foam supported self-assembly of NiWO4 and CoWO4 nanostructures that act as high performance electrochemical capacitor electrodes. **Journal of Materials Chemistry a,** v. 3, n. 27, p. 14272-14278, 2015 2015. ISSN 2050-7488.

13 NIU, L. et al. Simple Synthesis of Amorphous NiWO4 Nanostructure and Its Application as a Novel Cathode Material for Asymmetric Supercapacitors. **Acs Applied Materials & Interfaces,** v. 5, n. 16, p. 8044-8052, AUG 28 2013 2013. ISSN 1944-8244.

14 BARZGARI, Z.; ASKARI, S.; GHAZIZADEH, A. Fabrication of nanostructured CuWO4 for photocatalytic degradation of organic pollutants in aqueous solution. **Journal of Materials Science-Materials in Electronics,** v. 28, n. 4, p. 3293-3298, FEB 2017 2017. ISSN 0957-4522.

15 SCHOFIELD, P.; KNIGHT, K.; CRESSEY, G. Neutron powder diffraction study of the scintillator material ZnWO4. **Journal of Materials Science,** v. 31, n. 11, p. 2873-2877, JUN 1 1996 1996. ISSN 0022-2461.

16 PULLAR, R.; FARRAH, S.; ALFORD, N. MgWO4, ZnWO4, NiWO4 and CoWO4 microwave dielectric ceramics. **Journal of the European Ceramic Society,** v. 27, n. 2-3, p. 1059-1063, 2007 2007. ISSN 0955-2219.

17 HUANG, G.; ZHU, Y. Synthesis and photocatalytic performance of ZnWO4 catalyst. **Materials Science and Engineering B-Solid State Materials For Advanced Technology,** v. 139, n. 2-3, p. 201-208, MAY 15 2007 2007. ISSN 0921-5107.

18 FU, H. et al. Photocatalytic activities of a novel ZnWO4 catalyst prepared by a hydrothermal process. **Applied Catalysis a-General,** v. 306, p. 58-67, JUN 7 2006 2006. ISSN 0926-860X.

19 QIAN, R. et al. Charge carrier trapping, recombination and transfer during TiO2 photocatalysis: An overview. **Catalysis Today,** v. 335, p. 78-90, SEP 1 2019 2019. ISSN 0920-5861.

20 CHO, I. et al. Branched TiO2 Nanorods for Photoelectrochemical Hydrogen Production. **Nano Letters,** v. 11, n. 11, p. 4978-4984, NOV 2011 2011. ISSN 1530-6984.

21 MUTHAMIZH, S. et al. **Solid State Synthesis of Copper Tungstate Nanoparticles and its Electrochemical Detection of 4-chlorophenol**. 58th DAE Solid State Physics

Symposium. Thapar Univ, Patiala, INDIA: Amer Inst Physics. Dec 17-21, 2013. 508-510 p.

[22] SILVA, J. B.; RODRIGUES, J. A. J.; NONO, M. C. A. **Caracterização de materiais catalíticos**. 2008. Instituto de Pesquisas Espaciais

[23] Specificity in Catalytic Hydrogenolysis by Metals. **Advances in Catalysis,** v. 23, p. 91 - 119, 1973. ISSN 0360-0564.

[24] SCHMAL, M. **Catálise Heterogênea**. 2018.

[25] VENTURA, W. M. **Preparação de catalizadores heterogêneos a base de $Nb_2O_5$ e $CeO_2$ para oxidação da anilina em fase líquida**. 2017. 59 Departamento de Química, Universidade Federal de Ouro Preto

[26] FRANCO, R. L. M. **Desenvolvimento de catalisadores de óxidos de metais de transição suportados em MCM-41 para dessulfurização oxidativa de dibenzotiofeno**. 2013. 128, Universidade Federal de Sergipe

[27] PEREIRA, L. G. F. **Desenvolvimento de materiais catalíticos à base de óxidos mistos para a decomposição do monopropelente peróxido de hidrogênio**. 2014. 83, Universidade de São Paulo

[28] MIRANDA, A. N. **Síntese e caracterização de óxidos mistos de cobalto, manganês e alumínio paradecomposição catalítica de $H_2O_2$ 70% e geração de vapor**. 2016. 73, Universidade de São Paulo

[29] ALENCAR, L. et al. Preparation, characterization and catalytic application of Barium molybdate (BaMoO4) and Barium tungstate (BaWO4) in the gas-phase oxidation of toluene. **Ceramics International,** v. 43, n. 5, p. 4462-4469, APR 1 2017 2017. ISSN 0272-8842.

[30] DE BRITTO, N. N.; SILVA, V. B. M. Advanced Oxidative Process and environmental application. **Revista Eletrônica de Engenharia Civil,** v. 1, p. 36 - 47, 2012.

[31] DE ARAÚJO, K. S. et al. Processos oxidativos avançados: uma revisão de fundamentos e aplicações no tratamento de águas residuais urbanas e efluentes industriais. **Ambiente & Água - An Interdisciplinary Journal of Applied Science,** v. 11, 2016.

[32] FIOREZE, M.; DOS SANTOS, E. P.; SCHMACHTENBERG, N. Processos oxidativos avançados: fundamentos e aplicação ambiental. **Revista Eletrônica em Gestão, Educação e Tecnologia Ambiental**. 18**:** 79 - 91 p. 2014.

[33] BANERJEE, S. et al. New Insights into the Mechanism of Visible Light Photocatalysis. **Journal of Physical Chemistry Letters,** v. 5, n. 15, p. 2543-2554, AUG 7 2014 2014. ISSN 1948-7185.

[34] HOFFMANN, M. R. et al. Environmental applications of semiconductor photocatalysis. **Chemical Reviews,** v. 95, n. 1, p. 69-96, Jan-Feb 1995. ISSN 0009-2665.

[35] BOSE. Planck's law and light quantum hypothesis. **Zeitschrift Fur Physik,** v. 26, p. 178-181, Aug 1924. ISSN 0044-3328.

[36] SCHMIDT, W. **Materiais Elétricos: condutores e semicondutores**. 3ª. 2010. 152

[37] NOGUEIRA, R. F. P.; JARDIM, W. F. A fotocatálise heterogênea e sua aplicação ambiental. **Química Nova,** v. 21, p. 69 - 72, 1998.

[38] FERREIRA, I. V. L. **Fotocatálise heterogênea com $TiO_2$ aplicada ao tratamento de esgoto sanitário secundário**. 2005. 187 (Phd). Escola de Engenharia de São Carlos, Universidade de São Paulo

[39] VALENTE, J. P. S. et al. Synthesis and textural characterization of $CeO_2/TiO_2$ obtained by sol-gel process: photocatalysis of model compound potassium hidrogenphthalate. **Eclética Química,** v. 30, 2005.

[40] YU, J. et al. Enhanced photocatalytic activity of TiO2 powder (P25) by hydrothermal treatment. **Journal of Molecular Catalysis a-Chemical,** v. 253, n. 1-2, p. 112-118, JUL 1 2006 2006. ISSN 1381-1169.

[41] LIANG, L. et al. Fabrication of novel CuWO4 hollow microsphere photocatalyst for dye degradation under visible-light irradiation. **Materials Letters,** v. 182, p. 302-304, NOV 1 2016 2016. ISSN 0167-577X.

[42] QIN, X. et al. Enhanced photocatalytic activity for degrading Rhodamine B solution of commercial Degussa P25 TiO2 and its mechanisms. **Journal of Hazardous Materials,** v. 172, n. 2-3, p. 1168-1174, DEC 30 2009 2009. ISSN 0304-3894.

[43] SCHULTZ, D.; YOON, T. Solar Synthesis: Prospects in Visible Light Photocatalysis. **Science,** v. 343, n. 6174, p. 985-+, FEB 28 2014 2014. ISSN 0036-8075.

[44] LACOMBA-PERALES, R. et al. Optical absorption of divalent metal tungstates: Correlation between the band-gap energy and the cation ionic radius. **Epl,** v. 83, n. 3, p. 5, 2008. ISSN 0295-5075.

[45] KARTHIKEYAN, C. et al. Recent advances in semiconductor metal oxides with enhanced methods for solar photocatalytic applications. **Journal of Alloys and Compounds,** v. 828, p. 15, Jul 2020. ISSN 0925-8388. Disponível em: < <Go to ISI>://WOS:000522634300074 >.

[46] GÜRSES, A. et al. **Dyes and pigments**. 2016.

[47] SCHABBACH, L. M.; BERNARDIN, A. M.; FREDEL, M. C. Utilização da espectrofotometria no estudo da influência do percentual de zirconita na opacifição de um esmalte transparente. **Cerâmica Industrial,** v. 7, 2002.

[48] GURSES, A. et al. **Dye and Pigments: their structural and properties**. 2016.

[49] BUXBAUM, G. **Industrial Inorganic Pigments**. 1993.

[50] ATKINS, P. W.; JONES, L. **Princípios de química: questionando a vida moderna e o meio ambiente**. 5ª. 2012. 265

[51] DUDNICK, S. L. **Creative artmedium for forming artistic expressions having a latent luminescent image pattern** 1987.

[52] LANG, A. R. **Dyes and Pigments: New Research**. 2009. ISBN 978-1-60692-027-5.

[53] KIPPAX, P. **Why particle sizing?** Paint & Coatings Industry**:** 3 p. 2005.

[54] BONDIOLI, F.; MANDREDINI, T.; DE OLEIVEIRA, A. P. N. Pigmentos Inorgânic os: Projetos, Produção e Aplicação Industrial. **Cerâmica Industrial,** v. 3, 1998.

[55] LEWIS, A. P. **Pigment handbook: characterization and physical relationships**. 1ª. 1973.

[56] KELLEY, A. et al. Investigation and Application of Nanoparticle Dispersions of Pigment Yellow 185 using Organic Solvents. **Acs Applied Materials & Interfaces,** v. 2, n. 1, p. 61-68, JAN 2010 2010. ISSN 1944-8244.

[57] MARQUES, G. N. et al. Synthesis of yttrium aluminate doped with $Cr^{3+}$ using $MgF_2$–$Na_2B_4O_7$ as mineralizers to obtain red pigments for ceramic tiles application. **Ceramics International,** v. 46, n. 18, p. 27940 - 27950, 2020. ISSN 0272-8842.

[58] TURNER, A. Cadmium pigments in consumer products and their health risks. **Science of The Total Environment,** v. 657, p. 1409 - 1418, 2019. ISSN 0048-9697.

59 CAO, L.; FEI, X. Environmental substitution for $PbCrO_4$ pigment with inorganic-organic hybrid pigment. **Dyes and Pigments,** v. 142, p. 100 - 107, 2017. ISSN 0143-7208.

60 JACOB, K. T. Phase relationships in the system Ni-W-O and thermodynamic properties of $NiWO_4$. **Journal of materials science,** v. 12, 1977.

61 OLIVEIRA, Y. L. et al. Structural characterization, morphology, optical and colorimetric properties of NiWO4 crystals synthesized by the co-precipitation and polymeric precursor methods. **Journal of Molecular Structure,** v. 1221, p. 128774, 2020. ISSN 0022-2860.

62 HE, H. Y. Luminescence properties of NiWO4 powders and films prepared with novel methods. **Materials Research Innovations,** v. 12, n. 3, p. 138-141,

63 MILANO, M. L. et al. **Luminescent raiser road marker** 2017.

64 BECIDYAN, A. N. Luminescent pigments in security applications. **Color Research \& Application,** v. 20, n. 2, p. 124-130, 1995.

65 MENATI, S. et al. Synthesis and characterization of insoluble cobalt(II), nickel(II), zinc(II) and palladium(II) Schiff base complexes: Heterogeneous catalysts for oxidation of sulfides with hydrogen peroxide. **Comptes Rendus Chimie,** v. 19, n. 3, p. 347-356, MAR 2016 2016. ISSN 1631-0748.

66 WANG, D. et al. Oxidative desulfurization of fuel oil - Part I. Oxidation of dibenzothiophenes using tert-butyl hydroperoxide. **Applied Catalysis a-General,** v. 253, n. 1, p. 91-99, OCT 20 2003 2003. ISSN 0926-860X.

67 CARNIATO, F. et al. Niobium(V) Saponite Clay for the Catalytic Oxidative Abatement of Chemical Warfare Agents. **Angewandte Chemie-International Edition,** v. 53, n. 38, p. 10095-10098, SEP 15 2014 2014. ISSN 1433-7851.

68 JIN, W.; WENG, W.; ZHOU, Z. Mixed-Valence Vanadium (IV/V) Glycolates and Lactates with N-Heterocycle Ligands: Localized Structures and Catalytic Oxidation of Thioanisole. **European Journal of Inorganic Chemistry**, n. 9, p. 1228-1235, MAR 7 2019 2019. ISSN 1434-1948.

69 GHORBANLOO, M. et al. Synthesis, characterization, and catalytic activity for thioanisole oxidation of homogeneous and heterogeneous binuclear manganese(II) complexes with amino acid-based ligands. **Transition Metal Chemistry,** v. 38, n. 5, p. 511-521, AUG 2013 2013. ISSN 0340-4285.

[70] NEGI, S. et al. Disordered mesoporous V/TiO2 system for ambient oxidation of sulfides to sulfoxides. **Applied Catalysis a-General,** v. 452, p. 132-138, FEB 15 2013 2013. ISSN 0926-860X.

[71] NUZHDIN, A. et al. Homogeneous and heterogeneous catalytic oxidation of sulfides by H2O2 over zinc(II) compounds. **Dalton Transactions**, n. 47, p. 10481-10485, 2009 2009. ISSN 1477-9226.

[72] JEREB, M. Highly atom-economic, catalyst- and solvent-free oxidation of sulfides into sulfones using 30% aqueous H2O2. **Green Chemistry,** v. 14, n. 11, p. 3047-3052, 2012 2012. ISSN 1463-9262.

[73] MOUSSA, N. et al. Catalytic oxidation of thioanisole Ph-S-CH3 over VOx/SiO2 and VOx/Al2O3 catalysts prepared by sol-gel method. **Journal of Molecular Catalysis a-Chemical,** v. 255, n. 1-2, p. 62-68, AUG 1 2006 2006. ISSN 1381-1169.

[74] BEZAATPOUR, A. et al. Green oxidation of sulfides in solvent-free condition by reusable novel Mo(VI) complex anchored on magnetite as a high-efficiency nanocatalyst with eco-friendly aqueous H2O2. **Molecular Catalysis,** v. 436, p. 199-209, JUL 2017 2017. ISSN 2468-8231.

[75] CRUZ, P. et al. Selective oxidation of thioanisole by titanium complexes immobilized on mesoporous silica nanoparticles: elucidating the environment of titanium(iv) species. **Catalysis Science & Technology,** v. 9, n. 3, p. 620-633, FEB 7 2019 2019. ISSN 2044-4753.

[76] LU, J. et al. An isotetramolybdate-supported rhenium carbonyl derivative: synthesis, characterization, and use as a catalyst for sulfoxidation. **Dalton Transactions,** v. 47, n. 15, p. 5279-5285, APR 21 2018 2018. ISSN 1477-9226.

[77] YAMAGUCHI, S. et al. Selective Oxidation of Thioanisole with Hydrogen Peroxide using Copper Complexes Encapsulated in Zeolite: Formation of a Thermally Stable and Reactive Copper Hydroperoxo Species. **Acs Catalysis,** v. 8, n. 4, p. 2645-2650, APR 2018 2018. ISSN 2155-5435.

[78] THORNBURG, N.; NOTESTEIN, J. Rate and Selectivity Control in Thioether and Alkene Oxidation with H2O2 over Phosphonate-Modified Niobium(V)-Silica Catalysts. **Chemcatchem,** v. 9, n. 19, p. 3714-3724, OCT 10 2017 2017. ISSN 1867-3880.

[79] XU, Q. et al. Two New Sandwich-Type Polyoxomolybdates Functionalized with Diphosphonates: Efficient and Selective Oxidation of Sulfides to Sulfones. **Materials,** v. 10, n. 10, OCT 2017 2017. ISSN 1996-1944.

[80] HADDADI, H.; HAFSHEJANI, S.; FARSANI, M. Selective and Reusable Oxidation of Sulfides to Sulfoxides with Hydrogen Peroxide Catalyzed by Organic-Inorganic Polyoxometalate-Based Frameworks. **Catalysis Letters,** v. 145, n. 11, p. 1984-1990, NOV 2015 2015. ISSN 1011-372X.

[81] AL-MAKSOUD, W.; DANIELE, S.; SOROKIN, A. Practical oxidation of sulfides to sulfones by H(2)O(2) catalysed by titanium catalyst. **Green Chemistry,** v. 10, n. 4, p. 447-451, 2008 2008. ISSN 1463-9262.

[82] DOHERTY, S. et al. Efficient and selective hydrogen peroxide-mediated oxidation of sulfides in batch and segmented and continuous flow using a peroxometalate-based polymer immobilised ionic liquid phase catalyst. **Green Chemistry,** v. 17, n. 3, p. 1559-1571, 2015 2015. ISSN 1463-9262.

[83] KAMATA, K. et al. Heterogeneously Catalyzed Aerobic Oxidation of Sulfides with a BaRuO3 Nanoperovskite. **Acs Applied Materials & Interfaces,** v. 10, n. 28, p. 23792-23801, JUL 18 2018 2018. ISSN 1944-8244.

[84] ZHOU, X.; JI, H. Highly efficient selective oxidation of sulfides to sulfoxides by montmorillonite-immobilized metalloporphyrins in the presence of molecular oxygen. **Catalysis Communications,** v. 53, p. 29-32, AUG 5 2014 2014. ISSN 1566-7367.

[85] UEMATSU, T. et al. Molybdenum-doped alpha-MnO2 as an efficient reusable heterogeneous catalyst for aerobic sulfide oxygenation. **Catalysis Science & Technology,** v. 6, n. 1, p. 222-233, 2016 2016. ISSN 2044-4753.

[86] SATO, K. et al. Oxidation of sulfides to sulfoxides and sulfones with 30% hydrogen peroxide under organic solvent- and halogen-free conditions. **Tetrahedron,** v. 57, n. 13, p. 2469-2476, MAR 26 2001 2001. ISSN 0040-4020.

[87] HULEA, V. et al. Catalytic oxidation of thiophenes and thioethers with hydrogen peroxide in the presence of W-containing layered double hydroxides. **Applied Catalysis a-General,** v. 313, n. 2, p. 200-207, OCT 4 2006 2006. ISSN 0926-860X.

[88] KE, J. et al. Nanostructured Ternary Metal Tungstate-Based Photocatalysts for Environmental Purification and Solar Water Splitting: A Review. **Nano-Micro Letters,** v. 10, n. 4, OCT 2018 2018. ISSN 2311-6706.

[89] BELYAKOV, A.; KULIKOV, N. Production of nanopowders of yttrium-aluminum garnet by the pechini method. **Refractories and Industrial Ceramics,** v. 52, n. 1, p. 61-62, MAY 2011 2011. ISSN 1083-4877.

[90] KAKIHANA, M. "Sol-Gel" preparation of high temperature superconducting oxides. **Journal of Sol-Gel Science and Technology,** v. 6, n. 1, p. 7-55, 1996 1996. ISSN 0928-0707.

[91] SING, K. Reporting physisorption data for gas solid systems - with special reference to the determination of surface-area and porosity. **Pure and Applied Chemistry,** v. 54, n. 11, p. 2201-2218, 1982 1982. ISSN 0033-4545.

[92] XIA, J.; CHANG, K.; LI, S. Electronic structure and optical property of semiconductor nanocrystallites. **Computational Materials Science,** v. 30, n. 3-4, p. 274-277, AUG 2004 2004. ISSN 0927-0256.

[93] LIMA, A. et al. Facile preparation of CuWO4 porous films and their photoelectrochemical properties. **Electrochimica Acta,** v. 256, p. 139-145, DEC 1 2017 2017. ISSN 0013-4686.

[94] LACOMBA-PERALES, R. et al. Optical absorption of divalent metal tungstates: Correlation between the band-gap energy and the cation ionic radius. **Epl,** v. 83, n. 3, 2008 2008. ISSN 0295-5075.

[95] SADIQ, M.; SHENOY, U.; BHAT, D. NiWO4-ZnO-NRGO ternary nanocomposite as an efficient photocatalyst for degradation of methylene blue and reduction of 4-nitro phenol. **Journal of Physics and Chemistry of Solids,** v. 109, p. 124-133, OCT 2017 2017. ISSN 0022-3697.

[96] SOUZA, E. et al. Structural evolution, growth mechanism and photoluminescence properties of CuWO4 nanocrystals. **Ultrasonics Sonochemistry,** v. 38, p. 256-270, SEP 2017 2017. ISSN 1350-4177.

[97] ZHANG, W. et al. Cyclic voltammetry analysis of copper electrode performance in Na2WO4 solution and optical property of electrochemical synthesized CuWO4 nanoparticles. **Journal of Alloys and Compounds,** v. 690, p. 221-227, JAN 5 2017 2017. ISSN 0925-8388.

[98] ZAWAWI, S. et al. Structural and optical characterization of metal tungstates (MWO4; M=Ni, Ba, Bi) synthesized by a sucrose-templated method. **Chemistry Central Journal,** v. 7, MAY 1 2013 2013. ISSN 1752-153X.

[99] PEREIRA, P. et al. ZnWO4 nanocrystals: synthesis, morphology, photoluminescence and photocatalytic properties. **Physical Chemistry Chemical Physics,** v. 20, n. 3, p. 1923-1937, JAN 21 2018 2018. ISSN 1463-9076.

[100] REDDYPRASAD, P.; NAIDOO, M. Ultrasonic synthesis of high fluorescent C-dots and modified with CuWO4 nanocomposite for effective photocatalytic activity.

**Journal of Molecular Structure,** v. 1098, p. 146-152, OCT 15 2015 2015. ISSN 0022-2860.

101 POURMORTAZAVI, S. et al. Synthesis, structure characterization and catalytic activity of nickel tungstate nanoparticles. **Applied Surface Science,** v. 263, p. 745-752, DEC 15 2012 2012. ISSN 0169-4332.

102 AMOUZEGAR, Z. et al. Microwave engineering of ZnWO4 nanostructures: Towards morphologically favorable structures for photocatalytic activity. **Ceramics International,** v. 41, n. 7, p. 8352-8359, AUG 2015 2015. ISSN 0272-8842.

103 LONGO, V. et al. Understanding the origin of photoluminescence in disordered Ca0.60Sr0.40WO4: An experimental and first-principles study. **Chemical Physics,** v. 334, n. 1-3, p. 180-188, APR 20 2007 2007. ISSN 0301-0104.

104 WANG, Z. et al. Enhancing the Ethynylation Performance of CuO-Bi2O3 Nanocatalysts by Tuning Cu-Bi Interactions and Phase Structures. **Catalysts,** v. 9, n. 1, JAN 2019 2019.

105 ZACCHERIA, F. et al. Unravelling the properties of supported copper oxide: can the particle size induce acidic behaviour? **Dalton Transactions,** v. 42, n. 5, p. 1319-1328, 2013 2013. ISSN 1477-9226.

106 HONG, S. et al. Large Resistive Switching in Ferroelectric BiFeO3 Nano-Island Based Switchable Diodes. **Advanced Materials,** v. 25, n. 16, p. 2339-2343, APR 24 2013 2013. ISSN 0935-9648.

107 XIAO, J. et al. NiO microspheres with tunable porosity and morphology effects for CO oxidation. **Catalysis Science & Technology,** v. 1, n. 6, p. 999-1005, 2011 2011. ISSN 2044-4753.

108 DONPHAI, W. et al. Effect of magnetic field on CO2 conversion over Cu-ZnO/ZrO2 catalyst in hydrogenation reaction. **Journal of Co2 Utilization,** v. 16, p. 204-211, DEC 2016 2016. ISSN 2212-9820.

109 SHOZI, M. et al. An investigation of Cu-Re-ZnO catalysts for the hydrogenolysis of glycerol under continuous flow conditions. **Sustainable Energy & Fuels,** v. 1, n. 6, p. 1437-1445, AUG 2017 2017. ISSN 2398-4902.

110 SILVA, A. et al. Ce1-xSmxO1.9-delta nanoparticles obtained by microwave-assisted hydrothermal processing: an efficient application for catalytic oxidation of alpha-bisabolol. **Catalysis Science & Technology,** v. 4, n. 3, p. 814-821, 2014 2014. ISSN 2044-4753.

[111] WANG, X. et al. Selective Oxidation of Glycerol to Glyceraldehyde with H2O2 Catalyzed by CuNiAl Hydrotalcites Supported BiOCl in Neutral Media. **Catalysis Letters,** v. 149, n. 4, p. 1046-1056, APR 2019 2019. ISSN 1011-372X.

[112] SONG, Z. et al. Density functional study on the heterogeneous oxidation of NO over alpha-Fe2O3 catalyst by H2O2: Effect of oxygen vacancy. **Applied Surface Science,** v. 413, p. 292-301, AUG 15 2017 2017. ISSN 0169-4332.

[113] TUMULA, V. et al. Oxidation of sulfides to sulfones with hydrogen peroxide in the presence of acetic acid and Amberlyst 15. **Reaction Kinetics Mechanisms and Catalysis,** v. 107, n. 2, p. 449-466, DEC 2012 2012. ISSN 1878-5190.

[114] BROWN, M.; DEVITO, S. Predicting azo-dye toxicity. **Critical Reviews in Environmental Science and Technology,** v. 23, n. 3, p. 249-324, 1993 1993. ISSN 1064-3389.

[115] KANT, R. Textile dyeing industry an environmental hazard. **Nature Science,** v. 4, p. 22-26, 2012.

[116] ALMEIDA, E.; CORSO, C. Decolorization and removal of toxicity of textile azo dyes using fungal biomass pelletized. **International Journal of Environmental Science and Technology,** v. 16, n. 3, p. 1319-1328, MAR 2019 2019. ISSN 1735-1472.

[117] OLIVEIRA, R. G. D. **Caracterização das águas e efluentes em lavanderias de jeans no agreste pernambucano**. 2008. Programa de Pós-Graduação em Engenharia Civil, Universidade Federal de Pernambuco, Recife.

[118] KHAN, T. A. et al. Utilization of Fly ash as Low-Cost Adsorbent for the Removal of Methylene Blue, Malachite Green and Rhodamine B Dyes from Textile Wastewater. **Journal of environmental protection science,** v. 3, p. 11-22, 2009.

[119] KHAN, T.; NAZIR, M.; KHAN, E. Adsorptive removal of rhodamine B from textile wastewater using water chestnut (Trapa natans L.) peel: adsorption dynamics and kinetic studies. **Toxicological and Environmental Chemistry,** v. 95, n. 6, p. 919-931, JUL 1 2013 2013. ISSN 0277-2248.

[120] LAU, Y. et al. Coagulation-flocculation of azo dye Acid Orange 7 with green refined laterite soil. **Chemical Engineering Journal,** v. 246, p. 383-390, JUN 15 2014 2014. ISSN 1385-8947.

[121] ZHOU, M. et al. Degradation of organics in reverse osmosis concentrate by electro-Fenton process. **Journal of Hazardous Materials,** v. 215, p. 287-293, MAY 15 2012 2012. ISSN 0304-3894.

[122] LIN, J. et al. Tight ultrafiltration membranes for enhanced separation of dyes and Na2SO4 during textile wastewater treatment. **Journal of Membrane Science,** v. 514, p. 217-228, SEP 15 2016 2016. ISSN 0376-7388.

[123] ANDREOZZI, R. et al. Advanced oxidation processes (AOP) for water purification and recovery. **Catalysis Today,** v. 53, n. 1, p. 51-59, OCT 15 1999 1999. ISSN 0920-5861.

[124] JONES , B. M. F.; MARUTHAMAN, D.; MUTHURAJ, V. Construction of novel n-type semiconductor anchor on 2D honey comb like FeNbO 4 /RGO for visible light drive photocatalytic degradation of norfloxacin. **Journal of Photochemistry & Photobiology A: Chemistry**. 2020

[125] CHIU, Y. et al. Mechanistic Insights into Photodegradation of Organic Dyes Using Heterostructure Photocatalysts. **Catalysts,** v. 9, n. 5, MAY 2019 2019. ISSN 2073-4344.

[126] FERREIRA, S. S. **Tratamento fotocatalítico de água de lavagem, sintética e real, de solo contaminado com ácido etilenodiamino-n, n'-dissuccínico (edds), cobre e zinco**. 2015. Pós-graduação em Engenharia Química, Universidade Federal do Rio de Janeiro, Rio de Janeiro.

[127] DA SILVA, L. et al. An Understanding of the Photocatalytic Properties and Pollutant Degradation Mechanism of SrTiO3 Nanoparticles. **Photochemistry and Photobiology,** v. 92, n. 3, p. 371-378, MAY-JUN 2016 2016. ISSN 0031-8655.

[128] DUTTA, D. et al. Selective sorption and subsequent photocatalytic degradation of cationic dyes by sonochemically synthesized nano CuWO4 and Cu3Mo2O9. **Rsc Advances,** v. 5, n. 115, p. 94866-94878, 2015 2015. ISSN 2046-2069.

[129] MONTINI, T. et al. Synthesis, characterization and photocatalytic performance of transition metal tungstates. **Chemical Physics Letters,** v. 498, n. 1-3, p. 113-119, SEP 30 2010 2010. ISSN 0009-2614.

[130] BERNARDI, M. et al. Influence of the concentration of Sb2O3 and the viscosity of the precursor solution on the electrical and optical properties of SnO2 thin films produced by the Pechini method. **Thin Solid Films,** v. 405, n. 1-2, p. 228-233, FEB 22 2002 2002. ISSN 0040-6090.

[131] RUIZ-FUERTES, J. et al. High-pressure structural phase transitions in CuWO4. **Physical Review B,** v. 81, n. 22, JUN 29 2010 2010. ISSN 1098-0121.

[132] DOUMERC, J. et al. A photoelectrochemical study of cuwo4 single-crystals. **Physica Status Solidi a-Applied Research,** v. 82, n. 1, p. 285-294, 1984 1984. ISSN 0031-8965.

[133] PATTERSON, A. The Scherrer formula for x-ray particle size determination. **Physical Review,** v. 56, n. 10, p. 978-982, NOV 1939 1939. ISSN 0031-899X.

[134] DUPIN, J. et al. Systematic XPS studies of metal oxides, hydroxides and peroxides. **Physical Chemistry Chemical Physics,** v. 2, n. 6, p. 1319-1324, 2000 2000. ISSN 1463-9076.

[135] KANNAN, S.; MOHANRAJ, K.; SIVAKUMAR, G. Preparation of Bifunctional CuWO4-Based Heterostructure Nanocomposites for Noble-Metal-Free Photocatalysts. **Chemistryselect,** v. 2, n. 16, p. 4484-4498, MAY 31 2017 2017. ISSN 2365-6549.

[136] TIAN, C. et al. Elucidating the electronic structure of CuWO4 thin films for enhanced photoelectrochemical water splitting. **Journal of Materials Chemistry a,** v. 7, n. 19, p. 11895-11907, MAY 21 2019 2019. ISSN 2050-7488.

[137] TANG, Y. et al. Enhancement of the photoelectrochemical performance of CuWO4 films for water splitting by hydrogen treatment. **Applied Surface Science,** v. 361, p. 133-140, JAN 15 2016 2016. ISSN 0169-4332.

[138] CATTO, A. et al. Improving the ozone gas-sensing properties of CuWO4 nanoparticles. **Journal of Alloys and Compounds,** v. 748, p. 411-417, JUN 5 2018 2018. ISSN 0925-8388.

[139] JEYAKANTHAN, M. et al. Relaxor like colossal dielectric constant in CoWO4 and CoWO4/PbWO4 nanocomposites. **Journal of Materials Science-Materials in Electronics,** v. 30, n. 15, p. 14657-14668, AUG 2019 2019. ISSN 0957-4522.

[140] SANTOS, C. et al. Antiangiogenic evaluation of ZnWO4 nanoparticles synthesised through microwave-assisted hydrothermal method. **Journal of Drug Targeting,** v. 26, n. 9, p. 806-817, 2018 2018. ISSN 1061-186X.

[141] SEIDL, C. et al. Tin Tungstate Nanoparticles: A Photosensitizer for Photodynamic Tumor Therapy. **Acs Nano,** v. 10, n. 3, p. 3149-3157, MAR 2016 2016. ISSN 1936-0851.

[142] PROCTOR, A.; PANUGANTI, S.; BARTLETT, B. CuWO4 as a photocatalyst for room temperature aerobic benzylamine oxidation. **Chemical Communications,** v. 54, n. 9, p. 1101-1104, JAN 28 2018 2018. ISSN 1359-7345.

143 HE, X. et al. Synthesis and coloration of highly dispersed NiTiO3@TiO2 yellow pigments with core-shell structure. **Journal of the European Ceramic Society,** v. 37, n. 8, p. 2965-2972, JUL 2017 2017. ISSN 0955-2219.

144 WANROOIJ, P. et al. Extraction of CdS pigment from waste polyethylene. **Journal of Applied Polymer Science,** v. 100, n. 2, p. 1024-1031, APR 15 2006 2006. ISSN 0021-8995.

145 BAE, B. et al. Novel environmentally friendly inorganic yellow pigments based on gehlenite-type structure. **Ceramics International,** v. 42, n. 13, p. 15104-15106, OCT 2016 2016. ISSN 0272-8842.

146 KAWASAKI, T. et al. Markers of cadmium exposure in workers in a cadmium pigment factory after changes in the exposure conditions. **Toxicology and Industrial Health,** v. 20, n. 1-5, p. 51-56, JUN 2004 2004. ISSN 0748-2337.

147 JANSEN, M.; LETSCHERT, H. Inorganic yellow-red pigments without toxic metals. **Nature,** v. 404, n. 6781, p. 980-982, APR 27 2000 2000. ISSN 0028-0836.

148 ZHOU, Y. et al. Hierarchical FeWO4 Microcrystals: Solvothermal Synthesis and Their Photocatalytic and Magnetic Properties. **Inorganic Chemistry,** v. 48, n. 3, p. 1082-1090, FEB 2 2009 2009. ISSN 0020-1669.

149 HITHA, H.; JOSE, A.; VARGHESE, T. **Synthesis, Characterization and Photocatalytic Activity of $NiWO_4$ Nanoparticles**. AIP Conference Proceedings. 2082 2019.

150 HARSHAN, H. et al. Structural, optical and magnetic properties of nanophase NiWO4 for potential applications. **European Physical Journal B,** v. 91, n. 11, NOV 19 2018 2018. ISSN 1434-6028.

151 DU, X.; SHAO, Q.; ZHANG, X. Metal tungstate dominated NiCo2O4@NiWO4 nanorods arrays as an efficient electrocatalyst for water splitting. **International Journal of Hydrogen Energy,** v. 44, n. 5, p. 2883-2888, JAN 28 2019 2019. ISSN 0360-3199.

152 BABU, E. et al. Novel NiWO4 nanoberries morphology effect on photoelectrochemical properties. **Materials Letters,** v. 220, p. 209-212, JUN 1 2018 2018. ISSN 0167-577X.

153 RYU, J. et al. Microwave-assisted synthesis of nanocrystalline MWO4 (M : Ca, Ni) via water-based citrate complex precursor. **Ceramics International,** v. 31, n. 6, p. 883-888, 2005 2005. ISSN 0272-8842.

[154] HUANG, Y. et al. Ni0.85Co0.15WO4 nanosheet electrodes for supercapacitors with excellent electrical conductivity and capacitive performance. **Nano Energy,** v. 48, p. 430-440, JUN 2018 2018. ISSN 2211-2855.

[155] TIAN, J. et al. Solvothermal synthesis of NiWO4 nanostructure and its application as a cathode material for asymmetric supercapacitors. **Rsc Advances,** v. 8, n. 73, p. 41740-41748, 2018 2018. ISSN 2046-2069.

[156] POURMORTAZAVI, S. et al. Evaluation of photocatalytic and supercapacitor potential of nickel tungstate nanoparticles synthesized by electrochemical method. **New Journal of Chemistry,** v. 42, n. 24, p. 19934-19944, DEC 21 2018 2018. ISSN 1144-0546.

[157] DHAND, C. et al. Methods and strategies for the synthesis of diverse nanoparticles and their applications: a comprehensive overview. **Rsc Advances,** v. 5, n. 127, p. 105003-105037, 2015 2015.

[158] BLOVSKA, V.; BELINA, P.; SULCOVA, P. Synthesis of tungstate pigments of the formula MNd2W2O10 (M = Ni, Zn, Mn). **Journal of Thermal Analysis and Calorimetry,** v. 113, n. 1, p. 83-89, JUL 2013 2013. ISSN 1388-6150.

[159] GARCIA-PEREZ, U.; MARTINEZ-DE LA CRUZ, A.; PERAL, J. Transition metal tungstates synthesized by co-precipitation method: Basic photocatalytic properties. **Electrochimica Acta,** v. 81, p. 227-232, OCT 30 2012 2012. ISSN 0013-4686.

[160] FU, H. et al. Synthesis, characterization and photocatalytic properties of nanosized Bi2WO6, PbWO4 and ZnWO4 catalysts. **Materials Research Bulletin,** v. 42, n. 4, p. 696-706, APR 12 2007 2007. ISSN 0025-5408.

[161] SINGH, P. et al. Preparation of BSA-ZnWO4 Nanocomposites with Enhanced Adsorptional Photocatalytic Activity for Methylene Blue Degradation. **International Journal of Photoenergy,** v. 2013, 2013 2013. ISSN 1110-662X.

[162] SONG, X. et al. Photocatalytic activities of Cd-doped ZnWO4 nanorods prepared by a hydrothermal process. **Journal of Hazardous Materials,** v. 179, n. 1-3, p. 1122-1127, JUL 15 2010 2010. ISSN 0304-3894.

[163] CASALI, G. A. **Pigmentos de $TiO_2$ dopado com os metais de transição Cromo e Manganês**. 2001. Federal University of São Carlos

[164] KWON, T. et al. Zinc oxide thin film doped with Al2O3, TiO2 and V2O5 as sensitive sensor for trimethylamine gas. **Sensors and Actuators B-Chemical,** v. 46, n. 2, p. 75-79, FEB 15 1998 1998. ISSN 0925-4005.

165 DE OLIVEIRA, A. et al. Yellow ZnxNi1-xWO4 pigments obtained using a polymeric precursor method. **Dyes and Pigments,** v. 77, n. 1, p. 210-216, 2008 2008. ISSN 0143-7208.

166 KAKIHANA, M.; YOSHIMURA, M. Synthesis and characteristics of complex multicomponent oxides prepared by polymer complex method. **Bulletin of the Chemical Society of Japan,** v. 72, n. 7, p. 1427-1443, JUL 1999 1999. ISSN 0009-2673.

167 BERNARDI, M. et al. Thermal, structural and optical properties of Al2CoO4-Crocoite composite nanoparticles used as pigments. **Journal of Thermal Analysis and Calorimetry,** v. 97, n. 3, p. 923-928, SEP 2009 2009. ISSN 1388-6150.

168 PECHINI, M. P. **Method of preparing lead and alkaline earth titanates and niobates and coating method using the same to form a capacitor** 1963.

169 **Method of preparing lead and alkaline earth titanates and niobates and coating method using the same to form a capacitor** 1967.

170 CIE. **Commission internationale de l'Eclairage proceedings**. Cambridge University Press 1931.

171 QUINTANA-MELGOZA, J.; CRUZ-REYES, J.; AVALOS-BORJA, M. Synthesis and characterization of NiWO4 crystals. **Materials Letters,** v. 47, n. 4-5, p. 314-318, FEB 2001 2001. ISSN 0167-577X.

172 RUIZ-FUERTES, J. et al. High-pressure phase transitions and compressibility of wolframite-type tungstates. **Journal of Applied Physics,** v. 107, n. 8, APR 15 2010 2010. ISSN 0021-8979.

173 LEVER, A.; LONDON, G.; MCCARTHY, P. Single-crystal electronic-spectra of a series of trans nickel(ii) complexes with n,n'-diethylethylenediamine and n,n'-dimethylethylenediamine. **Canadian Journal of Chemistry-Revue Canadienne De Chimie,** v. 55, n. 17, p. 3172-3189, 1977 1977. ISSN 0008-4042.

174 DE OLIVEIRA, A. et al. Influence of the thermal treatment in the crystallization of NiWO4 and ZnWO4. **Journal of Thermal Analysis and Calorimetry,** v. 97, n. 1, p. 167-172, JUL 2009 2009. ISSN 1388-6150.

175 LOJACONO, M.; SCHIAVELLO, M.; CIMINO, A. Structural, magnetic, and optical properties of nickel oxide supported on eta-aluminas and gamma-aluminas. **Journal of Physical Chemistry,** v. 75, n. 8, p. 1044-+, 1971 1971. ISSN 0022-3654.

[176] BERNARDI, M. et al. Comparison of blue pigments prepared by two different methods. **Journal of the European Ceramic Society,** v. 22, n. 16, p. 2911-2919, DEC 2002 2002. ISSN 0955-2219.

[177] ROSS-MEDGAARDEN, E.; WACHS, I. Structural determination of bulk and surface tungsten oxides with UV-vis diffuse reflectance spectroscopy and Raman spectroscopy. **Journal of Physical Chemistry C,** v. 111, n. 41, p. 15089-15099, OCT 18 2007 2007. ISSN 1932-7447.

[178] KUZMIN, A.; KALINKO, A.; EVARESTOV, R. Ab initio LCAO study of the atomic, electronic and magnetic structures and the lattice dynamics of triclinic CuWO4. **Acta Materialia,** v. 61, n. 1, p. 371-378, JAN 2013 2013. ISSN 1359-6454.

[179] MOHAMMADI, S. et al. Synthesis of new dyes from imidazo[1,2-a]pyridine: tautomerism, spectroscopic characterisation, DFT/TD-DFT calculations, atoms in molecules analyses and antibacterial activities. **Journal of Chemical Research**, n. 3, p. 143-148, MAR 2017 2017. ISSN 1747-5198.

[180] OVECHKIN, A. et al. Luminescence of znwo4 and cdwo4 crystals. **Physica Status Solidi a-Applied Research,** v. 103, n. 1, p. 285-290, SEP 16 1987 1987. ISSN 0031-8965.

[181] LAMMERS, M.; BLASSE, G.; ROBERTSON, D. The luminescence of cadmium tungstate (cdwo4). **Physica Status Solidi a-Applied Research,** v. 63, n. 2, p. 569-572, 1981 1981. ISSN 0031-8965.

[182] GRIGORJEVA, L. et al. Time-resolved luminescence and absorption in CdWO4. **Radiation Measurements,** v. 29, n. 3-4, p. 267-271, JUN-AUG 1998 1998. ISSN 1350-4487.

# ATTACHMENT

1. Confirmation of submission: Paper 1

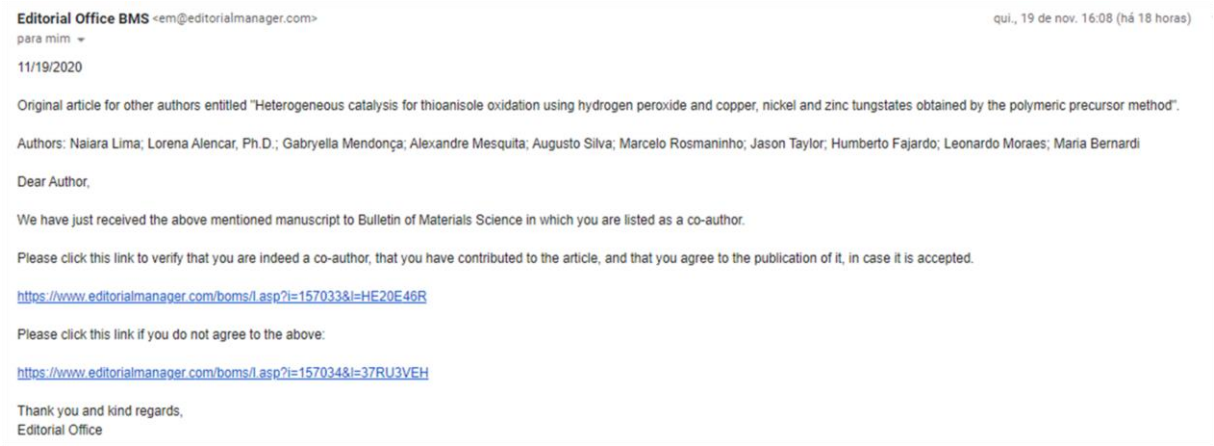

**Editorial Office BMS** <em@editorialmanager.com> qui., 19 de nov. 16:08 (há 18 horas)
para mim

11/19/2020

Original article for other authors entitled "Heterogeneous catalysis for thioanisole oxidation using hydrogen peroxide and copper, nickel and zinc tungstates obtained by the polymeric precursor method".

Authors: Naiara Lima; Lorena Alencar, Ph.D.; Gabryella Mendonça; Alexandre Mesquita; Augusto Silva; Marcelo Rosmaninho; Jason Taylor; Humberto Fajardo; Leonardo Moraes; Maria Bernardi

Dear Author,

We have just received the above mentioned manuscript to Bulletin of Materials Science in which you are listed as a co-author.

Please click this link to verify that you are indeed a co-author, that you have contributed to the article, and that you agree to the publication of it, in case it is accepted.

https://www.editorialmanager.com/boms/l.asp?i=157033&l=HE20E46R

Please click this link if you do not agree to the above:

https://www.editorialmanager.com/boms/l.asp?i=157034&l=37RU3VEH

Thank you and kind regards,
Editorial Office

2. Permission granted to use publiched manuscrip: Paper 2

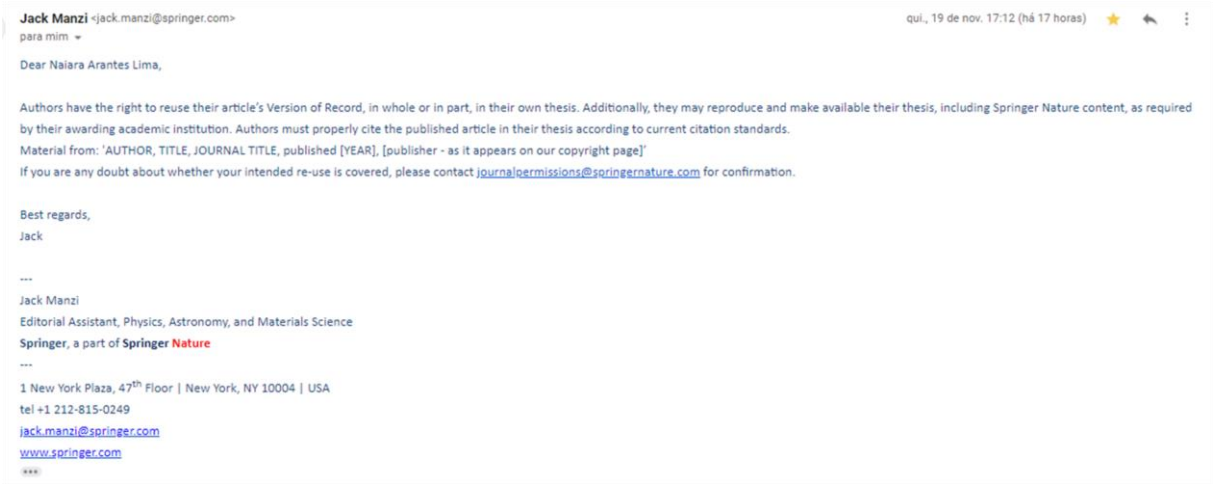

**Jack Manzi** <jack.manzi@springer.com> qui., 19 de nov. 17:12 (há 17 horas)
para mim

Dear Naiara Arantes Lima,

Authors have the right to reuse their article's Version of Record, in whole or in part, in their own thesis. Additionally, they may reproduce and make available their thesis, including Springer Nature content, as required by their awarding academic institution. Authors must properly cite the published article in their thesis according to current citation standards.
Material from: 'AUTHOR, TITLE, JOURNAL TITLE, published [YEAR], [publisher - as it appears on our copyright page]'
If you are any doubt about whether your intended re-use is covered, please contact journalpermissions@springernature.com for confirmation.

Best regards,
Jack

---
Jack Manzi
Editorial Assistant, Physics, Astronomy, and Materials Science
**Springer**, a part of **Springer Nature**
---
1 New York Plaza, 47th Floor | New York, NY 10004 | USA
tel +1 212-815-0249
jack.manzi@springer.com
www.springer.com

3. Permission granted to use publiched manuscrip: Paper 3

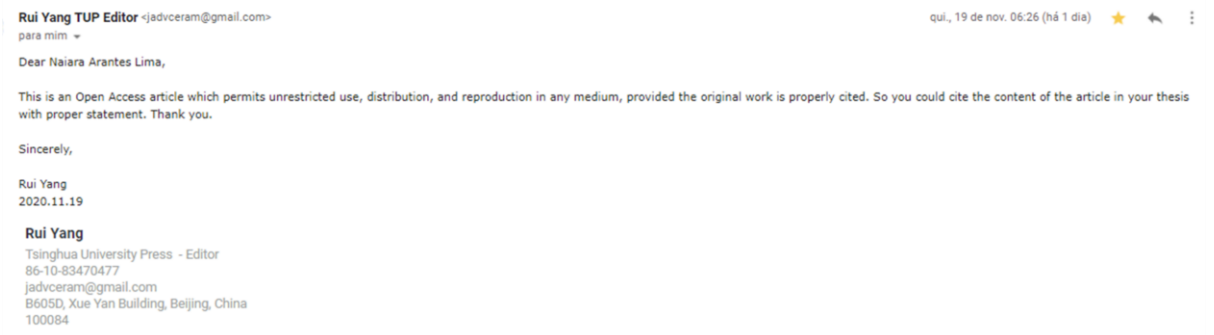

**Rui Yang TUP Editor** <jadvceram@gmail.com> qui., 19 de nov. 06:26 (há 1 dia)
para mim

Dear Naiara Arantes Lima,

This is an Open Access article which permits unrestricted use, distribution, and reproduction in any medium, provided the original work is properly cited. So you could cite the content of the article in your thesis with proper statement. Thank you.

Sincerely,

Rui Yang
2020.11.19

**Rui Yang**
Tsinghua University Press - Editor
86-10-83470477
jadvceram@gmail.com
B605D, Xue Yan Building, Beijing, China
100084